Alma Mater Studiorum · Università di Bologna

Scuola di Scienze
Corso di Laurea Magistrale in Fisica del Sistema Terra

Analysis of precipitation from ground observations over the Antarctic coast

Relatore:
Prof. Vincenzo Levizzani

Presentata da:
Alessandro Bracci

Correlatori:
Ing. Luca Baldini
Dott.ssa Nicoletta Roberto

II Sessione
Anno Accademico 2017/2018

Abstract

Improvements in the knowledge of the Antarctic hydrologic cycle are essential in order to assess potential future changes of the surface mass balance and to define the contribution of the Antarctic ice sheet (AIS) on the sea level rise. The primary mass input of the AIS is represented by snow precipitation. Despite of their crucial role, the estimates of precipitation over Antarctica are sparse and characterized by large uncertainties, being not well-assessed by numerical weather/climate models, by ground observations and satellite measurements.

Recently, different research stations in Antarctica were equipped with observatories for cloud and precipitation, included the Italian Mario Zucchelli station (MZS). This thesis is part of the APP-PNRA project ("Antarctic precipitation properties from ground-based instruments") whose object is to set up an observatory to characterize precipitation on the Antarctic coast.

The present study was focused on the evaluation of the response of solid hydrometeors to the electromagnetic radiation and on the microphysical characterization of precipitation.

The former was investigated using a pre-computed discrete dipole approximation (DDA) database for complex-shape snowflakes and a T-Matrix code for soft-spheroids with different axis ratio and density values. The backscattering cross sections calculated at the K-band by the two scattering methods were compared, downstream of a harmonization procedure. In case of aggregate particles the methods show a poor agreement, whereas comparable values are found when pristine crystals are considered.

The latter was examined by considering the in-situ observations by a Parsivel disdrometer and Micro Rain Radar. By exploiting the Parsivel data collected during the austral summer periods 2016-2017 and 2017-2018, the

particle size distributions of hydrometeors were derived. The PSDs show a high number of particles with very small diameter (around 1 mm), as expected. Anomalies in hydrometeor velocities were found in disdrometer measurements close to ground. Hence, the Parsivel retrieval during windy days was also investigated, proving that meteorological conditions seem to affect microphysical observations of Antarctic precipitation.

Numerical simulations, driven by DDA and T-Matrix methods, were also performed by using the particle size distributions, captured by the disdrometer, in order to obtain the simulated equivalent radar reflectivity factor. The comparative analysis of simulated and actual (provided by the MRR) reflectivity allowed to infer microphysical characterization of precipitation events at MZS. Based on this methodology, 16 out of 22 precipitation days during the observation periods were categorized: 6 as having aggregate-like features and 10 as pristine crystal-like. The classification of the snowfall episodes will allow computing the snowfall rate using a proper mass-size relationship.

The methodology studied in this work is an interest step to improve precipitation observation at the ground in the Antarctic region. In fact, accurate ground based measurements are fundamental to calibrate and validate satellite observations which are able to give measurements over large areas. Moreover, the results of this thesis will be of practical interest, giving an important contribution toward a more accurate quantification of snow accumulation in the Antarctic coast.

Sommario

Le precipitazioni in Antartide avvengo quasi esclusivamente sotto forma di neve e rappresentano una delle variabili fondamentali per il calcolo del bilancio di massa superficiale della calotta polare. I cambiamenti di quest'ultima possono inoltre influenzare direttamente il livello del mare a scala globale. Nonostante la loro fondamentale importanza, le misure di precipitazione in Antartide sono decisamente scarse e caratterizzate da una grande incertezza. Infatti, le stime di precipitazione vengono solitamente fornite da modelli di previsione numerica oppure da dati satellitari, i quali necessitano entrambi di misure di riferimento al suolo per la validazione e la calibrazione. Purtroppo però le osservazioni al suolo sono insufficienti e rare, viste le difficili condizioni climatiche presenti nel continente Antartico, che rendono complicata la gestione della strumentazione in-situ.

A livello internazionale, negli ultimi anni, si è assistito ad una crescita dell'interesse per le misure di precipitazione al suolo in Antartide. Diverse stazioni di ricerca sono state attrezzate con strumentazione specifica per la misura della precipitazione, come Princess Elisabeth (Belgio), Dumont D'Urville (Francia) e Mc Murdo (USA). Anche la stazione di ricerca italiana Mario Zucchelli è stata equipaggiata con strumenti in grado di rilevare e caratterizzare le idrometeore e misurare l'accumulo di precipitazione. Questa tesi si inserisce nel progetto di ricerca APP-PNRA (Antarctic precipitation properties from ground-based instruments) che ha come obiettivo quello di installare un osservatorio presso la stazione di Mario Zucchelli, per la caratterizzazione delle precipitazioni lungo la costa antartica.

Il lavoro si è concentrato sullo studio della risposta delle idrometeore solide alla radiazione elettromagnetica nella banda K e sulla caratterizzazione microfisica delle precipitazioni.

La prima tematica è stata analizzata usando due diversi metodi di calcolo delle proprietà di scattering: un database generato tramite il DDA (Discrete Dipole Approximation) che prende in considerazione la complessità della forma delle idrometeore solide, e i risultati di simulazioni effettuate con un codice T-Matrix, il quale approssima le particelle di ghiaccio con uno sferoide di densità e rapporto assiale variabili. Le cross section di backscattering, calcolate con i suddetti metodi dopo una procedura di armonizzazione, sono state confrontate. I risultati mostrano un buon accordo fra le due metodologie di calcolo quando le idrometeore considerate sono cristalli puri ("pristine"), mentre sorgono delle evidenti differenze quando vengono considerate particelle formate da aggregati ("aggregate").

Il secondo argomento è stato trattato analizzando le osservazioni di eventi di precipitazione presso la stazione Mario Zucchelli, rilevati attraverso un Micro Rain Radar ed un disdrometro Parsivel. Utilizzando i dati provenienti da quest'ultimo e raccolti durante le estati australi 2016-2017 e 2017-2018, sono state calcolate le distribuzioni dimensionali delle idrometeore, che mostrano un'elevata concentrazione di particelle di ghiaccio molto piccole, con diametro nell'ordine di 1 mm. Inoltre, sono state riscontrate delle anomalie nella misura della velocità di caduta delle idrometeore, con valori ben più alti di quelli normalmente osservati. Questa singolarità è stata indagata nel dettaglio, provando infine che il metodo di misura utilizzato dal Parsivel viene fortemente influenzato in condizioni di vento forte.

I metodi di scattering DDA e T-Matrix e le distribuzioni dimensionali di idrometeore sono stati poi combinati per ottenere un valore simulato del fattore di riflettività radar equivalente. Questo è stato successivamente comparato col valore di riflettività misurato dal radar MRR nello stesso istante. Il confronto ha permesso di caratterizzare microfisicamente gli even-

ti di precipitazione presso la stazione Mario Zucchelli. Utilizzando questo metodo sono stati classificati 16 giorni di precipitazione dei 22 totali rilevati nei due periodi esaminati. Durante 6 episodi, le idrometeore sono risultate avere caratteristiche simili ad aggregati, mentre in 10 eventi la precipitazione aveva caratteristiche simili a cristalli singoli. Questa classificazione permetterà, all'interno del progetto APP-PNRA, di calcolare l'accumulo di neve al suolo tramite una relazione opportuna che lega massa e dimensione delle idrometeore.

I risultati di questa tesi saranno di interesse pratico poiché potranno dare un importante contributo verso una più accurata misura della precipitazione nevosa al suolo nel continente Antartico.

Contents

1 Introduction **1**

1.1 State of art 3

1.2 The Mario Zucchelli station at Terra Nova Bay 6

1.3 Precipitation in Antarctica 10

1.4 Aim of the thesis 11

1.5 Outline 12

2 Theoretical background **14**

2.1 Solid precipitation microphysics 14

2.1.1 Introduction 14

2.1.2 Ice nucleation 15

2.1.3 Ice nuclei in atmosphere 18

2.1.4 Secondary ice particle production 21

2.1.5 Growth of ice crystals 22

2.1.6 Habits of ice crystals 25

2.1.7 Additional growth mechanisms 28

2.1.8 Solid particle mass-size relations 30

2.1.9 Ice crystal and snowflake size distribution 32

2.2 Electromagnetic theory 35

2.2.1 Introduction 35

2.2.2 Electromagnetic field equation 35
2.2.3 Stokes parameters 36
2.2.4 Scattering by an ice crystal 39
2.2.5 Backscattering cross section 45

3 Data and Methods **48**
3.1 Data 48
3.1.1 Micro Rain Radar (MRR) 48
MRR Data at MZS 56
3.1.2 Parsivel disdrometer 60
Parsivel Data at MZS 69
3.1.3 Ancillary measurements 74
3.2 Methods 75
3.2.1 Discrete Dipole Approximation 77
Overview 77
The NASA DDA Database 80
3.2.2 T-Matrix 86
Overview 86
T-Matrix code 88
3.2.3 Methodology 90
DDA - T-Matrix harmonization 90
Hydrometeors characterization 91

4 Results **93**
4.1 NASA-Leinonen database comparison 93
4.2 The NASA database 96
4.3 DDA - T-Matrix comparison 98
4.4 Particle Size Distribution at MZS 103

4.5 Hydrometeor characterization 108
Aggregate-like event 110
Pristine-like event 114
Unclassified event 121

5 Discussion and conclusion **124**

5.1 Discussion 124
5.1.1 DDA - T-Matrix comparison 124
5.1.2 Microphysical observations 126
5.1.3 Hydrometeor characterization 128
5.2 Outlook 132
5.3 Conclusion 135
References 138

List of Figures

1.1 Geographical map of the Antartica. Several research stations are depicted with the information of the home country. The Italian research station "Mario Zucchelli" is highlighted. Adapted from: Ponzo and Lori (2007). 7

1.2 Aerial view of the "Mario Zucchelli" research station at Terra Nova Bay. Source: Ponzo and Lori (2007). 9

1.3 Mean annual snowfall rate in mm (water equivalent) per year from CloudSat satellite for the period August 2006-April 2011. Source: Palerme *et al.* (2014). 11

2.1 Diagram of habits in text and pictorial format for ice crystals drawn form laboratory results and from observations. Source: Bailey and Hallett (2009). 27

2.2 Size distributions for aggregate snowflakes in a semi-log plot for different rainfall rate values fitted by Gunn and Marshall formula. Dots are experimental data. Adapted from: Gunn and Marshall (1958). 33

2.3 Coordinate system used to described the direction of propagation and the polaritation state of a plane electromagnetic wave. Source: Mishchenko *et al.* (2002). 37

3.1 Working block diagram of the Micro Rain Radar. Source: Löffler-Mang *et al.* (1999). 50
3.2 Frequency of the transmit signal and the echo. Here t_h represents the travel (delay) time of the response pulse. Source: Metek (2010). 52
3.3 Micro Rain Radar at Mario Zucchelli research station on the roof of the logistic container. 56
3.4 Control computer of Micro Rain Radar at MZS (on left). White box in the middle is the Junction Box. It is used to pass through the communication between the PC and the RCPD (Radar control and processing device and transceiver) mounted on MRR dish. 58
3.5 Functional principle of Parsivel. Source:OTT (2017b). 61
3.6 Signal modification due to falling of large/small particle (upper plate); related raw signal outputs (middle plate); inverted and amplified signal (lower plate). Source: Löffler-Mang and Joss (2000). 62
3.7 Semplified hydrometeors classification based on size and velocity values. X-axis particle dimension (mm), y-axis particle speed (m/s). Source: Löffler-Mang and Joss (2000). 64
3.8 Parsivel snowflake measuring example. WHD stands for widest horizontal dimension. Source: Battaglia *et al.* (2010). 66
3.9 Schemating portayal of Parsivel measurement principle in case of no wind (left hand side) and windy atmpospheric conditions (righ hand side). Gray arraw stands for particle motion. During windy conditions that is the sum of air motion and particle fall velocity. Source: Friedrich *et al.* (2013a). 68

3.10 Classical stationary Parsivel disdrometer (left hand side) and articulating disdrometer (right hand side). The latter, thanks to the coupled anemometer, is able to continuonsly orient Parsivel sampling area perpendicular respect to the wind. Source: Friedrich *et al.* (2013a). 69
3.11 Parsivel at Mario Zucchelli on the roof of a logistic container. . 70
3.12 Data tab of Parsivel application software ASDO. Source: OTT (2017a). 71
3.13 Automatic weather stations network (red dots) of Osservatorio Meteo Climatologico Italiano in Antartide. Source: climantartide.it 75
3.14 The Eneide automatic weather station. Source: climantartide.it 76
3.15 Nine pristine habits of NASA database (first row). Beneath, snaphots of aggregation mechanism for each habit. Source: Kuo *et al.* (2016). 81

4.1 Comparison between backscattering cross section values of NASA (dots), calculated by maximum diameter, and Leinonen (circles) databases. Colors represent Ku (red), Ka (green) and W (blue) bands. 94
4.2 Comparison between the backscattering cross section values of the NASA (dots) calculated by projection radius and the Leinonen (circles) databases. Colors represent Ku (red), Ka (green) and W (blue) bands. 95
4.3 Comparison between the backscattering cross section values of the NASA (dots) calculated by equivalent radius and the Leinonen (circles) databases. Colors represent Ku (red), Ka (green) and W (blue) bands. 95

4.4 NASA database backscattering cross sections for the ice pristine particles at K-band. Colors represent different hydrometeor habits. 97
4.5 NASA database backscattering cross sections for ice aggregate particles at K-band. Colors represent different hydrometeor habits. 97
4.6 Density-dimension power law relation of the DDA NASA database. Blue dots represent database of aggregate particles. Red line stands for fitting line. The other lines are relationships from the literature for reference. 98
4.7 Aspect ratio-dimension linear relation of the DDA NASA database. Blue dots represent the database of aggregate particles. Red line is a fitting line. 99
4.8 Backscattering cross sections at 24 GHz. Dots represent the NASA DDA database values. Lines with stars stand for the CANTMAT T-Matrix calculations in which the density and aspect ratio depend on the particle diameter. 100
4.9 Backscattering cross sections at 24 GHz. Dots represent the NASA DDA database values. Lines with stars stand for the CANTMAT T-Matrix calculations: black line represents the computation where the size relations were used and it is depicted as reference, the other lines stand for the simulations in which the particle density depends on the particle diameter, whereas the aspect ratio assumes fixed values. 101

4.10 Backscattering cross sections at 24 GHz. Dots represent the NASA DDA database values. Lines with stars stands for the CANTMAT T-Matrix calculations: black line represents the computation where size relations were used and it is provided as reference, the other lines stand for the simulations in which the aspect ratio depends on the particle diameter, whereas the particle density assumes fixed values. 102
4.11 Particle size distribution at the Mario Zucchelli station, calculated through Parsivel data of 32nd Italian Antarctic expedition at MZS. 103
4.12 Probability density function of D_{max} and D_0, calculated through Parsivel data of 32nd Italian Antarctic expedition at MZS. . . 104
4.13 Parsivel spectrograph data of 32nd Italian Antarctic expedition at MZS. Red line represents velocity-speed relation for dendrites (Locatelli and Hobbs, 1974), and it is reported as reference. 105
4.14 Particle size distribution at the Mario Zucchelli station, calculated through Parsivel data of 33nd Italian Antarctic expedition at MZS. 106
4.15 Probability density function of D_{max} and D_0, calculated through Parsivel data of 33nd Italian Antarctic expedition at MZS. . . 106
4.16 Parsivel spectrograph data of 33nd Italian Antarctic expedition at MZS. Red line represents velocity-speed relation for dendrites (Locatelli and Hobbs, 1974), and it is reported as reference. 107
4.17 Errors in modeled and actual radar equivalent reflectivity for the 22 precipitation events considered at MZS. 108

4.18 Meteorological conditions at MZS on 17 December 2016. . . . 111
4.19 Equivalent reflectivity measured by Micro Rain Radar at the Mario Zucchelli research station on 17 December 2016. 112
4.20 Equivalent reflectivity measured by Micro Rain Radar (black line) on 17 December 2016 is reported together with the four Z_e simulations. 112
4.21 Scatter plots: measured versus simulated Z_e values at MZS on 17 December 2016. 113
4.22 Parsivel observations at MZS on 17 December 2016. 113
4.23 Spectral reflectivity (1 minute) measured by Micro Rain Radar on 17 December 2016. 114
4.24 Equivalent reflectivity measured by Micro Rain Radar at the Mario Zucchelli research station on 25 January 2018. 115
4.25 Equivalent reflectivity measured by Micro Rain Radar (black line) on 25 January 2018 is reported together with the four Z_e simulations. 116
4.26 Scatter plots: measured versus simulated Z_e values at MZS on 25 January 2018. 116
4.27 Parsivel observations at MZS on 25 January 2018. 117
4.28 Equivalent reflectivity measured by Micro Rain Radar at the Mario Zucchelli research station on 4 January 2018. 118
4.29 Equivalent reflectivity measured by Micro Rain Radar (black line) on 04 January 2018 is reported together with the four Z_e simulations. 119
4.30 Scatter plots: measured versus simulated Z_e values at MZS on 04 January 2018. 119
4.31 Parsivel observations at MZS on 4 January 2018. 120

4.32 Spectral reflectivity (1 minute) measured by Micro Rain Radar on 04 January 2018. 120
4.33 Equivalent reflectivity measured by Micro Rain Radar at the Mario Zucchelli research station on 13 January 2018. 122
4.34 Equivalent reflectivity measured by Micro Rain Radar (black line) on 13 January 2018 is reported together with the four Z_e simulations. 122
4.35 Scatter plots: measured versus simulated Z_e values at MZS on 13 January 2018. 123

5.1 Picture of the fallen hydrometeors at the Mario Zucchelli research station on 2 December 2016. 131

List of Tables

3.1 Main technical specifications of the Micro Rain Radar. 51

3.2 Explanation of Parsivel telegram data. 73

3.3 NASA database variables provided for each particle and their explanation. 84

4.1 Precipitation events at MZS during the 32nd and 33rd Antarctic expeditions, classified by the best simulation estimate. . . . 110

Chapter 1

Introduction

The polar regions have been and will be the most affected areas by climate change (Johnston, 2009). Antarctic Ice Sheet (AIS) actually plays a major role in regional and global climate variability and represents, probably, the most critical factor of future sea-level rise, as it contains approximately more than 70% of the world's fresh water. While some hints of ice sheet reduction during the past decade are present, Antarctic ice sheet could represent a major contributor to sea level rise over 21st century (Shum *et al.*, 2008) in a global climate change scenario, considering its volume equivalent to about 58 meters on global mean sea level rise (IPCC, 2014). Sheperd *et al.* (2018) have recently presented comprehensive overview about the mass balance of AIS from 1992 to 2017 and confirmed such concerns. Combining satellite observations of its changing volume, flow and gravitational attraction with modelling of its surface mass balance, the researchers showed that AIS had lost about 2,700 billion tonnes of ice during the period considered, resulting in a mean sea level rise of approximately 8 millimeters.

Snow, and solid precipitation more broadly, have been recognized as primary mass input for the ice sheet. Bearing all this in mind, a deeper knowl-

edge of Antarctic ice sheet input as well as a continuous monitoring of its trend would be desirable and very much needed. Moreover, the knowledge of Antarctic hydrological cycle is essential even for assessing the radiative budget of the lower atmosphere in addition to evaluate the ice sheet variation, the surface mass balance and the evolution of sea level height (Scarchilli *et al.* 2011; DeConto and Pollard 2016).

Despite its fundamental role, the knowledge of precipitation over polar region, particularly over Antarctica, remains largely unknown (Grazioli *et al.*, 2017a), being this quantity not well-estimated by numerical weather/climate models, by ground observation and satellite measurements as well.

As pointed out by Agosta *et al.* (2015), being based on physical assumptions and schemes that are not generally suited for polar conditions, most climate models are not able to quantify precipitation, showing a large bias to observations or reanalysis products. On the other hand, both satellite measurements and weather models need ground observations in order to be calibrated and validated, although some steps toward detection of solid precipitation by means of the CloudSat satellite data have been made (Palerme *et al.* 2014; Milani *et al.* 2016).

Accurate ground observations, that would be useful to improve numerical model performance and to constrain measurements from space, are hard to get due to the intrinsic complexity of solid precipitation measurements and, in Antarctica, in addition to low precipitation rates. Furthermore, difficult access and complex logistical operation add huge drawbacks to an intrinsically uncertain context. Moreover, the vastness of the continent, the extreme environment and the harsh climatic conditions cause significant difficulties in measuring and monitoring precipitation (Gorodetskaya *et al.* 2015; Grazioli *et al.* 2017b).

These are the main reasons why ground-based precipitation measurements in the Antarctic region are scarce and of limited accuracy. Summarizing, the available measurements are not able to support the characterization of Antarctica precipitation microphysics, the comprehension of precipitation process mechanisms , and to provide accurate quantitative input for establishing a hydrologic cycle for Antarctica.

1.1 State of art

In the Antarctica Region, however, some ground-based remote-sensing instruments have been operated and are operational in different research stations and some information on clouds and precipitation is available (e.g. Del Guasta *et al.* 1993; Bromwich *et al.* 2012).

Nevertheless, there is a need for permanent observations over AIS in order to provide valuable information on a long term. Being this knowledge a pressing and an actual task for the scientific community, over recent years some Antarctic stations, namely "Princess Elisabeth Antarctica" (PE) (Belgium), "Dumont d'Urville Station" (DDU) (France), "McMurdo" (USA) and "Mario Zucchelli" (Italy) are being equipped to continuously observe clouds and precipitation.

Several instruments collected data in the austral summer 2015/16 at DDU station, and one of them (Micro Rain Radar) is operating continuously. According to Grazioli *et al.* (2017b), a polarimetric weather radar (MXPol), a Micro Rain Radar (MRR), a weighing gauge (Pluvio^2) and a Multi-Angle Snowflake Camera (MASC) have collected the first model-free measurements of precipitation (including of precipitation microphysics) in the region of the Adelie Land, where DDU is located. Thanks to these in-situ instruments,

researchers can obtain a more realistic estimation of precipitation amount keeping out phantom accumulation (a well-known phenomena that occur during intense wind events and that provokes blowing snow and vibration). Results have shown higher values (at least 10%) of DDU measurements with respect to ERA-Interim reanalysis values. Moreover, using simultaneous data from MRR, MXPol and Pluvio^2, they obtained a local Z-S relation (i.e. an equation to calculate snowfall intensity (S) from radar reflectivity (Z)) suited for precipitation events at DDU. Furthermore, an immediate micro-physical parameter of precipitation was inferred using MXPol and MASC camera. The latter provided a classification of hydrometeors at ground level according to Praz *et al.* (2017) method, while from polarimetric data of MXPol a classification covering a ray of hundred kilometers and at different heights were obtained (Grazioli *et al.*, 2015). Continue measurements provided by the Micro Rain Radar at DDU were used by Grazioli *et al.* (2017b) to investigate the role of katabatic winds in sublimation of precipitation at low atmospheric level (below 1000 meters) and a significant depletion of snowfall in some events was observed. Going into details, connecting MRR data and daily radiosounding at DDU, an evaluation of the loss of precipitation due to katabatic dry winds at DDU was achieved and, in some low intensity snowfall events, a loss of about 100% of precipitation was observed. Besides, a quantification of sublimination was calculated by a "total sublimination ratio" using MRR vertical profiles of snowfall intensity, and a comparison between snowfall ground measurements and satellite data was made in order to better evaluate the role of low atmospheric levels into precipitation loss.

Gorodetskaya *et al.* (2015) analyzed measurements from cloud, precipitation and meteorological observatory at Princess Elisabeth. PE is located at Dronning Maud Land (East Antarctica) and is equipped with a ceilometer,

a radiation pyrometer, a vertical pointing radar (MRR) and some automatic weather stations. Operating since 2010, this observatory has been able to capture and underline the complexity of Antarctic precipitation. Hourly mean snowfall rate was derived from radar data through several Z-S (see above) literature relationships, in order to take into account the extreme variability in snow particle shapes, size distributions and densities, which are major sources of uncertainty in Z-S relations. From ceilometer data, clouds and precipitation occurrence, as well as cloud base height, were derived using a polar threshold suited for high latitude zones (Van Tricht *et al.*, 2014). Some case studies (e.g. blowing snow episodes) related to a particular synoptic scenario were discussed using instrumentation and, in addition, a basic clouds/precipitation statistics was derived from remote sensing measurements. Frequency by height for Z (measured by MRR) and attenuated back-scatter profile (by ceilometer) over 14 months was obtained, showing typical clouds and precipitation signal intensities at PE. Also snowfall accumulation and its interannual variability, as well as surface mass balance component, were calculated, assembling a precious database for research in the Antarctic region and worthy of further study. As a matter of fact, MRR measurements (recorded since 2010 at PE) were used by Souverijns *et al.* (2017) to estimate an appropriate radar reflectivity-snowfall rate relationship. Adding a Precipitation Imaging Package (PIP) disdrometer (installed at the station in January 2016) and combining data with radar observations, a Z-S relation for PE was calculated. According to the authors, this was the first time that disdrometer and radar measurements were matched to obtain such relationship over the Antarctic ice sheet.

In this international background, the Italian Antarctic Research Program (PNRA) has funded research programs at Mario Zucchelli Station,

Terra Nova Bay. The "Italian National agency for new technologies Energy and sustainable economic development" (ENEA) manages the permanent meterological observatory (Clima Antartide[1]) which includes monitoring instruments for clouds and precipitation observation (i.e. a ceilometer, a laser pluviometer, an infrared pyrometer and a Micro Rain Radar) as well as several automatic weather stations (Scarchilli *et al.*, 2017).

Moreover, in 2015, PNRA financed the long term project "Antarctic precipitation properties from ground-based instruments" (APP) with the aim to set up a precipitation observatory at Mario Zucchelli Station (MZS) installing specific instruments for precipitation observation, namely a vertical pointing Micro Rain Radar (MRR) and an optical disdrometer Parsivel, which were installed during last Italian Antarctic expedition (2017-2018) (Roberto *et al.*, 2017).

1.2 The Mario Zucchelli station at Terra Nova Bay

Antarctica is known as the highest, driest, windiest and coldest continent, with the lowest recorded temperature on Earth, namely -89.2°C at Russia's Vostok Station, which is located over the Polar Plateau (Turner *et al.*, 2009). The Antarctic region extends for more than 14 millions km^2 commensurate with about 10% of the land surface of Earth. Most of the continent, apart from the northern part of the Antarctica Peninsula, lies south of the Antarctic Polar Circle. The mean elevation of the continent is about 2.200 meters above sea level, as land surface rises rapidly from the coast. It has a quasi-circular shape excluding the Antarctic Peninsula and some large inlets

[1] www.climantartide.it

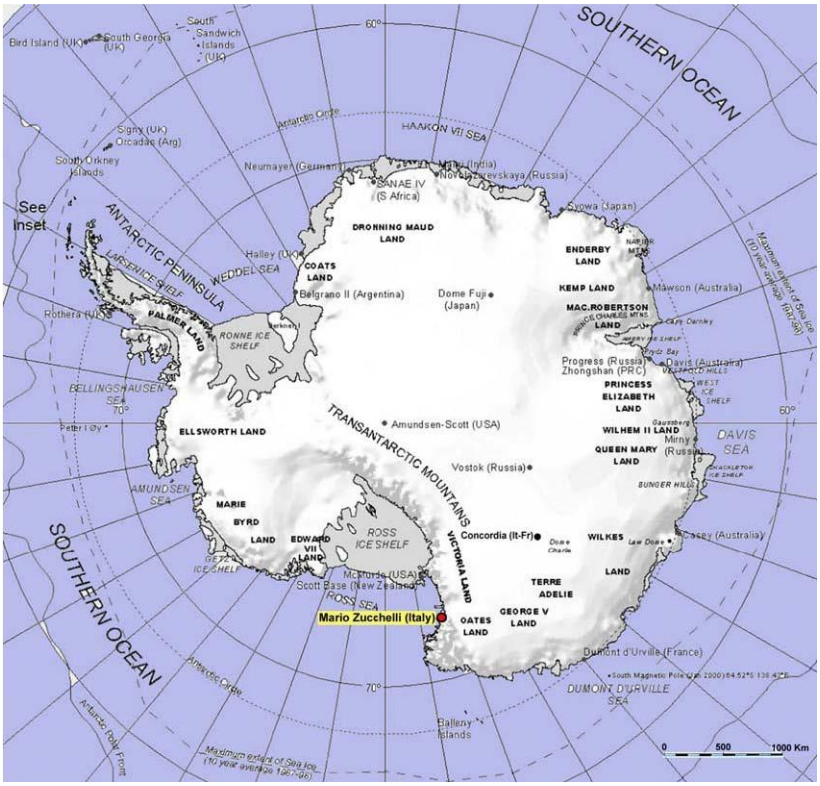

Fig. 1.1: Geographical map of the Antartica. Several research stations are depicted with the information of the home country. The Italian research station "Mario Zucchelli" is highlighted. Adapted from: Ponzo and Lori (2007).

(i.e. Ross and Weddell seas). The latter, together with the Transantarctic Mountains Range, divide the continent into West and East Antarctica (see Figure 1.1). For a long time Antarctica was known only as remote and harsh land and it was also subjected to several territorial claims until 1 December 1959, when the Antarctic Treaty was signed. This document, suspending any territorial demands, stated that Antarctica shall be used only for peaceful purposes and that the scientific investigations and observations from the Antarctic region shall continue, with data being exchanged and made freely

available. In this international framework, Italy launched in 1985 the PNRA (National Antarctic Research Programme) and quickly thereafter the first research station was built (1986).

The latter is the Italian Antarctic research station "Mario Zucchelli" (Figure 1.2) (74.7°S, 164.1°E) that is located at Terra Nova Bay, in the polar cap at the confluence of the Reeves and Priestley glaciers (Cristofanelli *et al.*, 2011). Terra Nova Bay is a large inlet along the coast of the central part of Victoria Land at the western margin of the Ross sea. The mountains facing the Bay belong to the Transantarctic Mountains Range (Argentini *et al.*, 1995). MZS is a permanent station in Antarctica even if it is functioning only during the Austral summer period (October to February) hosting several scientific research programmes which range from Earth science, oceanography and marine biology to atmospheric chemistry and physics. Logistical facilities, buildings and laboratories constitute the MZS, covering an area of more than 7000 m^2 (Ponzo and Lori, 2007).

The mean annual air temperature at MZS is -14.7°C, and each year the temperature rises up to 3°-5°C in the summertime and then falls to less than -20°C in May-August (French and Guglielmin, 2000). Strong winds affect the area, due mainly to katabatic effects from the inland ice, and predominantly from the west (French and Guglielmin, 2000). Katabatic surface winds are generated over the Antarctic Plateau by strong radiative cooling, which is responsible for the development of a near-surface inversion layer. The cold, negatively buoyant air is driven downslope by the sloped-inversion force, whose name emphasizes the topographic and thermodynamic forcing (Davolio and Buzzi, 2002). At Terra Nova Bay the Priestley and Reeves glaciers are the main paths through which the cold and gravity driven air flows from the Antarctic plateau toward the bay, reaching the research sta-

Fig. 1.2: Aerial view of the "Mario Zucchelli" research station at Terra Nova Bay. Source: Ponzo and Lori (2007).

tion (Argentini *et al.*, 1995) and blowing from west (coming from Reeves glacier) or from northeast (Priestley glacier). Moreover, the flows moving parallel to the Transantarctic Mountains cause the so called barrier winds (Argentini and Mastrantonio, 1994). These flows are related mainly to the large low pressure systems off shore over the Ross sea (Scarchilli *et al.*, 2017) that push air masses towards the steep coast. Failing to cross the mountain range, the air flow is therefore parallel to the coastline hitting the research station. There are still large uncertainties in current estimates of precipitation amounts at MZS, mainly depending on instrumentation and parametrization used. Piccardi *et al.* (1994) report an approximate value of 270 mm/year water equivalent, whereas satellite estimations range between 100 and 150 mm/year.

1.3 Precipitation in Antarctica

The very low temperatures in the interior of Antarctica year-round, together with the isolation from warm and moist air masses, yield that precipitation there is very low, making much of the Antarctica a desert and the driest continent on Earth (Turner *et al.*, 2009). Moreover, little evaporation and sublimation occur due to the low temperatures and, consequently, precipitation rates are very small. As discussed earlier, numerical models generally do not represent well precipitation due to problems in parameterizing key processes that drive precipitation (Turner *et al.*, 2009). Therefore, currently, continent wide assessment of snowfall are limited to information from the Cloud Profiling Radar on board of the CloudSat satellite (Souverijns *et al.*, 2018), giving the scarce ground observation network and intrinsic observational problems in measuring solid precipitation aggravated by the windy and extreme environment. Palerme *et al.* (2014) constructed a snowfall climatology of the Antarctic continent using CloudSat products finding that the mean snowfall rate, from August 2006 to April 2011, is 171 mm (water equivalent) per year, over the Antarctic ice sheet, north of 82°S. Moreover, the spatial pattern of the snowfall rate (see Figure 1.3) shows considerable differences between West and East Antarctica. In fact mean annual snowfall rate is 303 mm in the West, whereas only 118 mm in the eastern region of the continent. In addition, it should be noted that precipitation in the peripheral part of ice sheet (with elevation $<$2250 meters) is 303 mm per year, in comparison to a value of 36 mm related to the inner areas of the continent.

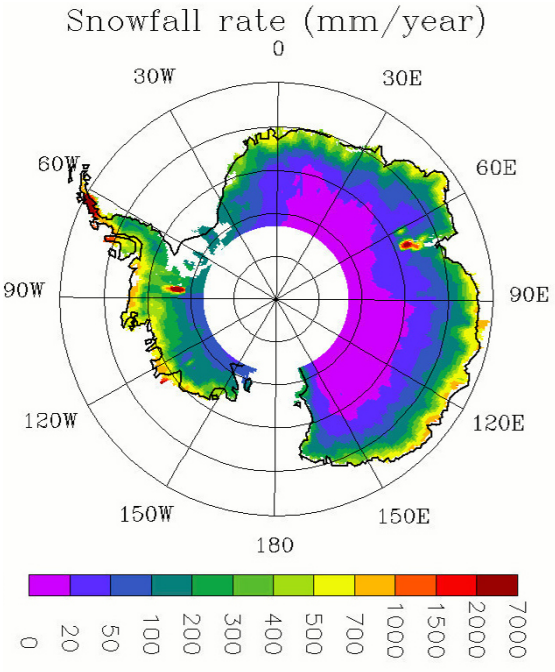

Fig. 1.3: Mean annual snowfall rate in mm (water equivalent) per year from CloudSat satellite for the period August 2006-April 2011. Source: Palerme *et al.* (2014).

1.4 Aim of the thesis

This thesis is part of the APP-PNRA project (Dr. Roberto and Dr. Baldini, Institute of Atmospheric Sciences and Climate - National Research Council of Italy) to set up an observatory to characterize precipitation on the Antarctic coast through the analysis of radar and disdrometer data from the measurement site and to develop a methodology for the synergetic use of MRR radar and disdrometer values.

In this dissertation MRR reflectivity and Parsivel measurements as well as scattering methods were investigated with the purpose of:

- obtaining seasonal Particle Size Distribution (PSD) of precipitation at the Mario Zucchelli research station, highlighting annual variations and wind influence;
- exploring the response of pristine ice crystals, ice aggregates and snowflakes to electromagnetic radiation at 24 GHz (K-band, MRR operational frequency), through numerical simulations, using a DDA (Discrete Dipole Approximation) scattering database and the T-Matrix scattering computation method;
- calculating the equivalent radar reflectivity factor (Ze) from PSD data and DDA (or T-Matrix) particle back-scattering cross sections, and comparing such values with Ze measured by MRR;
- classifying, given scattering property dissimilarity of different precipitation particles, precipitation types at MZS during Austral summertime of the beginning two years of data (2016-2017, 2017-2018).

1.5 Outline

The thesis is organized as follows. In Chapter 2 a theoretical background is presented. This is divided in two main sections. First, the physics beyond ice hydrometeors, their nucleation, formation and accretion, is examined. Then, the relevant electromagnetic theory is provided with particular emphasis on the backscattering cross section. Chapter 3 concerns data and methods employed in the dissertation. The Parsivel disdrometer and the Micro Rain Radar are presented and scattering methods used in this thesis are discussed. Finally, the methodology set up and followed in this thesis is introduced. Results and hydrometeor classification are given in Chapter 4

along with some case studies. Chapter 5 presents discussion and conclusion of the present work.

Chapter 2

Theoretical background

2.1 Solid precipitation microphysics

2.1.1 Introduction

The processes governing rain formation inside clouds are quite complicated and, to some extent, still not completely understood. Two basic microphysical mechanisms, by which precipitation forms in clouds, are often presented as conceptual models in order to make a convenient and explanatory differentiation of processes producing precipitation: warm rain and cold rain.

The former refers to rain derived from non icephase (hence completely liquid) processes in clouds (Lau and Wu, 2003) and where collisions and coalescence of water droplets of different sizes (thus with different terminal velocities) are the dominant ways in which hydrometeors are formed. Coalescence is the leading process of precipitation formation in tropical regions, where updrafts allow huge quantities of water droplets to grow to a large size quite quickly, but is also extremely efficient in some cumulus clouds at middle latitudes whose tops can lay at temperatures below freezing level.

The cold rain processes occur when temperatures in all or parts of the clouds are lower than 0°C. In these colder regions clouds are usually composed of both ice crystals and supercooled liquid water droplets (Wang and Georgakakos, 2005). The ice crystals, which form in this supercooled region, grow rapidly, drawing moisture from the surrounding cloud droplets through a well-known mechanism called Wegener-Bergeron-Findeisen (WBF) process. As pointed out by Glickman (2000) the basis of this theory is in fact that the equilibrium water vapor pressure with respect to ice is less than that with respect to liquid at the same subfreezing temperature. Thus within a mixture of these (ice and liquid) particles, and provided that the total water content were sufficiently high, the ice crystals would gain mass by vapor deposition at the expense of the liquid drops that would lose their mass by evaporation.

Because of the ambiguity in distinguishing between liquid-phase and ice-phase rain at elevation higher than the freezing level, it must be clearly noted that considerable uncertainty exists in the definitions of warm and cold rain.

2.1.2 Ice nucleation

More than 50% of the earth's precipitation originates in the ice phase. Ice nucleation, therefore, is the starting mechanism leading to precipitation. The poorly understood processes of ice initiation and secondary ice multiplication in clouds result in large uncertainties in the ability to model precipitation production and to predict climate changes (Heymsfield *et al.*, 2010). Santachiara *et al.* (2014) point out that ice formation can take place by two phase changes: water vapor deposition or freezing of small water drops. Both these processes are possible, in principle, through homogeneous or heterogeneous nucleation, i.e. triggered by aerosol particles called ice nuclei (IN). These processes can also be called as Primary processes (namely nucleation of ice

from the liquid or water vapour phases) whereas Secondary processes (i.e. a single ice crystal may act as IN, favoring, in some circumstances, the generation and the nucleation of new ice particles) could happen in a subsequent stage.

Homogeneous freezing of small water droplets initiates within the interior volume of a cloud droplet and may occur when enough water molecules stick together within the droplet to form an embryo of ice. In other words, random fluctuations of water molecules produce a structure acting as IN, carrying on the ice particle formation. As in homogeneous nucleation of water drops from vapor, the dimensions of stable nuclei and the probability of embryo formation behave as key factors. Considering that these quantities derive from solid-liquid interfacial free energy, a temperature of -40°C has been calculated as needed for freezing of liquid supercooled drops smaller than 5μm and, in addition, the temperature at which water droplets first freeze increases with the droplet size. In the atmosphere, even though supercooled liquid drops are frequent, very occasionally at such low temperature conditions, a water drop exits because heterogeneous nucleation has yielded to ice particle at higher temperatures. Although freezing does not take place immediately below 0°C, the ice phase is frequently observed in the atmosphere as cloud temperature approaches -20°C (Pruppacher and Klett, 1997) thanks to heterogeneous nucleation.

Homogeneous deposition, in turn, comes from water vapor molecules random collisions forming a stable ice embryo. In order for this process to be efficient very high values of supersaturation would be required (10-70 % respect to the ice). In the atmosphere rarely supersaturation exceeds a value of 1-2% with respect to water, because the heterogeneous nucleation of liquid droplets starts at lower values of vapor density excess implicating a decrease

of supersaturation. Hence homogeneous deposition it is not possible in the atmosphere.

Ice crystals thus appear below -20°C /-15°C indicating heterogeneous nucleation, and this temperature is assumed as a cut-off threshold for that process. The probability of nucleation mostly depends on the properties of the substrate material. The more tightly-bound the water molecules are to the substrate, the greater will be the probability of ice nucleation. In addition, if the crystal structure of the substrate closely resembles that of an ice crystal, it will increase the chances of ice nucleation (Liou and Yang, 2016), along with supercooling and supersaturation conditions. Moreover, when the binding and the matching of the crystal lattice are good, heterogeneous freezing occurs at lower supersaturation and higher temperatures than homogeneous freezing (Santachiara *et al.*, 2014).

Therefore supercooled clouds (also known as "mixed phase" clouds, meaning consisting of supercooled liquid droplets and ice particles) exist thanks to a huge concentration of aerosol particles in the atmosphere, of which a small amount acts as ice nuclei. Indeed these IN are rare in comparison to cloud condensation nuclei which form liquid droplets.

Heterogeneous ice nucleation has been hypothesized to occur in four different modes: deposition, condensation, immersion and contact (Vali, 1985). These can be briefly described as follows by referring to descriptions made by Murray *et al.* (2011) and by Broadley *et al.* (2012):

- deposition mode nucleation involves deposition of ice onto the solid surface directly from the vapor phase and can occur when conditions are supersaturated with respect to ice. It seems to be less important than the other mechanisms in mixed phase clouds, but it is probably important in upper-tropospheric ice clouds;

- immersion freezing occurs when ice nucleates on a solid particle immersed in a supercooled liquid droplet;
- condensation freezing involves ice formation during the condensation of liquid water onto a solid particle. The distinction between immersion and condensation modes is subtle, since the most likely route for immersing a particle inside a droplet is through condensation on that particle;
- contact freezing occurs when a solid particle comes into contact or collides with the water-air interface.

Immersion mode and contact freezing are thought to be most important in many mixed phase clouds. Generally, contact nucleation has been observed to occur at higher temperatures than immersion freezing for the same IN. Because of the subtle differences among these mechanisms, we usually speak of nucleation by freezing, thus avoiding to specify the process. Furthermore, the relative importance of these freezing modes in the atmosphere is not yet well understood.

2.1.3 Ice nuclei in atmosphere

Ice nuclei may nucleate ice in different ways, depending on temperature and saturation conditions, as well as being controlled by unknown probability in the course of the history in the cloud (Liou and Yang, 2016). Giving their importance, many studies have been carried out both in laboratories (e.g. Santachiara *et al.* 2014) and direct airborne and ground observations in the atmosphere (e.g. Patade *et al.* 2014; Jiang *et al.* 2015) in order to enhance the understanding of concentrations and compositions of IN.

According to Jiang *et al.* (2015) large spatial and temporal variations in IN concentration were observed during different campaigns worldwide. Usually the IN number varies in a range between values slightly above zero and a few tens per liter, depending also on atmospheric temperature and supersaturation. In particular, the dependence of IN concentration on temperature has been parameterized (e.g. Fletcher *et al.* 1962) showing a nearly exponential relationship:

$$N = N_0 exp(-bT) \tag{2.1}$$

where T is the activation temperature, N is the number concentration of activated IN under temperature T, N_0 and b are empirical parameters. Specifically, N_0 is the concentration at 0 degrees, instead b can vary between 0.3 and 0.8 degrees^{-1} (experimental values).

In urban air, the total concentration of aerosol is on the order of 10^8 per liter, and only about one of them has been observed to act as a effective IN at -20°C (Liou and Yang, 2016).

In Antarctica several observation campaigns were carried out with the aim of measuring aerosol concentration, size distribution and the condensation nuclei of clouds (e.g. Contini *et al.* 2010; Belosi *et al.* 2012). However the characteristics of the IN, their composition and concentration were more rarely investigated. A research conducted by Ardon-Dryer *et al.* (2011) at the South Pole station reported a concentration of 1 IN per liter at a temperature of -23°C. Earlier, Saxena and Weintraub (1988) measured IN at Palmer station discovering a number that spans from 0.03 to 10 IN per liter at -5°/-7°C.

In the framework of the 27th Italian Antarctica expedition of PNRA (Italian National Program for research in Antarctica) some IN measurements were performed by Belosi *et al.* (2014) at the Mario Zucchelli Station, Terra

Nova Bay, in November 2011. They found values from about 5 to 35 IN per m^3 at the air temperature of -17°C.

Sources of IN can be natural (organic, such as bacteria, pollen, lichen, fungi, decaying vegetation material, marine bacteria associated with plankton, and inorganic namely clay particles, volcanic ash, soil dust) or anthropogenic (soot, metallic oxides emitted by steel furnaces, copper smelters, etc.) (Belosi *et al.*, 2014). Observations have shown that clay minerals, usually containing silicate, with variable amounts of water trapped in the mineral structure and with a very small sizes (from 0.1 μm to a few micrometers in diameter) act as primary component of atmospheric ice nuclei, in particular the kaolinite, that is a common material found in many soil types. Moreover, the activation temperature of such materials seems to be relatively high, only -9°C (Liou and Yang, 2016). Typically, one solid silicate particle was found in the central portion of snow crystal. The diameter of that particles ranged from 0.1 to 15 microns. These finding suggest that desert and arid regions of the Earth surface are the major source of IN (Pruppacher and Klett, 1997).

Another main source of ice nuclei is represented by bacteria. Indeed, as reported in Joly *et al.* (2013), they can catalyze ice formation thereby potentially contributing to the induction of precipitation in supercooled clouds and subsequently to bacterial deposition. In particular, bacteria of the genera Pseudomonas, Pantoea, Erwinia and Xanthomonas seem to exhibit the most efficient IN characteristics, inasmuch some of them can catalyze freezing of supercooled water at a temperature as high as -2°C (Cochet and Widehem, 2000).

Generally materials that act as good IN have properties quite different from those that make good cloud condensation nuclei. Specifically, as reported in Wang (2013), the following characteristics seem to be fundamental:

- water insolubility: while soluble particles can act as suitable CCN, they are not good ice nuclei, that are, instead, all water-insoluble;
- size: observations and laboratory studies have shown larges particle are preferable IN, better than materials in Aitken aerosol region;
- hydrophobicity: again, as opposed to cloud condensation nuclei, hygroscopicity is not a desirable characteristic for IN particle;
- chemical bond and crystallographic similarities: molecular and lattice features play an important role in IN definition. Materials that contain hydrogen bonds or bonds of similar nature would also help to promote ice nucleation. In addition, since ice has a peculiar crystallographic structure, so particle akin to ice have greater chance to operate as IN.

2.1.4 Secondary ice particle production

In contrast to liquid droplet nucleation in which one cloud condensation nucleus contributes to the formation of a single drop, ice nucleation follows a different pattern. Unexpectedly, airborne measurements have proved that ice crystals concentrations inside clouds are in the region 10^4-10^5 times much more than usual concentration of IN in the atmosphere. This means that particular and efficient mechanisms operate in-cloud favoring multiplication of ice crystals. As also cited in section 2.1.2, these are usually referred as Secondary processes or ice multiplication and occur very rapidly (Hobbs and Rangno, 1990).

Santachiara *et al.* (2014) investigated in detail ice crystal multiplication. They described secondary processes as fracture of ice crystals exposed to dry air layers or collision of preexisting ice crystal, otherwise as fragmentation

of large cloud drops during freezing in free fall or as fragmentation of freezing droplets following their collision with ice particles in the cloud (riming). All these ice particles, derived from these different processes, can act as ice condensation nuclei leading to the formation of new ice crystals.

2.1.5 Growth of ice crystals

Once the ice crystal is formed inside the cloud, the initial stage of its growth is due to the diffusion of water vapor. As previously reported, a saturated environment with respect to water is favorable to a swift growth of crystals at ice supersaturation conditions. Indeed, starting from the Clausius-Clapeyron relationship, it is possible to obtain equation 2.2 where e_s is the saturation vapor pressure at T temperature, R_v and L are the gas constant and latent heat respectively.

$$\frac{de_s}{dT} = \frac{Le_s}{R_v T^2} \tag{2.2}$$

Integration of equation 2.2 leads to equation 2.3 in which values of pressure and temperature (e_{s_0} and T_0) at the triple point of water molecules are involved. Being latent heat of phase change between vapor and ice greater than in vapor-water transition, consequently the saturation vapor pressure over ice is smaller than respect to water. This is the reason why ice crystal growth can take place despite of liquid droplets. Efficiency of this process has a maximum at -12°C (Liou and Yang, 2016).

$$\frac{e_s(T)}{e_{s_0}} = exp[L(1/T_0 - 1/T)/R_v] \tag{2.3}$$

This is the well known mechanism called Wegener-Bergeron-Findeisen, already described in section 2.1.1.

Then, in order to quantify the mass increase of an ice particle, a mathematical procedure known as electrostatic analogy is followed, representing the starting point of ice crystal growth theory. The electrostatic potential function Φ outside a charge conducting body satisfies Laplace's equation $\nabla^2\phi = 0$ and also the boundary conditions represented by $\Phi = \Phi_s$ that is constant on the conductor and by $\Phi = \Phi_\infty$ again constant at infinity i.e. far enough from the conductor to gain unruffled conditions (Pruppacher and Klett, 1997). In a similar way, considering the growth of an ice particle with a similar geometry as the conducting body, the governing equation (2.4) can be written down, where ρ_v is the environmental vapor density.

$$\nabla^2\rho_v = 0 \tag{2.4}$$

Also boundary conditions are satisfied, given by $\rho_v = \rho_{v,S}$ i.e. constant over surface S (ignoring in that way the local curvature of the particle) and $\rho_v = \rho_{v,\infty}$ constant at infinity. Obviously the ice particles are mostly non-spherical and this is to be considered. However, through this analogy, it is possible to determine the diffusion growth rates for stationary non-spherical ice particles without solving directly the equation 2.4, namely borrowing known solutions for the electrostatic problems and using them in this situation.

The set of equations of electrostatic problem, as shown before, is identical to the ice problem considering ρ_v equivalent to Φ. To achieve the electrostatic solution a conductor with total electric charge Q is to be considered. This conductor produces an electric field $\vec{E}$ on its surface. It is well known that $\vec{E}$ is linked to Φ by the following relationship:

$$\vec{E} = -\nabla\Phi \tag{2.5}$$

Moreover, using Gauss law and integrating electric field over a surface that

envelops the conductor the equation 2.6 can be obtained (Wang, 2013).

$$\oint_S \vec{E} \cdot d\vec{S} = \oint_S (-\nabla\Phi) \cdot d\vec{S} = 4\pi Q = 4\pi C(\Phi_\infty - \Phi_S) \tag{2.6}$$

C, representing capacitance of conductor, is equal to:

$$C = \frac{Q}{\Phi_\infty - \Phi_S} \tag{2.7}$$

Hence, taking advantage of the analogy, as ρ_v is equivalent to Φ, replacing Φ with ρ_v and $\vec{E}$ with $-\nabla\rho_v$ and using equation 2.6, the following equation is obtained:

$$\frac{dm}{dt} = \oint_S (-D_v \nabla\rho_v) \cdot d\vec{S} = 4\pi D_v C(\rho_{v,\infty} - \rho_{v,S}) \tag{2.8}$$

This allows to calculate the diffusion growth rate of the ice crystal depending on D_v (i.e. the vapor diffusivity) and on C, that is function of particle dimensions and shape. If $C = r$ the equation depicts diffusion growth for a liquid droplets. For a circular disk of radius r, $C = 2r/\pi$ can be used for plate type ice crystals. Several C values, referring to different particle shapes, have been calculated (Pruppacher and Klett, 1997), but actual ice crystals display many different and complex shapes and thus some approximations are necessary. Hence dendrites and plates have to be approximated as circular disk of equal area or needles by a long prolate spheroids (Liou and Yang, 2016).

During the growth, the ice crystal surface temperature tends to be warmed by release of latent heat, so value of $\rho_{v,S}$ is greater than the one it would have without heating. Under stationary growth conditions the amount of $\rho_{v,S}$ is given by heating trough latent heat release and by diffusion of heat away from ice crystal in the form:

$$\frac{\rho_v - \rho_{v,S}}{T_S - T} = \frac{K}{L_s D_v} \tag{2.9}$$

where K is the thermal conductivity coefficient, T and T_s are the ambient temperature and the temperature at crystal surface respectively and L_s is the latent heat. Through the combination of equations 2.8 and 2.9 and by definition of saturation ratio with respect to ice ($S_i = e/e_i$ where e is the environment vapor pressure while e_i is the saturation pressure over ice) an analytic expression for ice crystal growth speed can be achieved (equation 2.10).

$$\frac{dm}{dt} = \frac{4\pi C(S_i - 1)}{[(\frac{L_s}{R_v T} - 1)\frac{L_s}{KT} + \frac{R_v T}{e_i(T) D_v}]} \tag{2.10}$$

Here, as before, ventilation and kinetic effects have been neglected. In reality, all ice crystals fall relative to air and hence it is necessary to consider the effect of the falling motion to obtain more accurate estimate of the diffusion crystal growth rate (Wang, 2013). Ventilation effects tend to intensify growth speed and can be assimilated into equation 2.10 modifying the denominator with appropriate correction terms. Nevertheless, equation 2.10 remains a good approximation to calculate the growth rate in the cases of large ice crystals.

2.1.6 Habits of ice crystals

As said earlier, the electrostatic analogy is only an approximation of the real growth process, since vapor density and temperature are assumed to be constant on the particle surface. Indeed, while the assumption on temperature could be somehow valid, the constant of vapor density, because the irregularity of crystal surface, is far from being true. The surface of growing crystals is made up of flat terraces of different heights, terminating at ledges and separated by steps (Liou and Yang, 2016), and steps themselves are irregular and erratically distributed. These are the reasons why vapor density varies from place to place on the particle surface.

Environmental conditions, specifically temperature and supersaturation, determine not only the growth rate but also shape and aspect of ice crystals modifying their preferential growth direction. Several studies have been carried out in the last 70 year, producing a variety of habit diagrams describing ice crystal shapes as a function of temperature and ice supersaturation. The diagrams were drawn from laboratory, in situ observations or combinations of the two. Pruppacher and Klett (1997) list different laboratory results (e.g. Kobayashi 1961). Magono and Lee (1966) put together diagrams coming from observation of snowfall obtained at the ground where snow crystals were classified into 80 different types, and each of these types may exist over a wide range of sizes and various degrees of aggregation (Locatelli and Hobbs, 1974).

Bailey and Hallett (2009) made a review of existing diagrams in the literature, and noticed that almost all habit diagrams agree on the behavior of ice crystals at temperatures from 0°C to -18°C, whereas they differ in a fundamental way at lower temperatures. Hence they proposed a new habit diagram as result of the previous studies as well as of their laboratory works and also adding field observations utilizing a nonimpacting cloud particle imager. The comprehensive diagram (Figure 2.1), in which the deep complexity and the great variety of the different forms as well as the intriguing links with supersaturation and temperature are well-represented, covers a temperature range from from 0°C to -70°C and an ice supersaturation values from 0.1 to 0.6. It retains the habits description of older diagram for temperatures above -18°C. It should be noted, for instance, the ice crystal appearance evolution at a fixed supersaturation of 0.1, that varies from plates to columns, again to plates and, as temperature becomes progressively lower, again to column. Shape dependence from supersaturation is clear from the

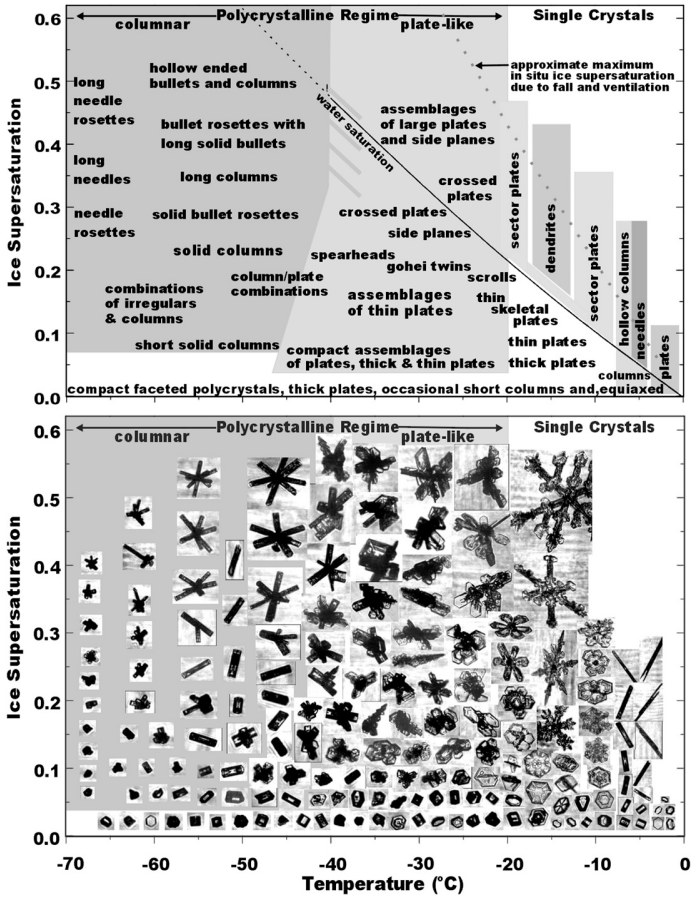

Fig. 2.1: Diagram of habits in text and pictorial format for ice crystals drawn form laboratory results and from observations. Source: Bailey and Hallett (2009).

diagram, for example, fixing temperature at -15°C crystal habit switch form plates to dendrites, whereas at -30°C from plates to columns. In addition, it must be noted that the complexity of forms increases with increasing supersaturation. The study of crystal characteristics at temperatures between -20°C and -70°C was carried out in the laboratory using a static diffusion chamber and it constitutes the new element of the research made by Bailey and Hallett (2004). From -20°C and -40°C they found that plates are

the dominant shape whereas columns mainly appears at lower temperature. In both regimes complexity depends on supersaturation as said previously. Also, it should be pointed out that temperatures of about -20°C and -40°C act virtually as borders dividing single crystal and polycristalline (plates and columnar) regimes. Single crystals (also known as pristine) represent the various shapes of ice particles in the simplest way, but are not fully indicative of all natural snow crystals, which are often dominated by polycristalline forms (Libbrecht, 2005). The latter instead reveal nucleation processes that lead to the formation of irregular polycrystals and crystal twins namely crystals with two or more components growing from a common grain boundary dislocation (Bailey and Hallett, 2004). These complicated shapes should not be confused with aggregate particles (resulting from accretion processes, see section 2.12), as often happens in the literature (Bailey and Hallett, 2009).

2.1.7 Additional growth mechanisms

As mentioned before, ice crystal growth through diffusion processes is by far more efficient than in the liquid drop formation. In fact, in the latter case, collision and coalescence mechanism are fundamental to increase droplets dimensions. Also in the mixed-phase conditions (i.e. at temperatures where supercooled water drops coexist with ice particles), besides growth by water vapor diffusion, an ice crystal can be involved in collision with both cloud drops and other ice particles. In the first mechanism, known as riming, drops can freeze on the ice surface resulting in an increase of hydrometeor dimensions. The terminology of ice particles formed by riming process is considerably not precise and is not generally accepted (Pruppacher and Klett, 1997). As a matter of fact graupels, soft hail as well as snow pellets are all definitions of hydrometeors in which ice crystal has lost its pristine identity,

and particles, because of air intrusions, appear white, fluffy and opaque. Moreover, when a frozen droplet or an ice crystal grown by riming and then converting into a semi-transparent particle, then a small-hail particle can be formed. Finally, subsequent processes of freezing and melting and re-freezing of a single ice particle can result in the so-called ice pellets or sleet.

The second mechanism in which an ice crystal can enhance its dimension is by means of collisions and captures of other crystals, often referred as clumping. The resulting aggregates of crystals are called snowflakes. This is probably the area where we have the least understating among all the accretion growth processes of hydrometeors (Wang, 2013), since few experimental studies have been carried on collision characteristics (e.g. collision efficiency factor). Moreover, there have not been theoretical studies owing to the complexity of the problem (Pruppacher and Klett, 1997). Indeed a collision between crystals does not always end in a merging, they could stick together but also interlock (mainly dendritic habits) without cohesion or could bounce apart. What is certain about this process is the strong air temperature dependence since, from observations, an increasing of aggregation efficiency with temperature could also explain the maximum dimension of aggregates at temperature around 0°C that is usually observed (Magono, 1960). Even though a second diameter maximum at temperatures between -12°C and -17°C was found by Rogers (1974) in addition to the main maximum near 0°C.

Snowflakes usually consist of aggregation of planar snow crystals with dendritic habits, that tend to adhere to one another due to the tangle upon collision, as well as needle aggregate are observed, whereas aggregates of plate and columnar shapes seem to be rare as they tend to rebound.

Another crystal feature that controls ice collisions and captures is fall

speed (Liou and Yang, 2016). Generally such velocity is measured in laboratory studies and it is linked to particle maximum dimension by equation 2.11,

$$u = kD^n \tag{2.11}$$

where u and D represent fall speed and maximum dimension of ice crystal respectively. The terms k and n are experimental coefficients depending on the different ice crystal habits.

A mathematical relation (2.12), similar to equation 2.10, in spite of several uncertainties about the accretion processes, can be obtained in order to describe the variation of the mass of the falling ice crystals.

$$\frac{dm}{dt} = EM\pi R^2 \Delta u \tag{2.12}$$

E represents the mean collection efficiency (e.g. a value of 0.55 for a case dominated by dendrites was found by Mitchell *et al.* (2006)), M denotes the cloud water content, whereas R and δu are the equivalent radius of the collector crystal and the difference in fall velocity between collector ice particle and smaller crystal or supercooled drop water (Liou and Yang, 2016).

2.1.8 Solid particle mass-size relations

The relationships between particle mass or density and dimension play a key role in snow characterization. It is also an essential term in the calculations of ice water content (IWC), of snowfall rate, and it is even strictly connected with the fallspeed-size relation (Heymsfield *et al.*, 2002). Moreover, the electromagnetic scattering properties depend on both size and mass and, in the radar reflectivity simulators, typically a fixed relationship between mass and size is assumed (Botta *et al.*, 2013). Several researches in literature have investigated this aspect through ground observations (Locatelli and Hobbs

(1974), Heymsfield *et al.* (2004), Brandes *et al.* (2007)) agreeing with the power-law form of such relation. Brandes *et al.* (2007) have found the two following equations 2.13 and 2.14 as density and mass versus diameter relationships.

$$\rho(D) = 0.178 D_0^{-0.922} \tag{2.13}$$

$$m(D) = 8.90 \times 10^{-5} D_0^{2.1} \tag{2.14}$$

Here ρ is in grams as well as the mass m. D_0 is the median volume diameter defined as:

$$\int_{D_{min}}^{D_0} D^3 N(D) dD = \int_{D_0}^{D_{max}} D^3 N(D) dD \tag{2.15}$$

Several other density-snowflake size relations are reported in the same paper and it should be noted that although they agree in the use of a power-law equation, they differ in the specific particle diameter. For instance, Muramoto *et al.* (1995) relation is based on the maximum horizontal dimension, whereas Heymsfield *et al.* (2004) consider the diameter of the minimum circumscribed circle that enclose the projected area of the particle. Those differences make direct comparison among these relationships quite difficult.

Several relationship have also been found for the different kinds of ice particle habits. In Locatelli and Hobbs (1974) a thorough list is reported. Moreover, density differences have been observed between pristine and aggregate solid hydrometeors. Indeed pristine crystals typically have a higher density than the aggregates that consist largely of air (Keat and Westbrook, 2017). In addition, as seen earlier, power- law relationships mean that densities are dependent on particle dimensions namely the smaller the particle, the denser it is. This suggests that the inner part of a large snowflake is denser than the outer one. Thus, it is reasonable to interpret snowflakes as particles with density that decreases from the center to the edges (Ori *et al.*, 2014).

2.1.9 Ice crystal and snowflake size distribution

In order to microphysical characterize a cloud or a precipitation event, the frequency distribution of drops/crystals/snowflakes diameters is mandatory and is also one of the primary factors involved in determining radar reflectivity. The distributions are defined as the expected particle concentration within a given volume of air versus liquid or solid particle dimensions.

In the liquid precipitation cases, the most widely used description was that of Marshall and Palmer (1948), a well-know formula to represent raindrop spectra which is based on observations using a dyed filter technique:

$$n(D) = n_0 exp(-\Lambda D) \tag{2.16}$$

Here D (expressed in mm) is the droplet equivolume diameter, $n(D)$ ($m^{-3}mm^{-1}$) stands for drop concentration of equivolume diameter D, whereas n_0 is the intercept of the curve with y-axis and is equal to $8\times\ 10^3$ $m^{-3}mm^{-1}$. The value of term Λ is linked to rainfall rate basing on the equation 2.17.

$$\Lambda = 4.1R^{-0.21} \tag{2.17}$$

Evidently, being an empirical relationship, the units of terms in the equation 2.16 have to be respected, otherwise constant values could change.

For natural snowflakes one of the first studies of size distributions was carried out by Gunn and Marshall (1958) taking up Marshall and Palmer formula. From ground observation they derived equation 2.18, again having an exponential form:

$$n_s(D) = n_s exp(-\Lambda_s D) \tag{2.18}$$

where D is now the diameter of snow particle equivalent melted drop. At first sight, equation 2.18 could appear identical to Marshall and Palmer relationship. Instead, both the other two terms of the equation have a precipitation

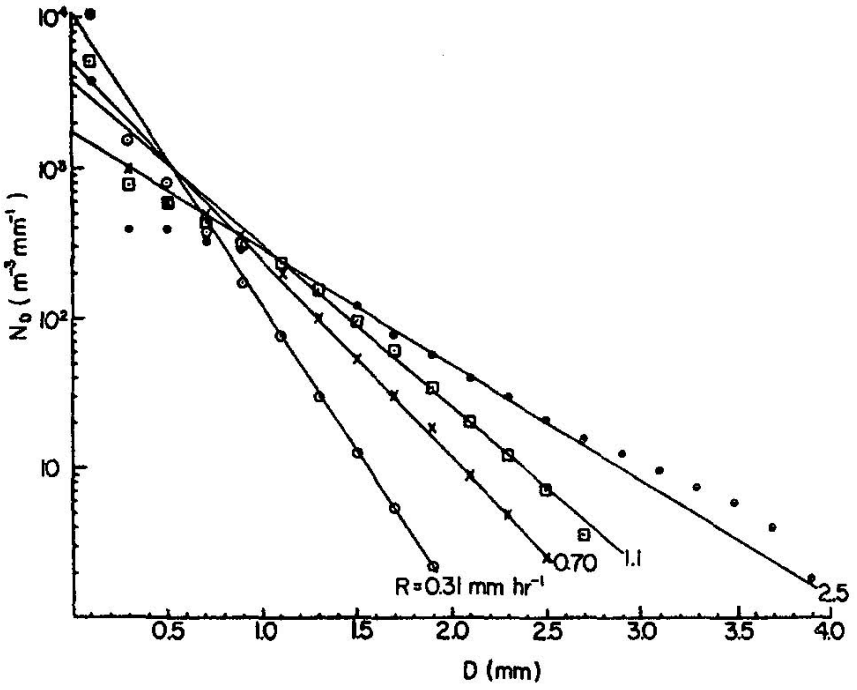

Fig. 2.2: Size distributions for aggregate snowflakes in a semi-log plot for different rainfall rate values fitted by Gunn and Marshall formula. Dots are experimental data. Adapted from: Gunn and Marshall (1958).

rate dependency, namely intercept is not constant and equal to 3.8×10^3 $R^{-0.87}$ $\mathrm{m}^{-3}\mathrm{mm}^{-1}$, whereas $\Lambda_s = 25.5R^{-0.48}$ cm^{-1}. R is expressed in $\mathrm{mm/h}^{-1}$ of liquid water.

Several different formulas were derived from ground observation to express diameter/concentration relationship in solid precipitation (e.g. Sekhon and Srivastava (1970)), finding that snowflakes typically follow an exponential form. That is important, since it allows snow size distribution parameters to be represented in a relative simple way in bulk microphysical scheme, used, for instance, in cloud models (Woods *et al.*, 2008). As a consequence of exponential form, size distributions are usually plotted on semi-log axes in

order to make their behavior clearly shown as straight line (see Fig 2.2).

The exponential behavior is a good approximation especially in aggregate snowfall episodes, but in ice crystal/pristine precipitation events it seems to fail. In these cases particle size distribution appears to agree well with a log-normal distribution (Schlenczek *et al.*, 2017).

In addition, several observations of particle size distributions in winter storms (e.g. Heymsfield *et al.* 2004; Brandes *et al.* 2007) were found also to fit the gamma model (Ulbrich, 1983). This can be expressed as:

$$N(D) = N_0 D^{\mu} exp(-\Lambda D) \tag{2.19}$$

where N_0 ($\mathrm{mm}^{-\mu-1}\mathrm{m}^{-3}$) is a number concentration parameters, μ is the distribution shape or curvature parameter, whereas Λ (mm^{-1}) is a slope term sensitive to large particles.

A power-law-type can describe ice crystal size distributions inside a cloud, in particular cirrus clouds. According to Heymsfield (1975) this relation appears as depicted in equation 2.20. Here, N is the value of number concentration, a and b represented fitting constants, D stands for largest crystal dimension while w_i is the ice water content of the cirrus clouds.

$$N = a w_i D^b \tag{2.20}$$

According to Wang (2013) typically the concentration of ice crystals in cirrus clouds is between $5{\times}10^4$ and $5{\times}10^5$ particles per m^3.

2.2 Electromagnetic theory

2.2.1 Introduction

The scattering consists in a physical process where a particle, hit by an electromagnetic wave, continuously absorbs energy from the incident wave and reradiates that energy in all directions. In this dissertation we concentrate on how solid hydrometeors scatter the electromagnetic waves, thus deriving information on their characteristics. Moreover, scattering matters since it influences, through the interaction between electromagnetic waves and solid/liquid particles, the signal received by a remote sensing instrument (for instance the Micro Rain Radar). These instruments use precisely the interplay between the substance and radiation (e.g. scattering, absorption and emission) to retrieve important features of the atmospheric phenomena such as precipitation.

A brief overview of relevant aspects of the electromagnetic theory as well as scattering processes is given in this chapter. The topics presented in the following pages are in part derived from Bringi and Chandrasekar (2001), Mishchenko *et al.* (2002), Bohren and Huffman (2008), Liou and Yang (2016) and Andronache (2018).

2.2.2 Electromagnetic field equation

The disturbance in space due to the presence of an electric charge is the basis of an electromagnetic field. The latter is governed and mathematically described by a set of equations, the well-know Maxwell's equations (equations 2.21), assuming that the physical properties of the medium are continuous

at every point in its neighborhoods.

$$\nabla \times \mathbf{H} = \frac{1}{c}\frac{\partial \mathbf{D}}{\partial t} + \frac{4\pi}{c}\mathbf{j}, \tag{2.21a}$$

$$\nabla \times \mathbf{E} = -\frac{1}{c}\frac{\partial \mathbf{B}}{\partial t}, \tag{2.21b}$$

$$\nabla \cdot \mathbf{D} = 4\pi\rho, \tag{2.21c}$$

$$\nabla \cdot \mathbf{B} = 0. \tag{2.21d}$$

In these equations $\mathbf{E}$ stands for the electric field, the magnetic induction vector is $\mathbf{B}$, $\mathbf{j}$ represents the electric current density whereas $\mathbf{D}$ and $\mathbf{H}$ the electric displacement and the magnetic vector respectively. Finally t denotes time, c the velocity of light in the vacuum and ρ the local charge density.

It is well-know that an electromagnetic wave is characterized by electric and magnetic vectors $\mathbf{E}$ and $\mathbf{H}$, forming an orthogonal set with the direction of propagation of the wave. Moreover, one of the fundamental properties of these equation is that they make possible to represent, in homogeneous medium, an electromagnetic field by equation 2.22,

$$\mathbf{E}(\mathbf{x}, t) = \mathbf{E}_0 exp[i(\mathbf{k} \cdot \mathbf{x} - \omega t)] \tag{2.22}$$

where $\mathbf{E}_0$ is the amplitude of electromagnetic wave, $\mathbf{k}$ and ω are wave vector and frequency respectively, while $\mathbf{x}$ and t are the spatial and temporal coordinates.

2.2.3 Stokes parameters

Generally optical instruments cannot directly measure the electric and magnetic field associated with a beam of light, they rather measure the intensity of radiation and its polarimetric state. Fundamental examples of these observable quantities are the so-called Stokes parameters. A spherical coordinate system, associated with a local right-handed Cartesian coordinate

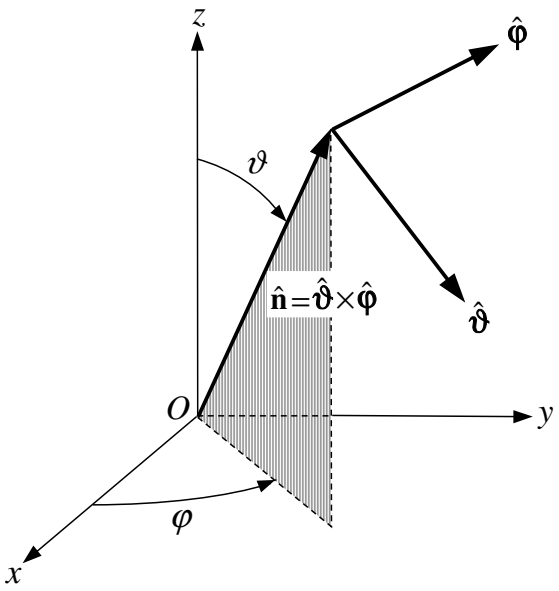

Fig. 2.3: Coordinate system used to described the direction of propagation and the polaritation state of a plane electromagnetic wave. Source: Mishchenko *et al.* (2002).

system with origin in the observation point, is needed with the purpose of defining such parameters. Considering an electromagnetic wave that propagates in a homogeneous and non-absorbing medium, the direction of propagation can be defined by a unit vector $\hat{\mathbf{n}}$ or by a couple of angles (ϑ and φ) (see Figure 2.3). These angles are respectively the zenith angle ($\vartheta \in [0,\pi]$) and the azimuth angle ($\varphi \in [0,2\pi)$). In such case, being the medium assumed as non-absorbing, the component of electrical field along the direction of propagation in equal to zero, so that the electric field at the origin of the axes is given by $\mathbf{E}=\mathbf{E}_{\vartheta}+\mathbf{E}_{\varphi}$. In fact $\mathbf{E}$ can be decomposed into two components representing the electric vectors parallel and perpendicular to a plane trough the direction of propagation. The plane is usually called the plane of

reference.

Thanks to such division it is possible to define a set of four quantities, namely the Stokes parameters. Because intensity is proportional to the absolute square of the electric field, neglecting a constant of proportionality, these parameters are calculated as follow:

$$I = \mathbf{E}_\vartheta \mathbf{E}_\vartheta^* + \mathbf{E}_\varphi \mathbf{E}_\varphi^* \tag{2.23a}$$

$$Q = \mathbf{E}_\vartheta \mathbf{E}_\vartheta^* - \mathbf{E}_\varphi \mathbf{E}_\varphi^* \tag{2.23b}$$

$$U = \mathbf{E}_\vartheta \mathbf{E}_\varphi^* + \mathbf{E}_\varphi \mathbf{E}_\vartheta^* \tag{2.23c}$$

$$V = -i(\mathbf{E}_\vartheta \mathbf{E}_\varphi^* - \mathbf{E}_\varphi \mathbf{E}_\vartheta^*) \tag{2.23d}$$

where asterisk stands for the complex conjugate value. The Stokes parameters I, Q, U, and V are also defined as the elements of 4x1 column vector **I**, known as Stokes vector.

$$\mathbf{I} = \begin{pmatrix} I \\ Q \\ U \\ V \end{pmatrix} \tag{2.24}$$

The vector components have a physical meaning: I represents the total intensity of the electromagnetic wave, Q is the difference in intensity between the horizontal and the vertical modes, U for the $\pm$ 45° modes (i.e. in a reference frame rotated), whereas V stands for intensity difference of the components in the circular reference frame. Moreover, the Stokes parameters of a plane monochromatic wave are not completely independent but rather related by a quadratic identity. Indeed they satisfy equation (2.25)

$$I^2 = Q^2 + U^2 + V^2 \tag{2.25}$$

and also can be expressed in terms of the geometry defining an ellipse, the so-called polarization ellipse.

2.2.4 Scattering by an ice crystal

Atmospheric scattering involves a change in direction of propagation, frequency and/or polarization caused by several interactions with the cloud particles, with the hydrometeors as well as with the atoms in the atmosphere.

The scattering response of a hydrometeor to an incident electromagnetic wave is related to size, shape, orientation, composition (ice, water, mixed phase) of the particle and to the frequency of the incoming radiation. The dielectric constant of relative permittivity (ϵ_r) is a complex number that quantifies the behavior of a material in response to the electromagnetic radiation. Considering a particle with an arbitrary shape, this can be split into very small finite scattering elements, representable as spheres. Applying an incident electric field, a dipole momentum is inducted in the spheres. The dipole momentum is the vector sum of the charge magnitude times the charge separation distance for each sphere summed over the particle. When the incident electric field swings (as in the case of weather radar wave), each tiny dipole will oscillate at the same frequency, transmitting electromagnetic waves in all directions. Hence the total scattered wave can be thought as the sum of these wavelets at a certain distance from the particle.

Before getting in further detail, the size parameter notion can be introduced. This represents the relationship between the particle size and the wavelength of the incident radiation and it is expressed as:

$$x = \frac{2\pi a}{\lambda} \tag{2.26}$$

where a and λ stand for the characteristic dimension of the scattering particle and wavelength of the incident radiation respectively. Size parameter shows the number of complete wave cycles of the radiation per characteristic particle length.

Going into detail, the scattered electric field, at a distance r from an ice particle of arbitrary shape and size, is related to the two components of the incident electric field namely E^i_ϑ and E^i_φ. In the far field, a 2 $\times$ 2 complex scattering amplitude matrix (known as Jones matrix) transforms incident electric vector into the scatter electric vector following the equation:

$$\begin{bmatrix} E^s_\vartheta \\ E^s_\varphi \end{bmatrix} = \frac{exp(-ikr + ikz)}{ikr} \begin{bmatrix} S_2 & S_3 \\ S_4 & S_1 \end{bmatrix} \begin{bmatrix} E^i_\vartheta \\ E^i_\varphi \end{bmatrix} = \begin{bmatrix} A_2 & A_3 \\ A_4 & A_1 \end{bmatrix} \begin{bmatrix} E^i_\vartheta \\ E^i_\varphi \end{bmatrix} \tag{2.27}$$

where $\mathbf{E}^i$ is the incident electric field and $\mathbf{E}^s$ is the scattered field in the far-field (i.e. large distance). Moreover, z represents the vertical direction in Cartesian coordinates, S_j (j=1,2,3,4) are the amplitude functions, whereas A_j is referred to as the transformation matrix. The relation (2.27) expresses that the incident energy interacts with a scattering particle and the scattered energy is related to the distance and to the scattering matrix called Jones matrix. It should be noted that such relation is angle-dependent, namely the matrix changes if the angle between particle and incident wave varies. As seen above, the Jones matrix links, through equation 2.27, the incoming and scattered electric field. Using the Stokes parameter, the Mueller matrix $\mathbf{M}$ connects incoming and outgoing Stokes vectors through the following relationship:

$$\begin{pmatrix} I \\ Q \\ U \\ V \end{pmatrix} = \frac{\mathbf{M}}{k^2 r^2} \begin{pmatrix} I_0 \\ Q_0 \\ U_0 \\ V_0 \end{pmatrix} \tag{2.28}$$

where the subscript 0 indicates the incident beam. The transformation ma-

trix is given by:

$$\mathbf{M} = \begin{pmatrix} M_{11} & M_{12} & M_{13} & M_{14} \\ M_{21} & M_{22} & M_{23} & M_{24} \\ M_{31} & M_{32} & M_{33} & M_{34} \\ M_{41} & M_{42} & M_{43} & M_{44} \end{pmatrix} \tag{2.29}$$

and in particular its components come from the subsequent relationship:

$$M_{11} = \frac{1}{2}(|S_2|^2 + |S_3|^2 + |S_4|^2 + |S_1|^2) \tag{2.30a}$$

$$M_{12} = \frac{1}{2}(|S_2|^2 - |S_3|^2 + |S_4|^2| - S_1|^2) \tag{2.30b}$$

$$M_{13} = S_{23} + S_{41} \tag{2.30c}$$

$$M_{14} = -D_{23} - D_{41} \tag{2.30d}$$

$$M_{21} = \frac{1}{2}(|S_2|^2 + |S_3|^2 - |S_4|^2 - |S_1|^2) \tag{2.30e}$$

$$M_{22} = \frac{1}{2}(|S_2|^2 - |S_3|^2 - |S_4|^2 + |S_1|^2) \tag{2.30f}$$

$$M_{23} = S_{23} - S_{41} \tag{2.30g}$$

$$M_{24} = -D_{23} + D_{41} \tag{2.30h}$$

$$M_{31} = S_{24} + S_{31} \tag{2.30i}$$

$$M_{32} = S_{24} - S_{31} \tag{2.30j}$$

$$M_{33} = S_{21} + S_{34} \tag{2.30k}$$

$$M_{34} = -D_{21} + D_{34} \tag{2.30l}$$

$$M_{41} = D_{24} + D_{31} \tag{2.30m}$$

$$M_{42} = D_{24} - D_{31} \tag{2.30n}$$

$$M_{43} = D_{21} + D_{34} \tag{2.30o}$$

$$M_{44} = S_{21} - S_{34} \tag{2.30p}$$

It should be noted that the terms given by such equations are functions of

the amplitude scattering matrix elements in the following ways:

$$S_{jk} = \frac{(S_j S_k^* + S_k S_k^*)}{2} \tag{2.31a}$$

$$D_{jk} = i\frac{(S_j S_k^* - S_k S_k^*)}{2} \tag{2.31b}$$

Moreover, it is worth mentioning that in the Mueller matrix only seven elements are independent, corresponding to the four amplitudes and three phase differences of the S_j. The first element of the transformation or the Mueller matrix allows also to define the scattering cross section by equation 2.32.

$$\sigma_s = \frac{1}{k^2}\int_0^{2\pi}\int_0^{\pi} M_{11} sin\Theta d\Theta d\phi \tag{2.32}$$

Here Θ and ϕ stand for the scattering angle, the former, and the azimuthal angle, the latter. The scattering cross section is an important feature as it represents the amount of the incident energy that is removed from the original path as result of a single scattering episode. In that way this flux is distributed over a sphere area where the scatterer is on the center. Moreover it is useful to introduce the scattering phase matrix $\mathbf{P}$, that, if no assumption is made about position and habit of the scattering element, is formed by 16 non zero elements. In the definition the first elements is normalized to unity in the subsequent way:

$$\int_0^{2\pi}\int_0^{\pi} \frac{P_{11}(\Theta)}{4\pi} sin\Theta d\Theta d\phi = 1 \tag{2.33}$$

In addition, the scattered Stokes terms can be written using the scattering phase matrix

$$\begin{pmatrix} I \\ Q \\ U \\ V \end{pmatrix} = \Omega_{eff}\frac{\mathbf{P}}{4\pi}\begin{pmatrix} I_0 \\ Q_0 \\ U_0 \\ V_0 \end{pmatrix} \tag{2.34}$$

where Ω stands for the effective solid angle associated with the scattering and it is equal to σ_s/r^2.

In the atmospheric remote sensing we have to deal with groups of solid hydrometeors, thus also the scattering by a group of ice crystals is discussed in this thesis. In this case orientation and dimensions of each crystal with respect to the incident wave influence the total scattering. Considering a sample of non-spherical ice crystals of same size and oriented in a random way, the scattering phase matrix can be written as follows:

$$\mathbf{P}(\Theta) = \frac{1}{2\pi\sigma_s} \int_0^{2\pi} \int_0^{\pi} \mathbf{P}'(\alpha', \gamma') \sigma_s'(\alpha', \gamma') sin\alpha' d\alpha' d\gamma' \tag{2.35}$$

here $\mathbf{P}'$ represents the scattering phase matrix for a single crystal, whereas α' and γ' are the orientation angles respect to the incident beam. Also the relationship for the scattering cross section (equation 2.32) can be generalized as

$$\sigma_s = \frac{1}{2\pi} \int \int \sigma_s'(\alpha', \gamma') sin\alpha' d\alpha' d\gamma' \tag{2.36}$$

where σ_s' stands for single particle cross section. Further, considering ice crystals that are randomly oriented in space, the law of reciprocity can be applied, meaning that the directions of the incident and scattered polarized beams can be reversed to achieve the same result. As a consequence the amplitude functions (see equation 2.27) (S_3, S_4) must be equal to ($-S_4$, -S_3). As discuss earlier in the relationship 2.34, the scattering phase matrix sets out scattered and incident Stokes vector:

$$\begin{pmatrix} I \\ Q \\ U \\ V \end{pmatrix} = \frac{\Omega_{eff}}{4\pi} \begin{pmatrix} P_{11} & P_{12} & P_{13} & P_{14} \\ P_{21} & P_{22} & P_{23} & P_{24} \\ P_{31} & P_{32} & P_{33} & P_{34} \\ P_{41} & P_{42} & P_{43} & P_{44} \end{pmatrix} \begin{pmatrix} I_0 \\ Q_0 \\ U_0 \\ V_0 \end{pmatrix} \tag{2.37}$$

Taking a sample of particles inside an arbitrarily volume and indicating as $\mathbf{P}$ their scattering phase matrix, a same number of reciprocal particles with $\mathbf{P}^*$ as scattering phase matrix can be considered always in the same volume. Therefore an average scattering phase matrix $\langle\mathbf{P}\rangle$ can be obtained as $(\mathbf{P} + \mathbf{P}^*)/2$, and has the property to be proportional to this transformation matrix:

$$\langle\mathbf{P}\rangle = \begin{pmatrix} \langle P_{11}\rangle & \langle P_{12}\rangle & \langle P_{13}\rangle & \langle P_{14}\rangle \\ \langle P_{21}\rangle & \langle P_{22}\rangle & \langle P_{23}\rangle & \langle P_{24}\rangle \\ \langle P_{31}\rangle & \langle P_{32}\rangle & \langle P_{33}\rangle & \langle P_{34}\rangle \\ \langle P_{41}\rangle & \langle P_{42}\rangle & \langle P_{43}\rangle & \langle P_{44}\rangle \end{pmatrix} \tag{2.38}$$

where the different terms are linear combinations similar to what seen in equations 2.31 and 2.30. Some properties, also, permit to simplify the matrix. Indeed, thanks to these six equivalences (i.e. $\langle P_{12}\rangle = \langle P_{21}\rangle$, $\langle P_{13}\rangle = \langle -P_{31}\rangle$, $\langle P_{14}\rangle = \langle P_{41}\rangle$, $\langle P_{23}\rangle = \langle -P_{32}\rangle$, $\langle P_{24}\rangle = \langle P_{42}\rangle$, and $\langle P_{34}\rangle = \langle -P_{43}\rangle$) the scattering phase matrix becomes:

$$\langle\mathbf{P}\rangle = \begin{pmatrix} \langle P_{11}\rangle & \langle P_{12}\rangle & \langle P_{13}\rangle & \langle P_{14}\rangle \\ \langle P_{21}\rangle & \langle P_{22}\rangle & \langle P_{23}\rangle & \langle P_{24}\rangle \\ \langle -P_{13}\rangle & \langle -P_{23}\rangle & \langle P_{33}\rangle & \langle P_{34}\rangle \\ \langle P_{14}\rangle & \langle P_{24}\rangle & \langle -P_{34}\rangle & \langle P_{44}\rangle \end{pmatrix} \tag{2.39}$$

The scattering phase matrix contains ten independent terms, but considering the previous relationships and a sample of randomly oriented ice particles which have a plane of symmetry, the scattering matrix of an ice crystal is reduced to six independent elements.

$$\langle\mathbf{P}\rangle = \begin{pmatrix} \langle P_{11}\rangle & \langle P_{12}\rangle & 0 & 0 \\ \langle P_{12}\rangle & \langle P_{22}\rangle & 0 & 0 \\ 0 & 0 & \langle P_{33}\rangle & \langle P_{34}\rangle \\ 0 & 0 & \langle -P_{34}\rangle & \langle P_{44}\rangle \end{pmatrix} \tag{2.40}$$

The matrix is formed by only four independent elements in the case of a spherical particles.

These considerations allow to define the scattering phase matrix and scattering cross section also in the case of a particle size distribution. Indeed, considering a size distribution $n(D)$, with D the major axis of an ice particle, the scattering phase matrix associated with a suitable volume is written as:

$$\mathbf{P}(\Theta) = \frac{\int_{D_1}^{D_2} \mathbf{P}(\Theta, D)\sigma_s(D)n(D)dD}{\int_{D_1}^{D_2} \sigma_s(D)n(D)dD} \tag{2.41}$$

that represents the dimension limits of particle size. Finally, the scattering cross section of a group of ice crystals represented by a size distribution is obtained in the following equation:

$$\sigma_s = \frac{\int_{D_{min}}^{D_{max}} \sigma_s(D)n(D)dD}{N} \tag{2.42}$$

where N stands for the total number of ice crystals in the given volume.

2.2.5 Backscattering cross section

In this dissertation, as in radar meteorology, the backscattering cross section or radar cross section is considered and evaluated. It represents the amount of the incident wave scattered from the object in the direction toward the source of the incident irradiance or the amount of radiation scattered back toward the radar from a target. Because the exact characteristics of the scatterer are unknown, it is assumed that the received power is from an hypothetical target that scatters radiation isotropically.

In order to define the backscattering cross section, the statement in Bohren and Huffman (2008) was followed. Considering an electromagnetic beam with irradiance I_i that illuminates an arbitrary particle and indicating as $\mathbf{X}$ the vector scattering amplitude for the particle, the quantity

$I_i|\mathbf{X}(\theta,\phi)|^2/k^2$ is the amount of energy scattered into a solid angle about a particular direction (θ,ϕ). Indeed, the vector scattering amplitude, in the case where a hypothetical isotropic scatterer illuminated by the same beam is considered, is direction independent and is equal to the scattering amplitude in the backscattering direction ($\theta = 180°$) $\mathbf{X}_{iso} = \mathbf{X}(180°)$. Indicating with W_{sca} the total energy scattered in all direction, this is equal to:

$$W_{sca} = \frac{I_i 4\pi |\mathbf{X}_{iso}|^2}{k^2} \tag{2.43}$$

Hence the definition of the backscattering cross section is achieved as follows:

$$\sigma_b = \frac{4\pi |\mathbf{X}(180°)|^2}{k^2} \tag{2.44}$$

Moreover, being the backscattering cross section expressed in units of area, this could make it difficult to compare different scattering properties of several particles with various dimensions. This is the reason why often the cross section is normalized into nondimensional units. This operation consists in dividing the cross section by the project area of the scattering particle and the quantity Q_b, known as backscattering efficiency, is attained. Its definition through the backscattering cross section is:

$$Q_b = \frac{\sigma_b}{\pi a^2} \tag{2.45}$$

where a is the dimension of the particle.

Furthermore, numerical values of the backascattering cross section for ice crystal particles with so different and irregular shapes and dimensions, are pretty hard to compute. In order to obtain such values, approximate solution methods are used whose results can be stored in precompiled databases. These are presented and investigated in some depth in the next chapter. On the other hand numerical values are easy to achieve in the case of Rayleigh

scattering, namely when the scattering particle dimensions are small compared to the radiation wavelength and hence size parameters are smaller than unit. Specifically it is possible to calculate the backscattering cross section as:

$$\sigma_b = \frac{\pi^5}{\lambda^4} D^6 |K|^2 \tag{2.46}$$

with λ the radar wavelength and K the dielectric factor expressed in the following equation:

$$|K|^2 = \left| \frac{m^2 - 1}{m^2 + 2} \right|^2 \tag{2.47}$$

where m stands for the complex refractive index. The most remarkable feature of the Rayleigh scattering is the sensitivity to the scatterer dimension, being proportional to the sixth power of particle size. For operational weather radars that transmit at S or C electromagnetic bands, many cloud and precipitation particles can be considered small with respect to the wavelength and hence this simple approximation can be used. Instead, for high frequency radar (i.e. K or W bands) as well as for the largest raindrops and large melting ice particle such as hail and snow aggregate Rayleigh scattering can no longer be applied.

Chapter 3

Data and Methods

The descriptions of the instruments used in this dissertation, the scattering methods evaluated as well as the methodology followed in order to obtain the hydrometeors classification, are presented in this chapter.

3.1 Data

3.1.1 Micro Rain Radar (MRR)

Weather radars typically operate at frequencies in X, C or S bands, namely where precipitation particles fall within the Rayleigh approximation. Instead, in order to investigate clouds, higher frequency systems (e.g. W, Ka and Ku bands) are used, the so-called cloud-radars. The use of high frequencies limited to cloud observations is due to the high values of attenuation of the radar beam represented by the liquid hydrometeors, although ice attenuation is lower hundred times than water depending on frequency (Kneifel *et al.*, 2011). If the atmospheric layers of interest are narrowed to the lowest portion of atmosphere (namely up to 5-6 km), a possible solution can be represented by using a cloud vertically profiling radar that operates in the K-band, 24

GHz (λ=1.24cm), such as the Micro Rain Radar.

The Micro Rain Radar 2 used in this work (hereinafter MRR), manufactured by Metek GmbH, is a vertically pointing frequency modulated continuous wave (FM-CW) profiling Doppler radar and is able to estimate Doppler spectra in 64 bins over 32 ranges (only 6 in the previous version of the instrument, the MRR-1). Normally, FM-CW radars need to use two separate antennas, one for transmitting and one for receiving. However in the MRR, the backscattered signal is detected and received with the same antenna assembly (monostatic radar). The core component of the radar is a gunn-diode-oscillator with integrated mixing diode with 50 mW as nominal transmit power. The simple configuration cannot be operated in pulsed mode, because during the shut off of the transmitter, also the receiver does not work. In the mixing diode, the backscattering radiation and the transmitted signal produce two different frequencies. This frequency shift depends on the distance of the targets from the radar and on the falling velocities of the hydrometeors (Löffler-Mang *et al.*, 1999). As opposed to the pulsed radar technology, such small amount of peak power is enough for FM-CW radars. Moreover, the MRR has a compact design (being composed only of a dish with a diameter of approximately 60 cm and with a beam width of 1.8°), a low power consumption and with plug-and-play installation that make the MRR suitable for placement in remote regions, such as Antarctic research stations (Gorodetskaya *et al.*, 2015). The working block diagram and a summary of the technical specifications of MRR are reported in Figure 3.1 and Table 3.1, respectively.

By properly processing power spectra collected in rain, the MRR allows to estimate the vertical profiles of drop size distributions and, from these, the rain rates, liquid water content and characteristic falling velocity of hydrom-

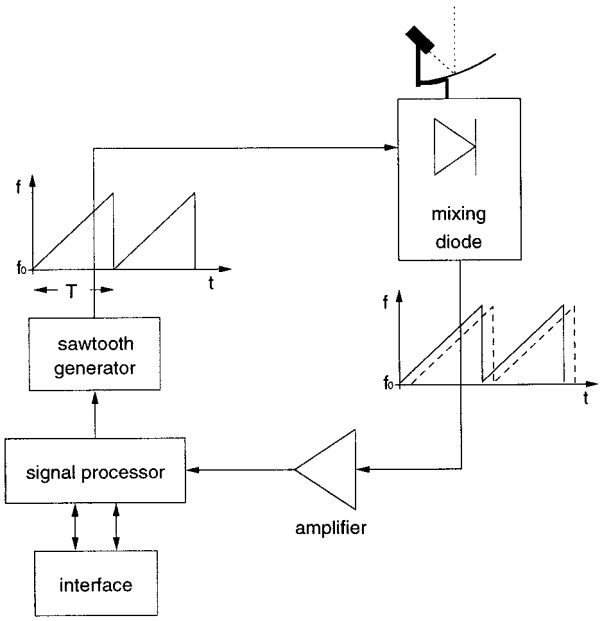

Fig. 3.1: Working block diagram of the Micro Rain Radar. Source: Löffler-Mang *et al.* (1999).

eteors can be derived (Metek, 2010). The Micro Rain Radar was originally developed to measure precipitation at buoys in the North Sea, not being affected by sea spray (Maahn and Kollias, 2012), then was used to observe rain, bright band and snow.

As said previously, MRR is not a pulsed radar, so the distance from a target to the instrument must be obtained in a different way rather than measuring the time between transmitted and received signal. Indeed, in order to calculate the range resolution, the electromagnetic beam is sent modulating its frequency. In this way, the distance of the target (or, in other words, the time delay of the return signal) is achieved by the frequency shift between the output and input signals.

(Richter, 1969) and Chadwick *et al.* (1976) proposed and introduced the processing procedure of the FM-CW radars. Going into detail, following

Instrument	**METEK Micro Rain Radar 2**
Operating mode	FM-CW Doppler
Spatial coverage	Vertically profiling
Centre frequency	24 GHz (λ=1.24 cm)
Frequency modulation	0.5 - 15 MHz
Nominal transmit power	50 mW
Antenna dish	60 cm offset parabolic dish
Measurement range	100 m - 3.1 km (at 100 m resolution)
No. of range gates	32
Measurement resolution	selectable form 30 m to 300 m
Environment resolution	Operational between -40° and +60°C; wind speed up to 45 m/s
Power consumption	25 W

Table 3.1: Main technical specifications of the Micro Rain Radar.

Metek (2010), the transmitted pulse is modulated through a linearly decrease of frequency, resembling a saw-tooth (see Figure 3.2). The received signal has a higher frequency than the transmitted one due to the time lag and this difference is proportional to the target distance. The frequency sweeps linearly around a central frequency f_0, from $f_0 + B/2$ to $f_0 - B/2$ and then jumps back to the initial value after T, the time of a full frequency sweep. The travel (delay) time of the response pulse can be expressed as $t_h = 2h/c$, where h is the target distance and c the speed of light. One of the main features of MRR radars is to mix in the receiver, the received signal with the signal at the output of transmitter. From a mathematical point of view, this mixing characteristic results in a multiplication of the two signals.

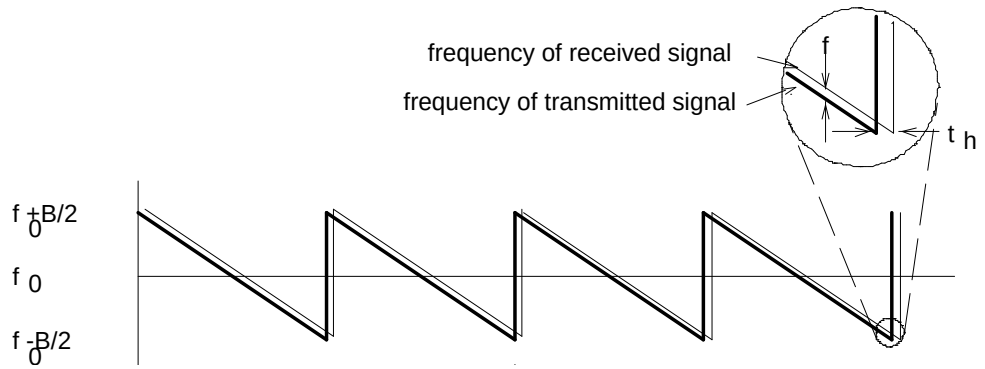

Fig. 3.2: Frequency of the transmit signal and the echo. Here t_h represents the travel (delay) time of the response pulse. Source: Metek (2010).

Exploiting trigonometric equations, the mixed frequency can be expressed as sum and difference of the two frequencies. Then, being frequency difference smaller than the central frequency f_0, its contribution to the mixing signal is suppressed by a low pass filter. The frequency of the mixing signal is derived by differentiation of its phase with respect to time, obtaining:

$$f_m = B\frac{t_h}{T} \tag{3.1}$$

Using the travel time relation, equation 3.1 can be easily written as:

$$f_m = \frac{2hB}{T} \tag{3.2}$$

Moreover, the signal returned from a moving target (as the precipitation particles are) adds to the mixing frequency another frequency term due to Doppler effect. Being the MRR a vertically pointed radar, the measured Doppler velocity is assumed to be equivalent to the hydrometeor fall speed. In fact, drop falling velocity, relative to the stationary antenna, produces a term of frequency deviation between transmitted and received signals and this term is a measure of the particle speed. It is well-know that rain drops of different diameter have different falling velocities depending on their diameter(Atlas

et al., 1973), and hence the backscattered signal consists of a distribution of different Doppler frequencies. The spectral analysis of this signal yields a wide distribution of lines corresponding to the Doppler frequencies of the signal (Oluwadare *et al.*, 2010). Summing the above mentioned two terms, the total frequency shift is obtained:

$$\Delta f_{total} = \frac{2}{\lambda} v + B \frac{2h}{cT} \tag{3.3}$$

here the first term on the right-hand side of the equation stands for the Doppler effect, whereas the second one accounts for the range. Thus, an ambiguity between the velocity of the particle and particle range appears and makes it impossible to distinguish between each contribution. Actually this statement is true only if a single sweep is considered. Indeed, contemplating several sweeps and using the Fourier transformation, it is possible to distinguish the two frequencies, obtaining a reflectivity matrix hosting 64 frequency intervals and 32 range gates. A more completed description of this method is included in Metek (2010). According to Maahn and Kollias (2012), of these 32 ranges, only 28 are typically taken into account. The first one is removed as it corresponds to the height of 0 meters. Near field effects affect the second and the third gates, hence they are eliminated. Whereas, the last one is generally cut due to the high noise level. The remaining 28 exploitable ranges lead to a maximum observable height that spans between 300 and 6000 meters depending on the choice of vertical resolution. The latter ranges from 10 to 300 meters adjusting the frequency modulation from 0.5 to 15 MHz.

The drop size distribution is derived by MRR from the raw spectral power received by the radar, given as

$$f(n,i) = \frac{10^{20} TF(i)}{C} \frac{1}{i^2 \Delta h} \eta(n,i) \tag{3.4}$$

where n and i are the numbers of Doppler spectrum and range gates respectively, TF is the transfer function that compensates for the dependence of amplification on frequency (Diederich *et al.*, 2004) and C stands for the device specific calibration constant. Δh and η represent, instead, the range resolution and the spectral reflectivity namely the backscattered cross section per volume. Considering that the frequency resolution of Doppler spectra is $\Delta f = 30.52$ Hz, the corresponding velocity resolution is $\Delta v = \Delta f \cdot \lambda/2 = 0.1905$ m/s. As said above, in order to achieve DSD, MRR takes advantage of the following relation between terminal fall velocity and drop diameter that has been found empirically by Gunn and Kinzer (1949) and then put in analytic form by Atlas *et al.* (1973):

$$v(D) = (9.65 - 10.3e^{-0.6D})\delta v(h) \tag{3.5}$$

here D stands for drop diameter and the height dependent density correction, $\delta v(h)$, is included. Then, through velocity resolution, the spectral reflectivity density with respect to velocity is obtained:

$$\eta(v, i) = \frac{\eta(n, i)}{\Delta v} \tag{3.6}$$

successively, the spectral reflectivity density is gathered with respect to drop diameter deriving the relation 3.5

$$\eta(D, i) = \eta(v, i)\frac{\partial v}{\partial D} \tag{3.7}$$

and, finally, dividing $\eta(D, i)$ by the backscattering cross section of a single rain drop, the drop size distribution is calculated:

$$N(D, i) = \frac{\eta(D, i)}{\sigma(D)} \tag{3.8}$$

As MRR wavelength is not so small compared to the natural drop dimensions, the Rayleigh approximation to compute the backscattering cross section (see

equation 2.46) is not applicable. Hence $\sigma(D)$ is calculated via Mie theory (Löffler-Mang *et al.*, 1999). Moreover, the Micro Rain Radar gains even the radar reflectivity Z by integrating the $N(D)$ of equation 3.8:

$$Z = \int N(D) D^6 dD \tag{3.9}$$

and again the precipitation rate is achieved via drop size distribution instead of using a Z-R relationship:

$$R = \frac{\pi}{6} \int N(D) D^3 v(D) dD \tag{3.10}$$

As pointed out by Kneifel *et al.* (2011) and Maahn and Kollias (2012), the standard radar variables evaluated by MRR had to be modified in order to measure solid precipitation, since the MRR was originally designed only for rain observations. Indeed, the operational software of MRR automatically derives mean fall velocities, rain DSD, rain rate and radar reflectivity factor assuming liquid hydrometeors. As highlighted above, DSD is derived from the assumption of a rain drop size-falling velocity relation. Moreover, in equation 3.8 the backscattering cross sections are calculated by Mie approximation supposing water spheres. As widely discussed in section 2.1, both these assumptions are totally unrealistic when we deal with solid precipitation. In fact, for snow particles, the dependence of velocity from size is rather complicated, and it heavily depends on the different habits. Moreover, the backscattering properties are largely dependent on ice particle shapes and densities. Thus, in this dissertation, similarly to Kneifel *et al.* (2011), instead of using Z obtained from $N(D)$, used is the effective reflectivity factor (Z_e) calculated by directly integrating the Doppler spectrum measured by MRR:

$$Z_e = 10^{18} \frac{\lambda^4}{\pi^5 |K^2|} \int \eta(v) dv \tag{3.11}$$

Fig. 3.3: Micro Rain Radar at Mario Zucchelli research station on the roof of the logistic container.

where $|K^2|$ is a function of the dielectric properties of liquid water at the freezing point, v the Doppler velocity and η the spectral reflectivity. In addition, in order to improve the MRR sensitivity, also the post-processing methodology of Maahn and Kollias (2012) was applied to the MRR data. This procedure, specifically devised for snow observations, allowed to increase the minimum detectable range to -14 dBz together with a noise removal procedure.

MRR Data at MZS

In the framework of the APP-PNRA project, a MRR was installed on the roof of a logistic container at the Mario Zucchelli research station in November 2017 (see Figure 3.3). It was set with a vertical resolution of 25 meters in order to explore, with dense range gates, the atmospheric layers closer to the ground from 75 meters to 750 meters above ground level. Unfortunately, once put into operation, a receiver fault happened. Repair required the

MRR to be sent back to the manufacturer. The MRR has been repaired by Metek company and will be sent again to MZS in the next Italian Antarctic expedition.

In this work the radar data were kindly provided by ENEA (Dr. Scharchilli) that managed another MRR at MZS. This is operating continuously since November 2016 at "Campo Meteo", about 200 meters from the logistic container. A vertical resolution of 100 meters has been chosen for the Enea-MRR, that allows measurements over 3 km in height, with the first exploited range gate at 300 meters above ground level.

The MRR provides three different data products: Proccessed Data, Average Data and Raw Spectra. The first contains measurement quantities, among others, radar reflectivity. Average Data is identical to Proccessed but averaged over user-selectable time interval (>10 s), whereas Raw Spectra gives Doppler spectra densities without any correction. In this study the Raw Spectra data were used, with a time interval of 60 seconds. Data were autmatically processed by a noise suppression procedure (Adirosi *et al.*, 2016), by the methodologies of Kneifel *et al.* (2011) and Maahn and Kollias (2012) and by an attenuation correction (Peters *et al.*, 2010).

Data were stored in a laptop connected to the MRR and sheltered inside the container (Figure 3.4), from which it is possible to manage the radar. At the end of the Italian expedition in Antarctica at MZS, that lasts typically from November to February each year, the annual data are taken to Italy and then analyzed. This is because, at the moment, bandwidth of the internet connection from that remote place, does not allow such large files be sent via web.

The MRR data are originally in ASCII format, by Maahn and Kollias (2012) procedure they are converted into netCDF format, which permits

Fig. 3.4: Control computer of Micro Rain Radar at MZS (on left). White box in the middle is the Junction Box. It is used to pass through the communication between the PC and the RCPD (Radar control and processing device and transceiver) mounted on MRR dish.

storing measurements in the forms of arrays. One Average file each day is produced by MRR, containing information about time and heights as well as radar quantities. Among the latter, Z_e data and spectral reflectivity with respect to velocity were considered in this thesis. The former is organized as a matrix composed by 31×1440 elements, each of them representing an effective reflectivity value in dBz. The range gates considered were 31 as the ground one is not included. The second and third ranges were composed by zero values and then eliminated, instead the last gate was evaluated inasmuch had a sufficient signal to noise ratio. The number 1440 refers to the

number of the minutes in a day. The spectral reflectivity was represented by a three-dimensional matrix (192×31×1440) and expressed in mm^6/m^3. 192 stands for the hydrometeor velocity ranges calculated using the de-aliasing procedure of Maahn and Kollias (2012).

By a specific Matlab script, data from two Italian Antarctic expeditions (32nd and 33rd) were analyzed in this work, covering two southern summers, specifically from November 2016 to February 2017 and from November 2017 to February 2018. Browsing MRR Z_e measurements, 22 precipitation days were identified (more than 1 hour of precipitation at the lower MRR level). The use of radar to identify these events was fundamental since other instruments (e.g. disdrometer, bucket rain gauge) fail in this task because, being located near the terrain and observing phenomena at ground level, they are heavily affected by blowing snow effect, a well-know feature of Antarctic climate, that can produces phantom precipitation.

With the purpose of characterizing the falling hydrometeors at MZS, exploiting the backscattering difference behavior between the hydrometeors, the effective reflectivity from MRR was also compared with a simultaneous and simulated Z_e in which Parsivel data and backscattering methods were used. This methodology is described in section 3.2.3.

As extensively discussed in section 2.1.7, clumping process is the growth mechanism by which an ice crystal can capture other solid particles. In this circumstance, a key role is played by the fall speed of the hydrometeors. Generally, a high spread of such speeds among falling particles during precipitation results in favoring clumping. In fact, supposing two colliding particles with a small falling velocity difference, this would imply an extended interaction time. During this time other factors (e.g. air motions, wind) could distance the two ice crystals resulting in a non-clumping collision. The cir-

cumstance is completely opposed in a high speed difference situation, where the collision has much of chance to determine an aggregate particle. So, in order to qualitatively analyze the hydrometeor speed spread during a precipitation event and to account for turbulence effects due to windy conditions, the spectral reflectivity with respect to velocity was considered in the following analysis.

3.1.2 Parsivel disdrometer

The measurement of size and velocity of falling particles is a challenging and essential task for the scientific community. Different techniques (e.g. impact, imaging, scattering, optical) are described in the literature and have been experimented over the years. Each technique gives advantages and drawbacks that must be carefully evaluated on the basis of the observed precipitation type.

The Particle Size and Velocity (hereafter Parsivel) is an optical disdrometer produced by OTT GmbH, for simultaneous measurements of size and fall velocities of the hydrometeors. It is easy to handle, robust and low cost, hence could be used extensively in a disdrometer network in order to investigate the small scale variability of precipitation (Löffler-Mang and Joss, 2000). The observations are carried out using a sensor head that was developed for this particular purpose (OTT, 2017b). It consists of a sensor that produces a horizontal strip of light. The light-sheet has a size of 30 mm wide, 1 mm high and 180 mm long, producing a horizontal sampling area of 54 cm^2 and this is done by a 780 nm laser diode with a power of 3 mW (Löffler-Mang and Blahak, 2001). The transmitter focuses the light sheet on a single photo diode included in the receiver.

The Parsivel functional principle is quite simple (Figure 3.5). In the

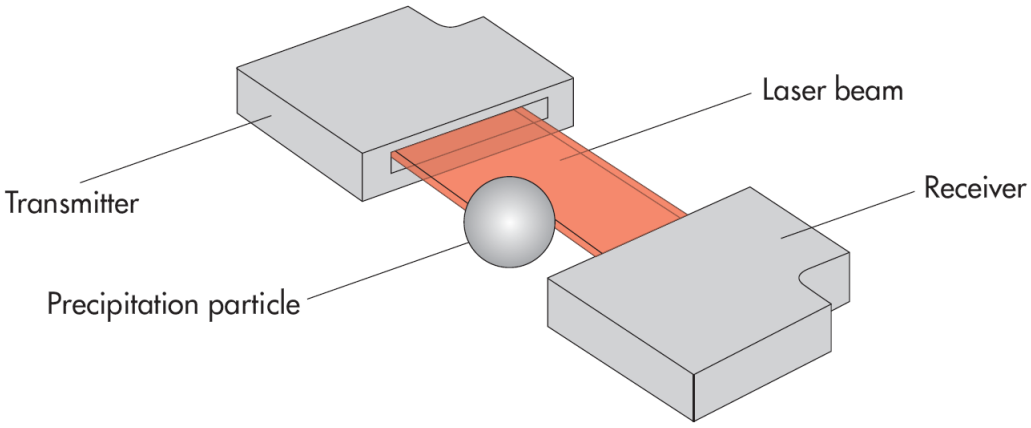

Fig. 3.5: Functional principle of Parsivel. Source:OTT (2017b).

absence of particles the receiver produces the maximum voltage signal (5 Volt) from the sensor output. When a hydrometeor falls crossing the laser beam, it produces a decrease of the output voltage due to the light extinction. By the amplitude of the voltage decrease, particle size can be measured as well as the duration of signal deviation allows an estimate of particle velocity by assuming a fixed relationship between the horizontal and the vertical dimensions. The signal starts with the particle entering the light sheet and ends when the particle has completely exited the light sheet. The distance of influence of a particle is given by the light sheet thickness of 1 mm plus the particle diameter (Löffler-Mang and Joss, 2000). The modification of the signal due to small/large particle is depicted, as schematic example, in Figure 3.6.

A spherical/spheroidal particle shape is assumed for the particle, so the diameter corresponds to the width of the maximum blocked area (Löffler-Mang and Joss, 2000). The Parsivel size and drop retrieval concept has been tuned to raindrops (Battaglia *et al.*, 2010). Indicating with D the particle

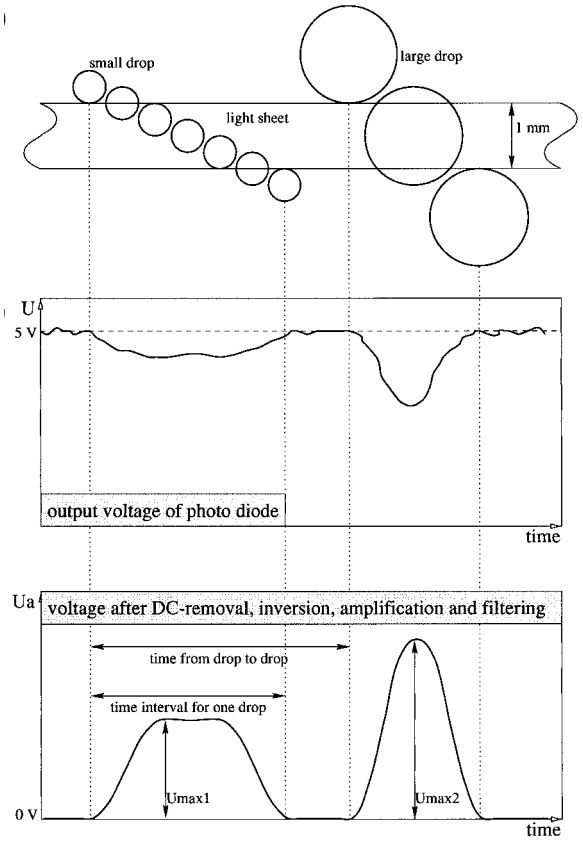

Fig. 3.6: Signal modification due to falling of large/small particle (upper plate); related raw signal outputs (middle plate); inverted and amplified signal (lower plate). Source: Löffler-Mang and Joss (2000).

diameter, hydrometeors with $D<1$ mm are assumed to be spherical, so with an axis ratio (defined as the ratio between height and width) equal to 1. In particles in the range from 1 to 5 mm, the assumed axis ratio varies linearly from 1 to 1.3 (Yuter *et al.*, 2006) and are assumed to be horizontally oriented oblate spheroids (Battaglia *et al.*, 2010). For drops larger than 5 mm, the axis ratio is set to 0.7 (Tokay *et al.*, 2014). Generally, rain drops are assumed to be symmetric in the horizontal plane. Moreover, because of the possibility for two particles to be in the laser beam at the same time, a correction is applied

to estimate the correct concentration of drops (Löffler-Mang and Joss, 2000). In the case of moderate rain, typically, the juxtaposition of particles is not a problem, whereas in heavy rain or rain with a large number of drops, that could be an important issue and hence the correction has to be applied.

The size and fall speed for every particle detected over the measuring period are tabulated in an array whose dimensions are the number of size bins by the number of fall speed bins (Yuter *et al.*, 2006). Parsivel can measure sizes up to about 26 mm and uses 32 size bins of different widths, ranging from 0.125 and 3 mm. The lowest two size classes are not used at all because of their low signal to noise ratio (Chen *et al.*, 2011). So, the observations starts at the third size bin (0.25 mm). Small drops are hence dependably detected, representing an important feature in the investigation of scavenging and chemical effects of precipitation (Löffler-Mang and Joss, 2000). Also the velocity is sorted into 32 speed classes, ranging from 0.05 to 20 m/s, with different bin widths ranging from 0.1 to 3.2 m/s. Thanks to this velocity-dimension array and exploiting the characteristic size-speed relationships for different hydrometeors (e.g. Gunn and Kinzer (1949); Locatelli and Hobbs (1974)), Parsivel can be used as present weather sensor. Each hydrometeor class occupies a defined position in the size-velocity matrix (see an example in Figure 3.7). Particles are categorized as: drizzle, drizzle with rain, rain, rain and drizzle with snow, snow, snow grains, soft hail and hail.

From its size-velocity array, the Parsivel reconstructs the drop size distribution or particle size distribution in case of solid precipitation (see section 2.1.9). Parsivel accumulates the concentration of hydrometeors (i.e. $n(D, v)_{ij}$) per diameter and fall velocity class over a predefined sampling time for each diameter size interval i and fall velocity interval j. Then, the instrument converts the number concentration for each bin, that is counted

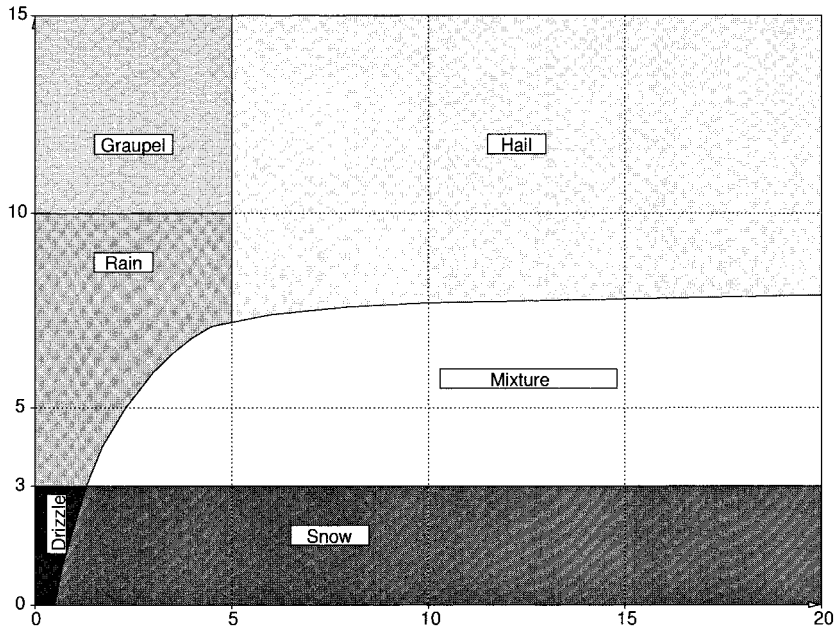

Fig. 3.7: Semplified hydrometeors classification based on size and velocity values. X-axis particle dimension (mm), y-axis particle speed (m/s). Source: Löffler-Mang and Joss (2000).

by area and time, to a volume distribution (Löffler-Mang and Blahak, 2001) by the following equation:

$$N(D,v)_{ij}(mm^{-1}m^{-3}) = \sum_{ij} \frac{10^6 n(D,v)_{ij}}{180mm(30mm - 0.5D_i)v_j \Delta D_i \Delta t} \qquad (3.12)$$

where the time span is represented by Δt, ΔD_i is the width of the i^{th} diameter bin, v_j the terminal fall velocity of class j^{th}, whereas other terms at denominator stand for sampling measuring area. Then, for each diameter class, number concentrations are summed over all the velocity classes in order to obtain $N(D)_i$. In addition, as the Micro Rain Radar, Parsivel provides the radar reflectivity factor Z and the precipitation rate R, and some other information as kinetic energy and visibility that can be obtained from Parsivel software. In particular, in an identical manner as MRR (see equa-

tions 3.9 and 3.10), the Parsivel achieves Z and R through the integration of particle size distribution and considering a power of hydrometeor diameter. Actually, in the case of Parsivel, in order to calculate the reflectivity, this can be evaluated as a sum over discrete quantities as:

$$Z = 10log_{10} \sum_{i} N(D)_i D_i^6 \Delta D_i \tag{3.13}$$

here D_i and ΔD_i represents the mean diameter and the width of the i^{th} diameter bin, whereas $N(D)_i$ stands for binned particle size distribution.

According to OTT (2017b), Parsivel would achieve an accuracy rate of $\pm$ 5% in the rain events, whereas $\pm$ 20% is indicated for solid precipitation. Some intrinsic limitations of measuring principle, indeed, affect the measurements. One is the passing of multiple particles in the laser beam that is taken into account and corrected by a statistical procedure. Also marginal falling hydrometeors, namely those particles that enter partially into the light sheet or falling in proximity of the light sheet borders, represent a persistent problem, since such particles are considered by Parsivel as having smaller size and smaller fall velocities (Battaglia *et al.*, 2010). A recent version of the instrument (i.e. Parsivel 2) seems to have overcome this issue thanks to the addition of two photo diodes that detect margin fallers and then discard them from the count. A lack of accuracy of the Parsivel measurements is reported in case of solid precipitations and high-speed wind. Both these conditions are peculiar features of harsh and cold climatic region like Antarctica. The solid precipitation issue is deeply discussed in Löffler-Mang and Joss (2000) and in Battaglia *et al.* (2010), whereas Parsivel measurements in case of hurricane and thunderstorms are described in Friedrich *et al.* (2013a,b).

According to Löffler-Mang and Joss (2000), Parsivel provides an estimate of the size and velocity of snowflakes although, as aforementioned, in the case

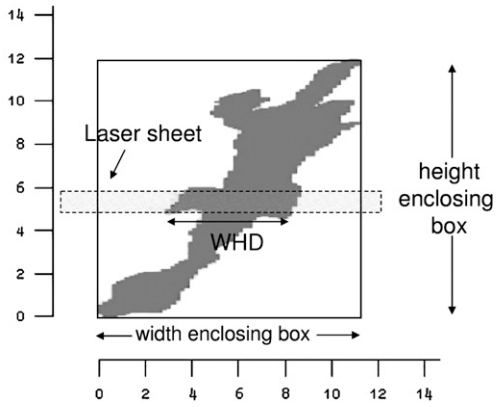

Fig. 3.8: Parsivel snowflake measuring example. WHD stands for widest horizontal dimension. Source: Battaglia *et al.* (2010).

of snow the particles are assumed to be spherical and the mean hydrometeor velocity is calculated assuming this shape, so with a fixed relationship between horizontal and vertical dimensions. Moreover, the particle size is assumed to be the maximum horizontal dimension of the snowflake seen by the instrument. The assumption of spherical shape, for ice particles, is obviously not true due to their irregularity and variety of habits, as highlighted in section 2.1.6. But as a consequence of the lack of proper empirical and theoretical relations, this assumption is currently used as a primary estimation (Löffler-Mang and Blahak, 2001). Battaglia *et al.* (2010) point out that the main shortcoming of the instrument lies in the fact that Parsivel measures only one size of the particle, which is approximately equal to the widest horizontal dimension (especially in the case of large snowflakes) and that has no microphysical meaning. Hence, instead of gauging the real size of the particle, the Parsivel returns the widest horizontal dimensions of the hydrometeor (see Figure 3.8) during its falling across the light sheet with an error less than or equal to 20% (Molthan *et al.*, 2016). This, as already

mentioned, is reflected in velocity derivation as vertical dimension is presumed from the horizontal one. Moreover, Parsivel seems to overestimate the number of small snowflakes whereas large particles would be underestimated when compared to other disdrometers (Battaglia *et al.*, 2010). Despite such considerations and the intrinsic limits of the instrument, Parsivel has been used in several studies of solid particle observations (e.g. Löffler-Mang and Joss 2000; Löffler-Mang and Blahak 2001; Yuter *et al.* 2006; Chen *et al.* 2011; Skofronick-Jackson *et al.* 2015; Molthan *et al.* 2016) with good results and in accordance with comparing instruments. In fact, as underlined by Löffler-Mang and Blahak (2001), measuring size and velocity distributions over an averaging time rather than looking at each individual particle, the Parsivel lack of accuracy, due to the influence of the irregular shapes, can be reduced.

Friedrich *et al.* (2013a) investigated the effects of wind speed and wind direction on Parsivel measurement accuracy, examining data from several disdrometers deployed during Hurricane Ike in 2008 and during some convective thunderstorms throughout the Vortex2 experiment. While they have noticed an overestimation in number concentration of medium and large particles only during the hurricane, they also found out a peculiar feature of Parsivel measurements, that appeared in high-speed wind conditions. In fact, they recognized an artifact in disdrometer observations that consists of a large number concentration of raindrops with large diameters ($>$5mm) and unrealistically low fall velocities ($<$1-2 ms^{-1}) and called it the wind effect. Indeed, in the presence of wind, the trajectories of the particles deviate from the vertical terminal fall to a slanted path (see Figure 3.9). Hence the particle motion results in the sum of air flux and the particle fall velocity and, moreover, in these conditions, the drops could be canted and distorted changing

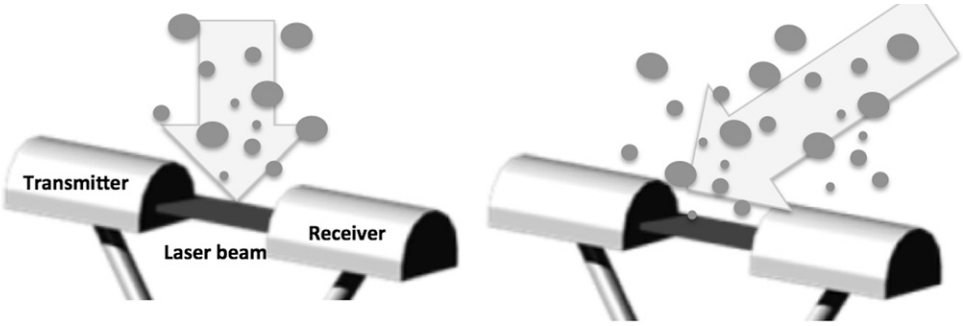

Fig. 3.9: Schemating portayal of Parsivel measurement principle in case of no wind (left hand side) and windy atmpospheric conditions (righ hand side). Gray arraw stands for particle motion. During windy conditions that is the sum of air motion and particle fall velocity. Source: Friedrich *et al.* (2013a).

particle shapes. Therefore, in such situations, the Parsivel retrieval seems to fail to identify particles in the correct way, producing this artifact. To improve the accuracy of the Parsivel observations in strong winds, some studies have suggested to orient the sampling area of the instrument perpendicular to the wind direction (e.g. Bradley and Stow 1975; Griffiths 1975) and also the manufacturer recommends deploying the instrument with its long axis perpendicular to the wind. The validity of this suggestion is also confirmed by the results in Friedrich *et al.* (2013a). In fact, the artifact noticed during high wind conditions by stationary disdrometers, was not detected by articulated instruments (Figure 3.10). The latter are disdrometers, designed by University of Florida, in which Parsivel is coupled with an anemometer. Exploiting wind direction observations, the articulating system continuously aligns the disdrometer sampling area to the air flux, in order to keep the Parsivel light sheet always perpendicular to the particle trajectories. The absence of the artifact in such instruments means that the spurious particles, observed by stationary disdrometers, are related to particle falling at

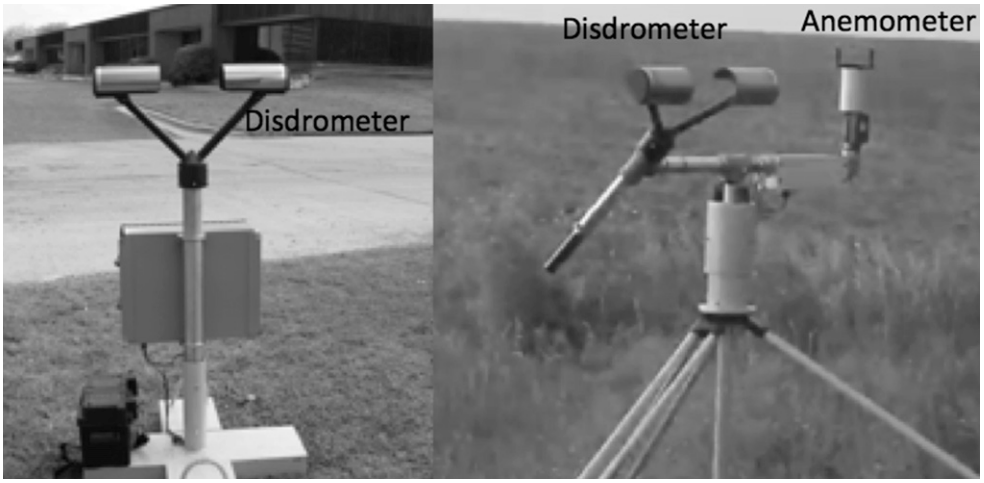

Fig. 3.10: Classical stationary Parsivel disdrometer (left hand side) and articulating disdrometer (right hand side). The latter, thanks to the coupled anemometer, is able to continuonsly orient Parsivel sampling area perpendicular respect to the wind. Source: Friedrich *et al.* (2013a).

an angle through the sampling area and this hypothesis is also proved by laboratory experiments carried out in the same research.

Parsivel Data at MZS

The disdrometer was installed in November 2016 at Mario Zuccheli station during the 32^{nd} Italian Antarctic expedition on the roof of a logistic container at 6 meters of height a.s.l. (Figure 3.11) as part of the APP-PNRA project. It has collected observations of two Austral summertime during 2016-2018 and, right now, is measuring data for the first time during the whole Antarctic year. The Parsivel was arranged with its long axis in direction north-south, hence its measurement area would be appropriate to observed particles in case of wind blowing from east or west, basing on the research illustrated above. Therefore, the strong katabatic wind affecting MZS that blows predominately

Fig. 3.11: Parsivel at Mario Zucchelli on the roof of a logistic container.

from the west or north-east, as reported in section 1.2, seems to be correctly taken into account. However, in case of barrier wind that typically comes from 180°-240° the Parsivel retrieval could be more difficult.

The disdrometer was set with a temporal resolution of 60 seconds, therefore the instrument provides a single averaged measurements each minute in order to satisfy literature suggestions regarding solid hydrometeor observation as previously described.

Parsivel is controlled and managed by a PC sheltered into the logistic container (see Figure 3.4, right hand side). The disdrometer is equipped

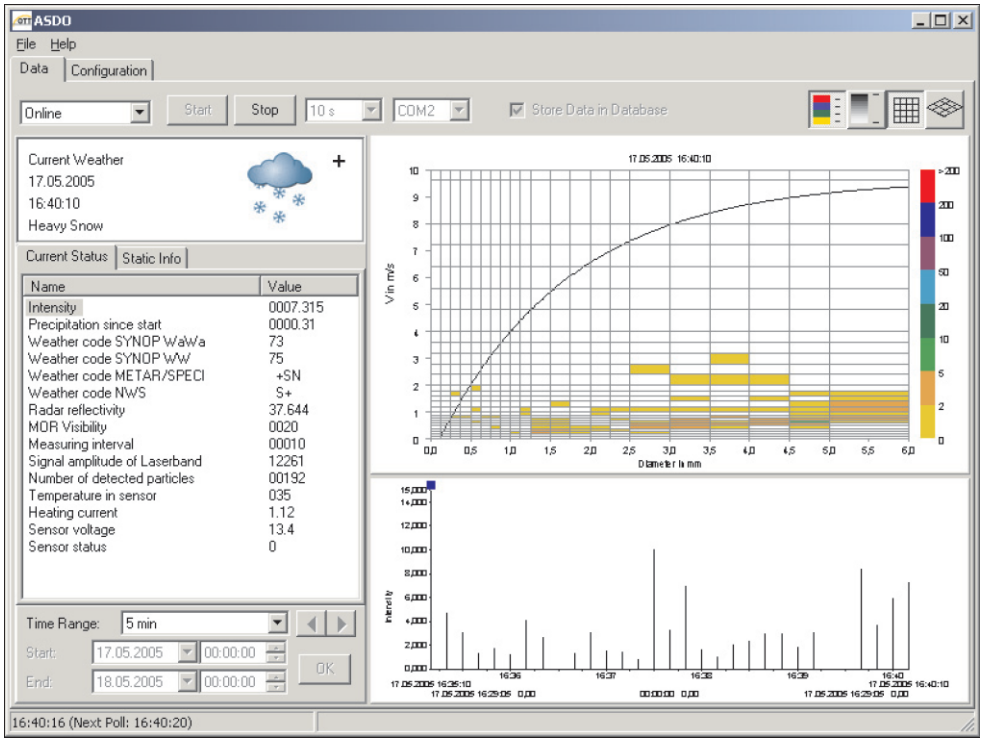

Fig. 3.12: Data tab of Parsivel application software ASDO. Source: OTT (2017a).

with an RS-485 interface and common PC's use standard RS-232 or USB interfaces, so the instrument is connected to the PC through a corresponding interface adapter.

OTT manufacturer provides an application software called ASDO to configure the Parsivel, read out and display the data, and also to manage the instrument remotely. An example of data tab screenshot of the software is presented in Figure 3.12. On the left side an icon representing the current weather is depicted along with hour, time and the particle type detected by the instrument. Just below, the current status tab displays all dynamic parameters and associated current values. On the right, the precipitation spectrograph (i.e. the size-velocity matrix) is shown. The x-axis is subdi-

vided into the 32 diameter classes and the y-axis into the 32 velocity bins. The black-curve represents the size-speed relation by Gunn and Kinzer (1949) and it is depicted as reference. As it is well known, Parsivel determines the diameter and speed of each particle passing across its light beam and the ASDO software classifies such particle in the matrix according to the measurement. The number of the detected particle is represented by the colors of the matrix. The last plot at the bottom of the screenshot represents the measurements (e.g. intensity of precipitation) in the time sequence. Moreover, ASDO stores data in the database producing the so-called Parsivel telegram every minute whose components are chosen by the user and which is written in a database text file. As an example, a telegram line of data from MZS (during a non precipitating day) is reported in order to explain what type of information and measurements are stored in.

02/02/2017;12:56:00;0.000;84.76;-9.999;9999;0;3;5836;23.9;0.06

<SPECTRUM>ZERO</SPECTRUM>

The explanation of telegram values is provided in Table 3.2. In case of precipitation detected by the instrument in place of *ZERO*, 1024 values are reported, representing the number of particles for each size-speed bin. It should be underlined that some quantities measured by Parsivel are not corrected in solid precipitation and have to be discarded. In fact, since the instrument assumes a spherical shape of the falling particles, measurements as rain intensity, rain accumulated as well as radar reflectivity are worthless in data analysis.

In this dissertation, Parsivel observations ranging from 22 November 2016 to 9 February 2017 and from 11 November 2017 to 31 January 2018 at MZS were examined, by the use of a dedicate Matlab script. Particle size distributions collected during these summer seasons were obtained and compared in

02/02/2017	Date
12:56:00	Time
0.000	Rain intensity (mm/h)
84.76	Rain amount accumulated (mm)
-9.999	Radar reflectivity (dBz)
9999	MOR visibility in the precipitation
0	Number of detected particles
3	Temperature in the sensor (°C)
5836	Signal amplitude of laser strip
23.9	Power supply voltage (V)
0.06	Heating current (A)
ZERO	32× 32 matrix of all particle detected

Table 3.2: Explanation of Parsivel telegram data.

order to infer a microphysical characterization of precipitation. In addition, even precipitation spectrographs of the two considered period were evaluated with the purpose of detecting similarities and differences. As said previously, 22 precipitation days have been identified by MRR data. PSD of these days have been used to calculate a simulated Z_e, then compared with Z_e measured by MRR in order to discriminate hydrometeors falling at MZS (methodology is introduced in section 3.2.3). Moreover, products as PSD, precipitation spectrograph as well as probability density function of maximum diameter have been employed to deeply investigate precipitation day and to find out some peculiar features, especially linked to the wind presence. Finally, the total amount of snow fall during each expedition was computed using Parsivel observations by the snowfall rate value calculated through the following

formula:

$$SR = \frac{1}{A\Delta T} \sum_{i=1}^{N} \frac{\rho_{snow}(D_i)}{\rho_{ice}} V_i n_i \tag{3.14}$$

where i represents the diameter class, n_i stands for the particles number of particles in the i^{th} class, A is the area of measurement, ΔT is the integration time in seconds, where as D and V are, respectively, the particle diameter and volume. The latter was obtained by $V = (\pi/6)D^3$. The ice density value is 0.917 g/cm^3, while the snow density, that depend on diameter by the well-know power law relationship (see section 2.1.8), was calculated using a literature relation (e.g. Brandes *et al.* 2007).

3.1.3 Ancillary measurements

In addition to measurements of the MRR and the Parsivel, also classical meteorological parameters have been evaluated. The Osservatorio Meteo Climatologico Italiano in Antartide, a PNRA project, manages and operates a network of 31 automatic weather stations positioned at Terra Nova Bay, over the Antarctic Plateau and near the French-Italian permanent station located at Dome C (Figure 3.13). Among these, the automatic station called Eneide (74°41'45"S, 164°05'32"E, 92 m a.s.l.) was chosen as representative of MZS meteorological situation, being the closest one to the research station (i.e. few hundred meters). Eneide (Figure 3.14) was installed on 7 January 1987, as the first of the network, and is equipped with a Vaisala Milos 500 sensor that provides temperature, humidity, atmospheric pressure as well as wind speed and direction (the anemometer is mounted over a 10 meters mast), and with a Kipp and Zonen pyrometer sensor giving a measure of solar radiation (Grigioni *et al.*, 2016). The station is powered by 12 batteries and 4 solar panels and stores data in a memory card, sends each minute meteorological values via satellite connection to ENEA (in Italy) and to

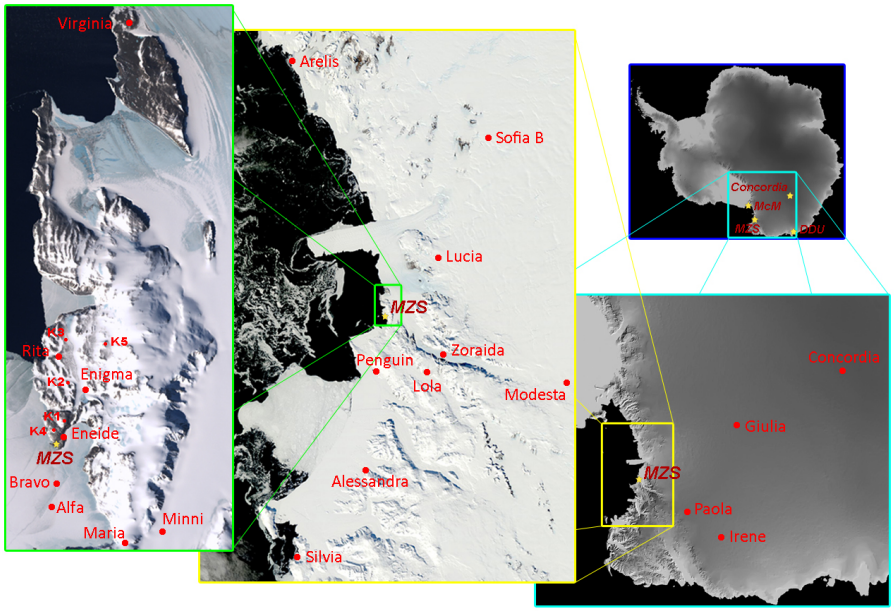

Fig. 3.13: Automatic weather stations network (red dots) of Osservatorio Meteo Climatologico Italiano in Antartide. Source: climantartide.it

Italian research stations in Antarctica.

Data are also wrapped into a text file and, for this thesis, were read trough a Matlab script. Among all the meteorological parameters, wind velocity and direction have been considered and analyzed in order to infer a possible relationship with Parsivel measurements during the 22 snow days identified.

3.2 Methods

An accurate representation of the electromagnetic behavior of precipitation particles requires modeling of realist complex geometry and a numerically efficient technique to calculate averaged scattering properties over multiple random target orientations (Fenni *et al.*, 2018). Moreover, detailed electro-

Fig. 3.14: The Eneide automatic weather station. Source: climantartide.it

magnetic models for ice crystals are necessary for calculating radar reflecivity as the latter depends on backscattering cross section linked to size, mass and distribution of mass within the crystal (Botta *et al.*, 2013). The methods to model snow scattering properties at microwave frequencies can be divided into structurally explicit and implicit techniques. The former determine scattering and backscattering cross section assuming full knowledge of a given snow particle structures and such calculation are computationally expensive and time consuming. The implicit techniques model equivalent particles with variable mass, bulk density and aspect ratio according to an effective-medium approximation. It is highly desirable to find a reasonable agreement between model ice crystal cross sections using both methods (Honeyager *et al.*, 2016).

Two scattering computation methods were investigated in this thesis in

order to explore the response of ice crystals to electromagnetic radiation at 24 GHz (K-band, the MRR operational frequency) and to obtain scattering properties of ice/snow particles: an explicit technique, the Discrete Dipole Approximation (DDA) and an implicit one, namely the T-matrix method (TMM). T-matrix is a powerful exact technique for computing light scattering by non-spherical particles based on numerical solutions of Maxwell's equations (Mishchenko and Travis, 1998). While in T-Matrix ice/snow particles are approximated as soft-spheroid, in DDA the complex geometry of each particle is electromagnetically represented by a distribution of polarizable points, yielding to an accurate scattering properties of particles (Kuo *et al.*, 2016). Hence DDA is able to take into account the complexity of snow, but large computation time is required.

3.2.1 Discrete Dipole Approximation

Overview

The discrete dipole approximation is a numerical technique for the calculation of the scattering and absorption properties of arbitrary shaped particles (Liou and Yang, 2016). Exact solutions to Maxwell's equations are known only for special geometries such as spheres, spheroids or infinite cylinders, so approximated methods are typically required and DDA belongs to this category. In DeVoe (1964) this method was first proposed for studying the optical properties of various particles, especially molecular aggregates. Then, Purcell and Pennypacker (1973) introduced DDA to study interstellar dust grains. The common use for scattering calculations of DDA was finally presented by Draine (1988) and Draine and Flatau (1994).

In DDA the target objects are approximated as arrays of polarizable

dipole elements (dipoles) that are on the cubic lattices. These polarizable points acquire dipole moments via their response to the local electric field and the electric field of the surrounding points (Nowell *et al.*, 2013). To approximate a homogeneous medium, the spacing d of the dipoles must be small enough compared to the incoming electromagnetic wavelength, specifically $|m|d << \lambda$, where λ is the wavelength in the external medium (e.g., vacuum or air) and m is the complex relative index of refraction of the material comprising the particle (Petty and Huang, 2010).

From a mathematical perspective, according to Draine and Flatau (1994), the electromagnetic scattering problem has to be solved, as stated, for a target that is represented by an array of N dipoles. Each j^{th} dipole is located at position $\mathbf{r}_j$ and has a polarization as follow:

$$\mathbf{P}_j = \alpha_j \mathbf{E}_j \tag{3.15}$$

where α_j is the polarizability and $\mathbf{E}_j$ is the electric field at $\mathbf{r}_j$. $\mathbf{E}_j$ is the result of two contributes, namely the incident electromagnetic wave $\mathbf{E}_{inc,j}$ and the contribution of the other dipoles as:

$$\mathbf{E}_j = \mathbf{E}_{inc,j} - \sum_{k \neq j} \mathbf{A}_{jk} \mathbf{P}_k \tag{3.16}$$

here $\mathbf{A}_{jk}\mathbf{P}_k$ stands for the electric field at $\mathbf{r}_j$ due to the dipole $\mathbf{P}_k$ at $\mathbf{r}_k$. The matrix $\mathbf{A}_{jk}$ is a 3×3 linear operator that maps the contribution of k^{th} region polarization vector to the local electric field at region j (Ori, 2016). If $\mathbf{A}_{jj}$ is defined as $\mathbf{A}_{jj} \equiv \alpha^{-1}$, then the scattering problem is reduced to finding the polarization $\mathbf{P}_j$ satisfying a system of $3N$ linear equations:

$$\sum_{k=1}^{N} \mathbf{A}_{jk} \mathbf{P}_k = \mathbf{E}_{inc,j} \tag{3.17}$$

This complex linear system can be solved by direct matrix inversion or via iterative methods. The most complete solution is obtained by matrix inversion

but huge memory is needed, whereas iterative methods require less memory but yield a solution for only one incident wave direction and polarization at a time (Petty and Huang, 2010).

Once that has been solved for unknown polarizations $\mathbf{P}_j$, then the scattered field can be compute in any position as well as the extinction and absorption cross sections:

$$C_{ext} = \frac{4\pi k}{|\mathbf{E}_0|^2} \sum_{j=1}^{N} Im(\mathbf{E}^*_{inc,j} \cdot \mathbf{P}_j) \tag{3.18}$$

$$C_{abs} = \frac{4\pi k}{|\mathbf{E}_0|^2} \sum_{j=1}^{N} \left\{ Im[\mathbf{P}_j \cdot (\alpha^{-1})^* \mathbf{P}^*_j] - \frac{2}{3} k^3 |\mathbf{P}_j|^2 \right\} \tag{3.19}$$

where k represents the wavenumber. Then the scattering cross section is calculated as:

$$C_{sca} = C_{ext} - C_{abs} \tag{3.20}$$

The processing time and memory requirements in order to solve and run the DDA method are very expensive, and computational costs increase dramatically with particle size parameters, particle finer resolution, larger particles and higher frequencies. Moreover, according to Honeyager *et al.* (2016), assuming fully random particle orientation, the DDA calculations must be repeated over many possible orientations of the particle relative to the incident light beam in order to determine the scattering properties, and also a large number of representative habits of the hydrometeors must to be considered with the purpose of portraying the wide variability of natural particles. Such tasks, evidently, require additional computational resources. These are the reasons why a pre-completed, comprehensive and innovative DDA database was used in this thesis, containing scattering properties for realistically shaped snow particle models.

The NASA DDA Database

Several recent DDA databases have been developed in order to perform studies and computations based on accurate scattering models (e.g.Liu 2008; Botta *et al.* 2011; Tyynelä *et al.* 2011; Nowell *et al.* 2013; Tyynelä and Chandrasekar 2014; Ori *et al.* 2014; Leinonen and Szyrmer 2015; Lu *et al.* 2016), and also to make available valuable tools to the scientific community. Among these, the extensive database of scattering properties of simulated pristine crystal and aggregate particles presented in Kuo *et al.* (2016) was chosen in this thesis.

Four are the main reasons for this selection: first, scattering properties in the Kuo's database have been calculate also for the K-band frequency (the same as the Micro Rain Radar) as opposed to the majority of the others (e.g. Botta *et al.* 2011; Tyynelä *et al.* 2011; Tyynelä and Chandrasekar 2014; Ori *et al.* 2014; Leinonen and Szyrmer 2015); second, the clear distinction between pristine and aggregate ice particles; third, the huge number of realistic synthetic solid hydrometeors and their corresponding single-scattering properties, namely more than 1000 for pristine and nearly 7000 for aggregate, that make this database by far the most complete; fourth, the further subdivision, beyond the main differentiation, of the particles into different hydrometeor habits for each main class.

As previously said, the NASA database provides the single-scattering parameters of individual and aggregate particles (see also section 2.1.6) that are derived using the DDSCAT code. The latter is a Fortran code for calculating scattering and absorption of light by irregular particles and periodic arrangement of irregular particles based on DDA method and developed by Draine and Flatau (2008). In addition to those properties, also geometric features of solid hydrometeros are given into the database that is freely and

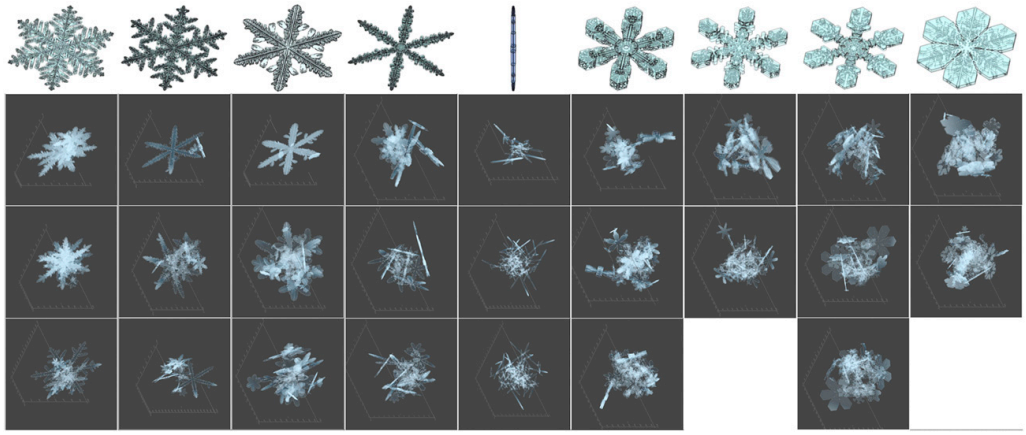

Fig. 3.15: Nine pristine habits of NASA database (first row). Beneath, snaphots of aggregation mechanism for each habit. Source: Kuo *et al.* (2016).

currently available online[1].

Typically, in order to generate synthetic ice crystals, two different methods are used: physical or empirical. The former tries to mimic the natural growth by diffusion of ice crystals in a cloud, whereas, in the latter, the physical properties are taken from in-situ observations for each habits. In the NASA database a physical method was used, since the simulation of individual pristine ice crystals is based on Gravner and Griffeath (2009), where a 3D model for snow-crystal growth, called "snowfake", is presented. Snowfake is a computational algorithm that describes the diffusion of vapor and the subsequent freezing in hydrometeor formation and, moreover, varying the initial crystal seed as well as the environmental conditions (e.g. saturation level) and other parameters, a large variety of crystal habits, that closely resemble crystals found in nature, is achieved and explained in the paper.

Exploiting this work, the NASA database contains nine different crystal pristine habits that are depicted in the upper row of Figure 3.15. The lat-

[1]https://storms.pps.eosdis.nasa.gov/storm/OpenSSP.jsp

ter includes the fern dendrite, classic dendrite, dendrite with facets, simple star dendrite, needle, three dendrite with broadening arms and a sandwich plate. Kuo *et al.* (2016) specify that these pristine shapes are representative of the habits usually observed in growth regime at temperatures higher than -20°C. Moreover, it should be underlined that other common types of ice crystals (e.g. rosettes, columns) are not included in this database, and that, in particle synthetic growth, the riming processes are not considered, so hydrometeors are limited to unrimed crystals.

Aggregate particles included in the database are composed only of pristine crystals coming from the same particle shape, hence only one of the nine habits is used to create an aggregate. This means that, for example, a fern dendrite aggregate is made up of a pristine fern dendrite main particle, which acts as "collector", and other smaller fern dendrite particles. Therefore such collector catches randomly, with a probability that decreases exponentially as a function of particle size, other hydrometeors of different sizes but with the same basic geometric structure. The process, that is repeated iteratively until the aggregate reaches a liquid equivalent diameter of 3.1 mm or a maximum fixed numbers of components, is depicted in lower rows of Figure 3.15. Although the self-collection method is heuristic, the properties of the resulting snow particles are consistent with observations (Kuo *et al.*, 2016), showing also different relationships of mass versus maximum diameter for each aggregate type. The same is also true for pristine particles. The distribution of aggregates is assumed to be consistent with a median canting angle[2] of 28° and, although this values is slightly higher than those reported

[2]The axes of symmetry of the hydrometeors are tilted by the effect of falling and the resulting angle between the minor axis and the vertical is known as the canting angle (Dalgleish, 1989).

in the literature, it is still in the range of canting angle observations.

Following this procedure for synthetic aggregate formation and adding pristine particles, the database contains more than 8000 synthetic hydrometeors ranging from a minimum size of 260 μm to a maximum size of 14.26 mm (both expressed as maximum dimension of the solid particles). In addition, it should be considered that the limitation of large particle size is not due to aggregation method but rather to the substantial computational memory needed to calculate scattering properties.

Thirteen microwave frequencies, from 10 to 190 GHz, are investigated in the database. The single-scattering properties are produced for the common bands used by ground based or satellite based instruments for remote sensing research including, for example, 89 and 165.5 GHz, namely the frequencies of GPM Microwave Imager or 13.6 and 35.5 GHz for dual-frequency precipitation radar and also the K-band that is the operational band of the Micro Rain Radar.

In the database, for each particle, dimension and single scattering parameters are provided (see Table 3.3, with the short description given by the authors). For the calculations, ice particles were assumed to fall with random orientation so that the hydrometeor response at each frequency is averaged over 900 different particle orientations with the purpose to produce representative parameters.

For the aims of this thesis, 18 NASA database files were downloaded from the aforementioned website, containing responses of hydrometeors to K-band electromagnetic beam. Nine files are representative of the nine pristine habits and the same amount for aggregate particles. Then, with a suitable Matlab code, these TSV[3] files were processed and merged together in order to obtain

[3]TSV stands for Tab Separated Values, a simple text format files for storing data in a

Variable	Explanation
D_{max}	maximum dimension/diameter
$Rho_{D_{max}}$	snow density based on D_{max}, ice mass of the particle divided by the volume of a sphere with D_{max} as its diameter
Q_{bk}	backscattering efficiency
Q_{ext}	extinction efficiency
Q_{sca}	scattering efficiency
Q_{abs}	absorption efficiency
g	asymmetry factor
Prj_{Area}	orientation-averaged projection area of the particle
Sfc_{Area}	surface area of the particle
r_{eq-vol}	radius of a sphere having the same volume as the ice mass of the particle
r_{eq-prj}	radius of a sphere having the same projection area as the orientation-averaged projection area of the particle
r_{eq-sfc}	radius of a sphere having the same surface area as that of the particle
L_{lx}	length of the shortest axis of a circumscribing ellipsoid of the particle
L_{ly}	length of the intermediate axis of a circumscribing ellipsoid of the particle
L_{lz}	length of the longest axis of a circumscribing ellipsoid of the particle
Rho_{elps}	snow density based on the circumscribing ellipsoid, ice mass of the particle divided by the volume of the circumscribing ellipsoid

Table 3.3: NASA database variables provided for each particle and their explanation.

two valuable databases: one that represents the single crystals variability of solid precipitation, the other the aggregate variability. Both cover a wide particle dimensional range.

To obtain a single backscattering cross section value for each of 32 Parsivel size bins the procedure was carried out as follows: first, backscattering cross section was calculated for each particle of pristine and aggregate databases; second, the databases were split into the 32 size bins based on D_{max} (i.e. the maximum dimension) of each particle since this dimension has been thought to represent in the best way the "true" dimensions of hydrometeors at MZS, being Antarctic falling particles relatively small and despite the uncertainties expressed in section 3.1.2 about the size observed by Parsivel; third, the values contained in the bins were averaged (or, randomly, one of those values was selected) achieving 32 backscattering cross section values, that is one for each Parsivel size bins.

Actually, obtaining backscattering cross section values from the NASA database was quite challenging. In fact this variable of interest is not present in Table 3.3. Therefore, the cross section was derived from the backscattering efficiency. As pointed out in section 2.2.5 and equation 2.45, Q_b is related to σ_b and the calculation seems to be rather straightforward. But understanding what kind of particle dimension is represented by the term a in equation 2.45 was quite puzzling. In the literature, different ice particle dimensions are used to attain backscattering cross section on the basis of the efficiency. Nowell *et al.* (2013), for instance, suggest to employ the radius of an equal mass of the solid ice sphere, whereas the whole denominator of equation 2.45 means the projected area of a volume-equivalent sphere of the scattered particles in Hong *et al.* (2009). Moreover, there is no mention of cross section

tabular structure.

calculation in Kuo *et al.* (2016) or in other papers using this database (e.g. Leinonen *et al.* 2018). Therefore, in order to untangle this problem, several backscattering cross sections were calculated using the different dimension variables of the database (i.e. $D_{max}, Prj_{Area}, Sfc_{Area}, r_{eq-vol}, r_{eq-prj}, r_{eq-sfc}$). Then the results were compared with backscattering cross section values supplied by another DDA database, the well-established research work of Leinonen and Szyrmer (2015), with the aim to select the right dimension variable to calculate σ_b by means of Kuo's database. The comparisons will be showed in chapter 4.

Moreover, with the purpose of comparing the DDA scattering outputs with the σ_b coming from the T-Matrix method, the density-size relationship has been achieved from the NASA database, as well as the aspect ratio (i.e. the ratio between vertical and horizontal dimensions) with respect to the size. These two relations will be used as inputs of T-Matrix code in the computation of backscattering cross sections.

3.2.2 T-Matrix

Overview

In many remote sensing applications, solid hydrometeors are approximated as spherical or spheroidal shapes consisting of a mixture of air and ice. This simplified model is commonly referred to as soft or fluffy sphere and have reached a large popularity due to the associated scattering numerical method such as the T-Matrix (Mishchenko *et al.*, 1996), that allows to compute an analytic solution within short computational time (Ori *et al.*, 2014). Even though this model is considered to be a source of error in dealing with scattering problems of solid particles, especially in comparison with more detailed

models such as the DDA method (e.g. Kulie *et al.* 2010; Botta *et al.* 2011; Tyynelä *et al.* 2011), it is widely used in the radar-meteorological scientific community both for its rapidity, as mentioned above, and because spheroidal model is a quite good approximation for raindrops. Mainly, the soft sphere approach fails since it requires approximating even complex ice crystals as having uniform density inside the particle, while in nature, as already discussed in section 2.1.8, the inner parts of a large snowflakes are denser than the outer ones.

In the scattering problems the incident and scattered electric fields can be expanded in terms of suitable vector wave functions. According to Liou and Yang (2016), the expansion coefficients associated with the scattered wave can be related to their counterparts for the incident wave through a transmitting matrix, known as T-matrix, containing all the single scattering characteristics of the corresponding scattering particle. A methodology to compute the T-matrix was created by Waterman (1971), the so-called extended boundary condition method (EBCM), while Mishchenko and Travis (1998) have implemented EBCM by a computational code to efficiently calculate the single scattering properties of a number of axially symmetric non-spherical homogeneous particles such as cylinders, spheroids and Chebyshev particles.

Typically the T-matrix method starts with expanding incident and scattered fields in vector spherical harmonics as follows:

$$\mathbf{E}^i(\mathbf{R}) = \sum_{n=1}^{\infty} \sum_{m=-n}^{\infty} [a_{mn} Rg\mathbf{M}_{mn}(k\mathbf{R}) + b_{mn} Rg\mathbf{N}_{mn}(k\mathbf{R})] \tag{3.21}$$

$$\mathbf{E}^s(\mathbf{R}) = \sum_{n=1}^{\infty} \sum_{m=-n}^{\infty} [p_{mn} \mathbf{M}_{mn}(k\mathbf{R}) + q_{mn} \mathbf{N}_{mn}(k\mathbf{R})] \tag{3.22}$$

here $Rg\mathbf{M}_{mn}$, $Rg\mathbf{N}_{mn}$, $\mathbf{M}_{mn}$ and $\mathbf{N}_{mn}$ are vector spherical wave functions, whereas a_{mn}, b_{mn} and p_{mn}, q_{mn} are the incident coefficients and the scattered

coefficients respectively. Thanks to the linearity of Maxwell's equations and boundary conditions, the relationships between the incident and scattered parameters is linear and can be written by the transmitting matrix in this way:

$$p_{mn} = \sum_{n'=1}^{\infty} \sum_{m'=-n'}^{n'} [T^{11}_{mnm'n'} a_{m'n'} + T^{12}_{mnm'n'} b_{m'n'}] \tag{3.23}$$

$$q_{mn} = \sum_{n'=1}^{\infty} \sum_{m'=-n'}^{n'} [T^{21}_{mnm'n'} a_{m'n'} + T^{22}_{mnm'n'} b_{m'n'}] \tag{3.24}$$

Using matrix form it would be written as:

$$\begin{bmatrix} \mathbf{p} \\ \mathbf{q} \end{bmatrix} = \mathbf{T} \begin{bmatrix} \mathbf{a} \\ \mathbf{b} \end{bmatrix} = \begin{bmatrix} \mathbf{T}^{11} & \mathbf{T}^{12} \\ \mathbf{T}^{21} & \mathbf{T}^{22} \end{bmatrix} \begin{bmatrix} \mathbf{a} \\ \mathbf{b} \end{bmatrix} \tag{3.25}$$

T-matrix contains the complete optical properties of the scattering particle so, knowing the T-matrix, is quite simple to calculate the scattering properties for any orientation and any scattering angle of the particle. Mishchenko (1990) provided a computationally and efficient approach to calculating single scattering properties averaged over random orientations, useful when dealing with hydrometeor scattering. Lastly, the scattering cross section can be derived from T-matrix elements as:

$$C_{sca} = \frac{2\pi}{k^2} \sum_{l=1}^{l_{max}} \sum_{l'=1}^{l_{max}} (|T^{11}_{ll'}|^2 + |T^{12}_{ll'}|^2 + |T^{21}_{ll'}|^2 + |T^{22}_{ll'}|^2) \tag{3.26}$$

where the previous double (mn) indices are combined into the single l index defined as $n(n+1)+m$.

T-Matrix code

In this thesis, numerical simulations were carried out using the T-Matrix model for spheroidal particles. The outputs of these simulations have been compared with those of the DDA method, in order to point out differences in

atmospheric ice particle scattering models between a soft-spheroid approximation and a more detailed approach in dealing with complex ice particle shapes.

The CANTMAT 1.2 Fortran code developed at Colorado State University was exploited for these calculations. This code is commonly in use in the radar-meteorology research group of the Institute of Atmospheric Sciences and Climate (ISAC) at the National Research Council of Italy (CNR), where this thesis has been developed. The CANTMAT code allows to calculate the Mueller matrix and Stokes vector of several solid and liquid hydrometeor types, such as cloud droplet, rain drop, aggregate and graupel for any electromagnetic frequency. The aggregate option was chosen for these simulations, carried out at K-band frequency, with the view to compare the results with DDA aggregate database. With the aid of a suitable Matlab code, from the Mueller matrix and Stokes vector, backscattering cross sections with respect to particle diameters were obtained.

In addition, CANTMAT requires some user inputs to work properly. In fact, the dimension of the particles for which the scattering parameters will be calculated as well as the size-density and the axis ratio relations and also the standard deviation of canting angle must be written into the Fortran code. Therefore the central value of each Parsivel size bin was used as input diameter, whereas the two relations were derived from the DDA database (the methodology followed is presented in section 3.2.3), lastly canting angle variability value was taken from Kuo *et al.* (2016).

3.2.3 Methodology

DDA - T-Matrix harmonization

With the purpose of properly comparing the results of the two scattering methods, few adjustments had to be considered and were adopted. As mentioned above, the T-matrix code requires relationships involving the dimension of the particle coupled with density and the axis ratio. These two relations follow different patterns. Density-size relation agrees with a power-law form (see also section 2.1.8), whereas a linear form links size and axis ratio (Nowell *et al.*, 2013). Both of them have been derived from DDA database as described below.

As can be seen perusing Table 3.3, an ice solid particle is described with different size parameters but only one must be considered in density and axis ratio relations. The choice was based on the following way of thinking. The T-Matrix, and consequently the CANTMAT code, deal with spheroidal particles and require an equivolume diameter. So, while the choice to use Parsivel size bins, as diameter for scattering calculations, could be correct since Parsivel considers hydrometeors as spheroidal shapes, none of the size parameters in Table 3.3 could be used for the calculation of size relations. This is the reason why a new radius has been computed. Calculating the mass of each DDA particle (gathered through D_{max} and $Rho_{D_{max}}$) and dividing it by rho_{elps}, the volume of an ellipsoid circumscribing the particle has been obtained and approximately can be considered as the volume of the spheroid circumscribing the particle. Then, from this volume, the radius of a sphere has been derived, representing the radius of a sphere equivolume to the ellipsoid/spheroid. Hence, the equivolume diameter was calculated for each particle of the DDA database. Later, the results were plotted versus

the density (rho_{elps}) and versus the aspect ratio (computed as the ratio between shortest and longest axis of circumscribing ellipsoid). Finally, using the Matlab fitting tool, the power law relation between equivolume diameter and density and the linear relation between equivolume diameter and axis ratio were obtained. Both have been used as inputs, into the CANTAMAT code.

Hydrometeors characterization

Through the use of simultaneous measurements of snowfall from the Micro Rain Radar and the Parsivel disdrometer, a method to distinguish among different hydrometeors can be developed and evaluated by comparing simulated and observed values. In particluar, it is possible to validate DDA or T-matrix backscattering cross sections by comparing Ze (i.e. equivalent radar reflectivity) computed using disdrometer measured PSD and scattering calculations, with the actual MRR measurements. The equivalent reflectivity factor can be calculated by equation 3.27. This is expressed as a summation over particles binned within specific size ranges and it is simply the result of Parsivel measurements (N_i is the number of particles within the size bin and ΔD_i is the bin width) multiplied by σ_b, namely the backscattering cross section of the particles. The other terms λ and $|K|^2$ are, respectively, the radar wavelength and a value related to the dielectric constant of liquid water and conventionally equal to 0.92.

$$Ze = \frac{\lambda^4}{\pi^5 |K|^2} \sum_i N_i \Delta D_i \sigma_{b,i} \tag{3.27}$$

More to the point, the MRR equivalent reflectivities measured at the first exploitable range gate (i.e. 300 meter a.g.l.) were used in these comparisons, together with the calculations of four Ze from as many simulations. These four

simulations represent each backscattering calculation method used: DDA aggregate database, DDA pristine database, T-Matrix initialized with DDA size relations and T-Matrix initialized with literature size relations.

Two error score indexes were used in this work for the evaluation of the measured and simulated Z_e comparisons. Specifically, the Pearson correlation coefficient and the root mean square error were calculated for each of the 22 precipitation days identified during the period considered at MZS. Through the analysis of the results of such statistical tools, the falling hydrometeor type has been evaluated and the precipitation days were classified based on ice particle properties.

Chapter 4

Results

4.1 NASA-Leinonen database comparison

A comparison between two different DDA databases has been carried out, as preparatory work, in order to obtain the proper backscattering cross sections from the NASA database. Indeed, in the latter, as discussed in section 3.2.1, the backscattering properties are provided in the form of the efficiency, and the process to derive the cross section was not straightforward. Hence, another DDA database was chosen with the purpose of comparing backscattering cross sections and of selecting the right dimension in the particle representation. Giving the absence of particle properties at K-band frequency in the Leinonen database, three other frequencies (Ku, Ka and W bands) were chosen in this evaluation. The backscattering cross section values of the two databases are reported in the following plots and depicted as circles (Leinonen database) and dots (NASA database). In Figure 4.1, the Leinonen values are compared with the NASA backscattering entries. The latter were calculated considering the maximum diameter of the particle as the right representation of the size (see section 2.2.5), namely it was used

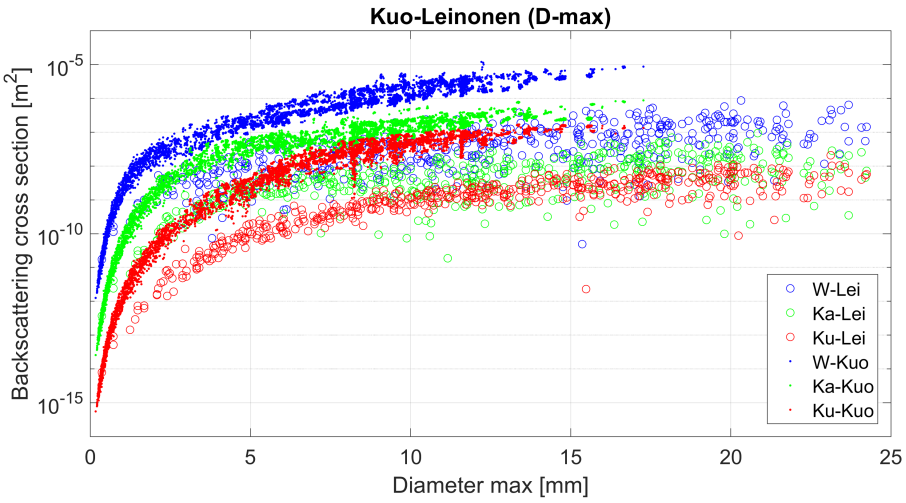

Fig. 4.1: Comparison between backscattering cross section values of NASA (dots), calculated by maximum diameter, and Leinonen (circles) databases. Colors represent Ku (red), Ka (green) and W (blue) bands.

as the denominator term of equation 2.45. Also the radius of a sphere having the same projection area as the orientation-averaged projection area of the particle was used, as first guess, to calculate the NASA cross sections. The results are reported in Figure 4.2. Both graphs show a large difference in all the electromagnetic bands between the two DDA databases, with a clear overestimate of the NASA database with respect to the Leinonen one. Therefore, neither the maximum diameter nor the projection radius were chosen as the dimension to be used. Instead, calculating the cross sections through the equivalent radius, defined as the radius of a sphere having the same volume as the ice mass of the particle, the two databases resulted in a good agreement. In fact, analyzing Figure 4.3, it must be noted that the two DDA values, at the investigated frequencies, are more or less completely overlapped. Hence, considering the Leinonen database as a reference, the equivalent radius was used as the description of the particle size in order to

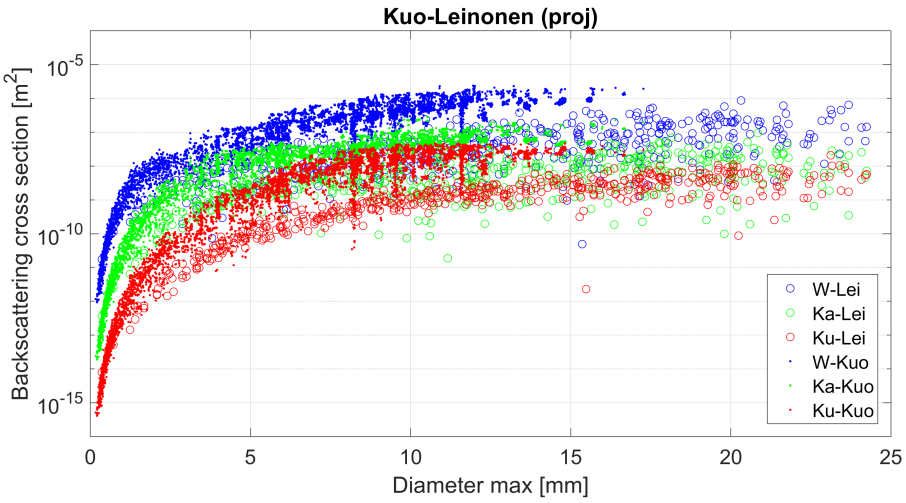

Fig. 4.2: Comparison between the backscattering cross section values of the NASA (dots) calculated by projection radius and the Leinonen (circles) databases. Colors represent Ku (red), Ka (green) and W (blue) bands.

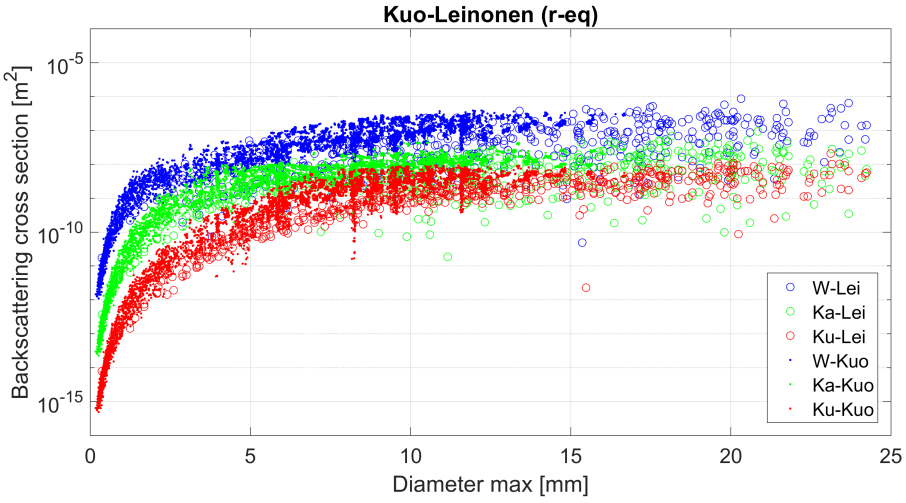

Fig. 4.3: Comparison between the backscattering cross section values of the NASA (dots) calculated by equivalent radius and the Leinonen (circles) databases. Colors represent Ku (red), Ka (green) and W (blue) bands.

obtain the backscattering cross section from the backscattering efficiency in this dissertation.

4.2 The NASA database

Following the way of thinking and the procedure explained in the previous section, the backscattering cross sections were computed even at K-band. As reported before, the NASA database has been divided into a pristine and an aggregate databases. Each one contains nine ice particle habits covering the majority of the natural snow variability. The calculated values are depicted in Figure 4.4 for the pristine ice particles, and in Figure 4.5 for the aggregates. It should be noted how the different shapes affect the electromagnetic response of the particles, and even how the dimension of the hydrometeor (here represented by the maximum diameter) plays an important role in the scattering. The pristine ice crystals seem to follow a similar response pattern at the lower sizes, while the difference becomes pronounced at larger dimensions, especially for the needle crystals that show a backscattering cross section nearly two orders of magnitude smaller compared to the other shapes. It must be stressed that the graph is presented in a logarithmic scale, therefore little differences in the plot result in a large gap. The aggregates follow a similar trend as that of pristine crystals, with an evident increase of cross section values between smaller dimensions and 4 mm. The needles again show a peculiar pattern. In fact, at the same maximum dimension, they can attain several backscattering values. This could be due to the particular growth mechanism of needles computed using the snowfake algorithm of Gravner and Griffeath (2009).

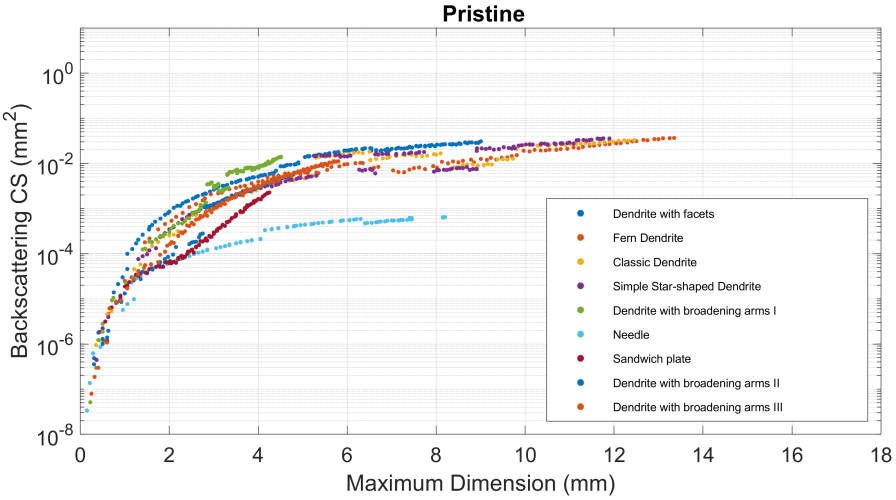

Fig. 4.4: NASA database backscattering cross sections for the ice pristine particles at K-band. Colors represent different hydrometeor habits.

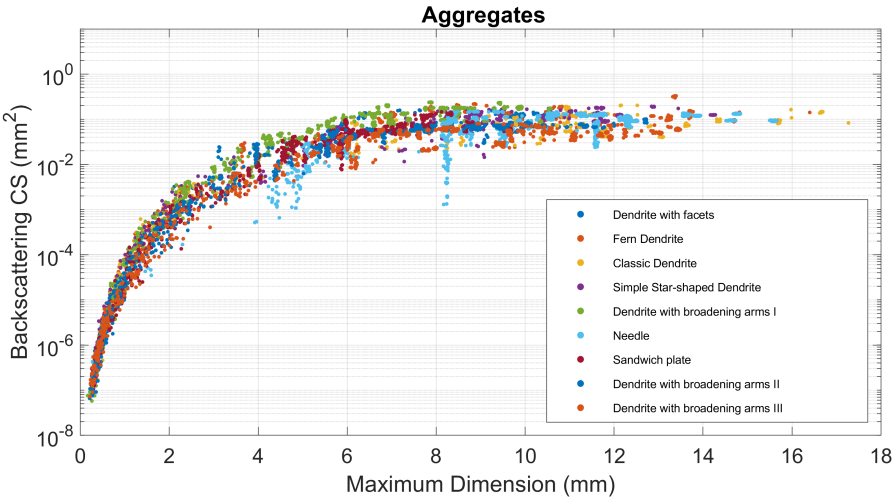

Fig. 4.5: NASA database backscattering cross sections for ice aggregate particles at K-band. Colors represent different hydrometeor habits.

4.3 DDA - T-Matrix comparison

The evaluation of the response of hydrometeors to the electromagnetic radiation is one of the aims of this thesis. For this purpose two of the most utilized scattering methods were compared. As explained in section 3.2.3, some size relations were retrieved from the NASA database in order to be used as inputs into the T-Matrix code. Utilizing the DDA aggregate database (because the CANTMAT code processes hydrometeors as aggregate-like particles) the density-diameter relation was obtained and is shown in Figure 4.6. The diameter of a sphere equivolume to the ellipsoid circumscribing the ice particles was used as the size representation (see also section 3.2.3). The achieved relationship, where a and b stand, respectively, for the coefficient and the exponent of the power law form of the equation, is consistent with the literature relations (e.g. Heymsfield *et al.* 2004). In this analysis the dif-

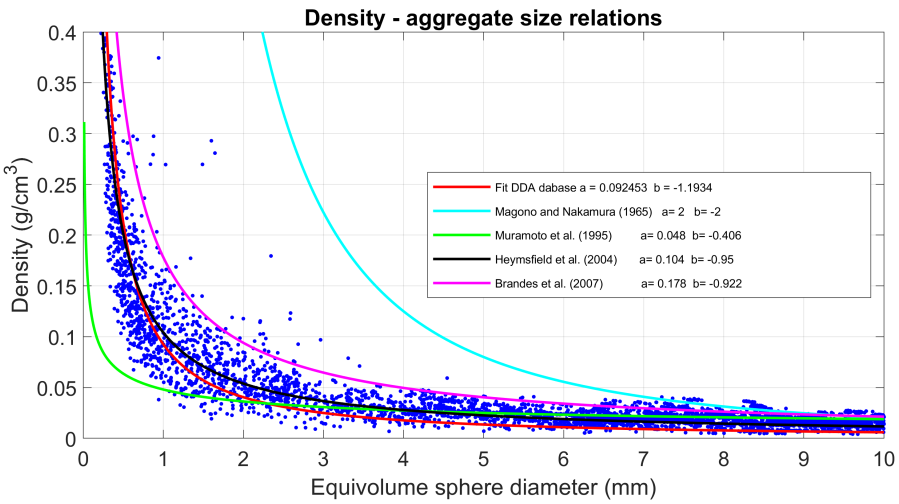

Fig. 4.6: Density-dimension power law relation of the DDA NASA database. Blue dots represent database of aggregate particles. Red line stands for fitting line. The other lines are relationships from the literature for reference.

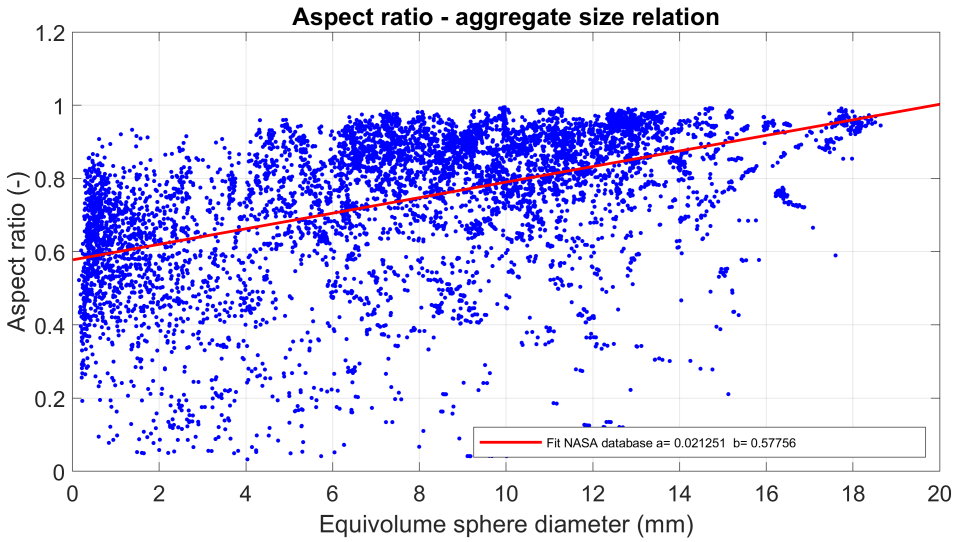

Fig. 4.7: Aspect ratio-dimension linear relation of the DDA NASA database. Blue dots represent the database of aggregate particles. Red line is a fitting line.

ferent habits were not considered and the particles were processed as general aggregate hydrometeors. This is the reason why they are depicted with a unique color in the graphs. That is to comply with the CANTMAT code, in which no habit distinction is made. A linear form, instead, links together the aspect ratio of the particles and their dimensions. Using a linear fit, the two coefficients were calculated (Figure 4.7) resulting in reasonable agreement with the literature relationships (e.g. Nowell *et al.* 2013).

By these two relations the CANTMAT code was initialized. The outcomes of T-Matrix computations were compared with the DDA backscattering cross sections. The results are shown in Figure 4.8. Here, the dots depict the cross section values of particle as calculated from the NASA database. The different hydrometeor shapes were made explicit through the colors with the aim of highlighting if some habits showed similar patterns to the T-Matrix

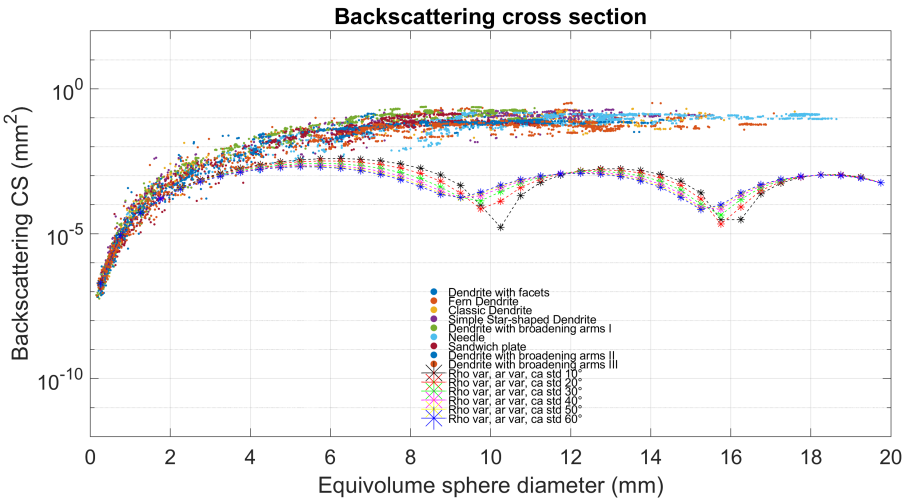

Fig. 4.8: Backscattering cross sections at 24 GHz. Dots represent the NASA DDA database values. Lines with stars stand for the CANTMAT T-Matrix calculations in which the density and aspect ratio depend on the particle diameter.

simulations. The latter are drawn as lines and stars and the different colors represent the different values of the canting angle standard deviation. The two methods seem to be in good agreement at the smaller sizes, where the particles fall within the Rayleigh approximation. Then there is a large discrepancy between the methods and the DDA exhibits higher values than the T-Matrix calculations. Moreover, the latter show the classical Mie resonance behavior, not found in the DDA results. That is probably because CANTMAT considers particles as having a symmetrical structures, whereas, in the NASA database, the aggregates are represented with more details, losing the geometrical symmetry.

To assess the T-Matrix variability due to the different size relation settings, several simulations were performed. In particular, some calculations were carried out with the canting angle standard deviation set at 10 degrees

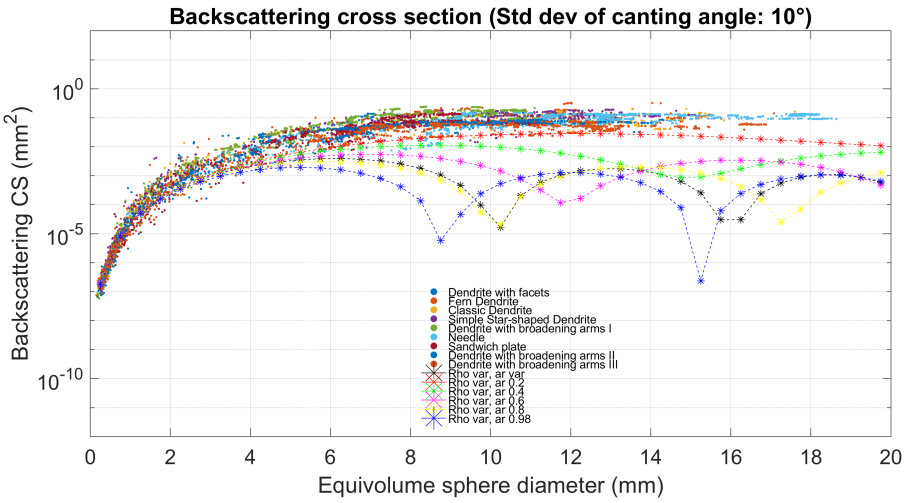

Fig. 4.9: Backscattering cross sections at 24 GHz. Dots represent the NASA DDA database values. Lines with stars stand for the CANTMAT T-Matrix calculations: black line represents the computation where the size relations were used and it is depicted as reference, the other lines stand for the simulations in which the particle density depends on the particle diameter, whereas the aspect ratio assumes fixed values.

and with fixed values of the axis ratio, while the density was linked to the hydrometeor size by the aforementioned relation. The results are shown in Figure 4.9. It can be seen how the T-Matrix resonance is strictly related to the axis ratio values. In fact, with the lowest value (ar=0.2) the CANTMAT simulation (red line with stars) exhibits a pattern similar to the DDA, without the resonance effects, that instead becomes clear with a quasi-spherical shape (ar=0.98, blue line). However, such a low value of the axis ratio is rather unrealistic for the hydrometeors.

As mentioned on several occasions in this thesis, the scattering properties depend deeply on density. In order to explore the T-Matrix electromagnetic responses with respect to this quantity, several density values were used in the

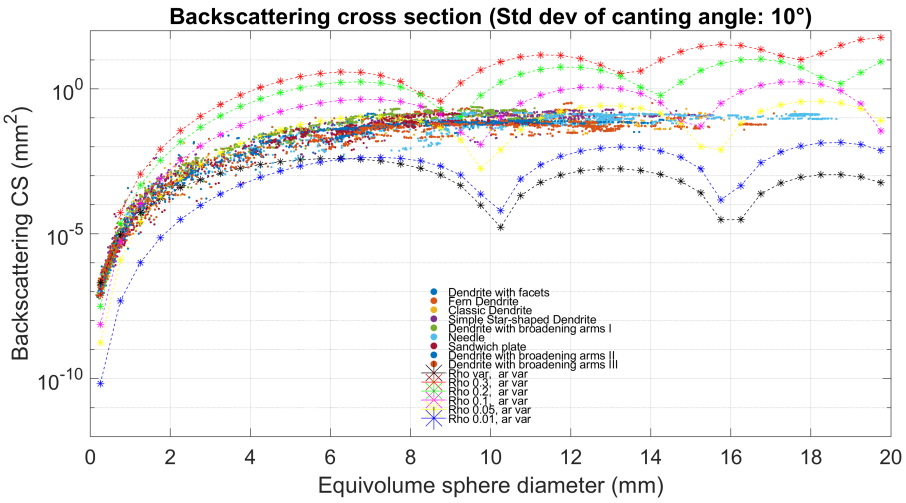

Fig. 4.10: Backscattering cross sections at 24 GHz. Dots represent the NASA DDA database values. Lines with stars stands for the CANTMAT T-Matrix calculations: black line represents the computation where size relations were used and it is provided as reference, the other lines stand for the simulations in which the aspect ratio depends on the particle diameter, whereas the particle density assumes fixed values.

simulations, while the axis ratio was governed by size relation. The results (Figure 4.10) show that, in case of high density, the T-Matrix values are greater than the DDA ones, and the opposite occurs for low density amount. It should be noted that the density value of 0.05 (yellow line) reproduces quite well the NASA database pattern. Such value seems not to be so unrealistic, even though it fails to represent the smaller particles (see Figure 4.6).

Finally, some other simulations were carried out using a canting angle standard deviation depending on hydrometeor diameter, following the literature hints (e.g.Kennedy and Rutledge 2011). The results (not shown) exhibit almost the same patterns of Figures 4.9 and 4.10, meaning that, at least in these CANTMAT computations, the canting angle plays a less fundamental

role on backscattering response variability compared to the particle density and the axis ratio.

4.4 Particle Size Distribution at MZS

Exploiting the Parsivel observations of the two Antarctic expeditions at the Mario Zucchelli research station, the hydrometeor size distributions were derived. Moreover, some quantities for characterization of precipitation were calculated, as well as the accumulated snowfall through the formula introduced in section 3.1.2.

In Figure 4.11 the particle size distribution of the 32nd Antarctic expedition is reported. The PSD behavior confirms the expectations, namely that the ice/snow particles falling in Antarctica are typically very small. For completeness, the probability density function of D_{max}, (the maximum dimension of the hydrometeors) and of D_0 (the median diameter) were computed and

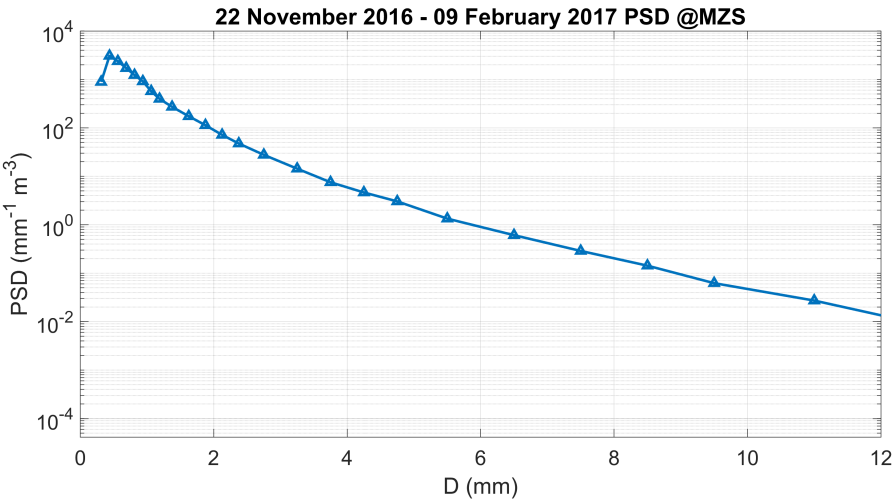

Fig. 4.11: Particle size distribution at the Mario Zucchelli station, calculated through Parsivel data of 32nd Italian Antarctic expedition at MZS.

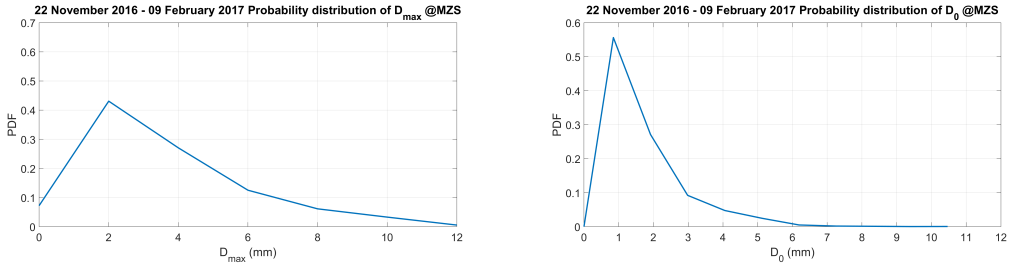

(a) PDF of D_{max} (b) PDF of D_0

Fig. 4.12: Probability density function of D_{max} and D_0, calculated through Parsivel data of 32nd Italian Antarctic expedition at MZS.

are depicted in Figures 4.12(a) and 4.12(b), respectively. The former exhibits a maximum at 2 mm of diameter, the latter shows a probability maximum around 1 mm, both confirming the extremely small particle sizes of the hydrometeors falling at MZS.

Moreover, the spectrograph produced by the Parsivel in the period under consideration is provided (Figure 4.13), showing a quite unusual behavior. In fact, snow particles typically are expected to occupy the low velocity-high dimension bins of the Parsivel spectrograph (see also section 3.1.2 and Figure 3.7), namely the area around the dendrite size-speed reference line depicted in the plot. Instead, the maximum concentrations of hydrometeors (i.e. the most common observed particles) are contained in the small dimension-high speed bins. This is likely due to two simultaneous features: small hydrometeor size, signature of polar and arid regions, and the presence of high-speed wind during observations, a well-known characteristic of the Mario Zucchelli measurement site. Through the Parsivel data an accumulated snowfall value of 297 mm was found in the observation period.

The same analysis was also conducted for the 33rd Antarctic expedition (November 2017 to February 2018). The particle size distribution, depicted

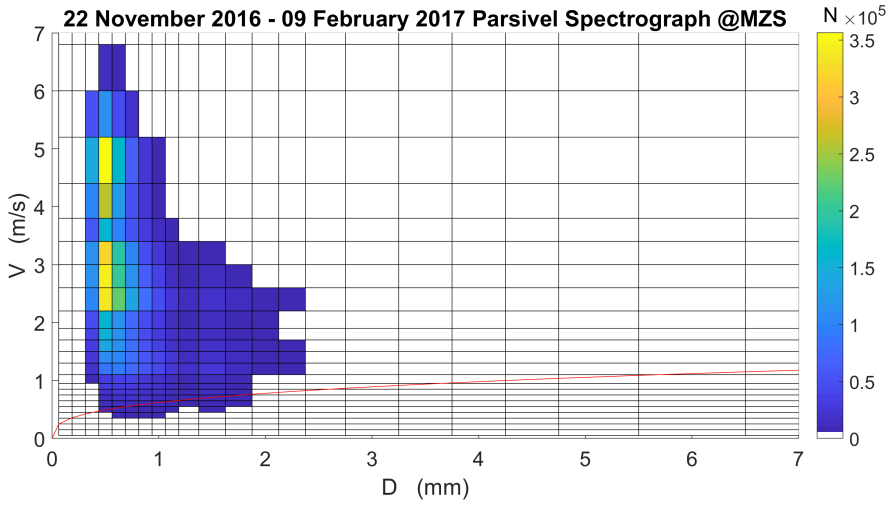

Fig. 4.13: Parsivel spectrograph data of 32nd Italian Antarctic expedition at MZS. Red line represents velocity-speed relation for dendrites (Locatelli and Hobbs, 1974), and it is reported as reference.

in Figure 4.14, shows a pattern similar to the previous year for the larger diameters, while, for the smaller sizes, there seems to be a slight shift toward larger diameters. Also D_{max} and D_0 PDF behaviors (Figures 4.15(a) and 4.15(b)) are consistent with the corresponding measured values of the 32nd expedition. Analyzing the Parsivel spectrograph the slight difference noted in the PSD appears more clear. In fact, it is clear that larger ice particles have been detected by Parsivel during this expedition. Although one maximum of hydrometeor concentration is still located in a quite unrealistic zone, covering bins with velocity between 2 and 3 m/s, the other maximum proves to be almost in agreement with the literature size-speed relation for the solid particles. Lastly, a total amount of 307 mm of snowfall was calculated by the data of the 33rd expedition.

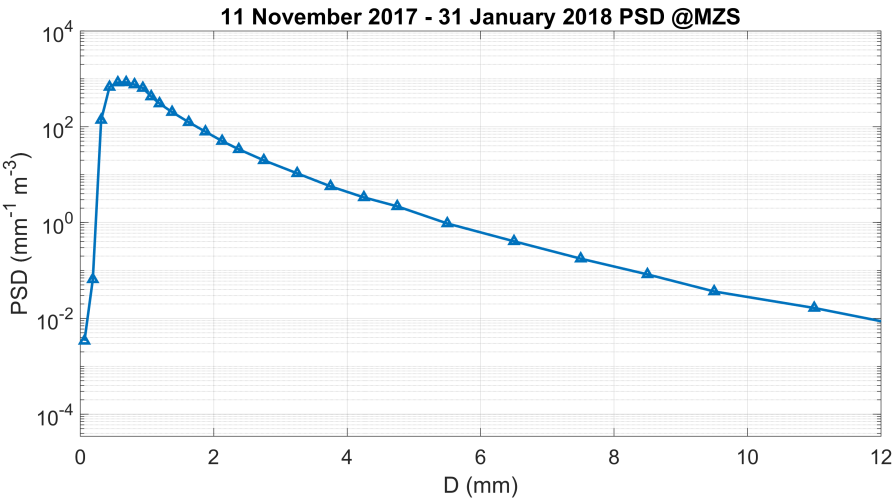

Fig. 4.14: Particle size distribution at the Mario Zucchelli station, calculated through Parsivel data of 33nd Italian Antarctic expedition at MZS.

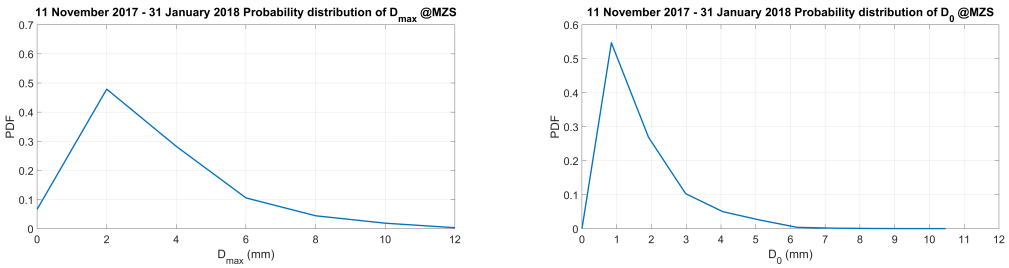

(a) PDF of D_{max}

(b) PDF of D_0

Fig. 4.15: Probability density function of D_{max} and D_0, calculated through Parsivel data of 33nd Italian Antarctic expedition at MZS.

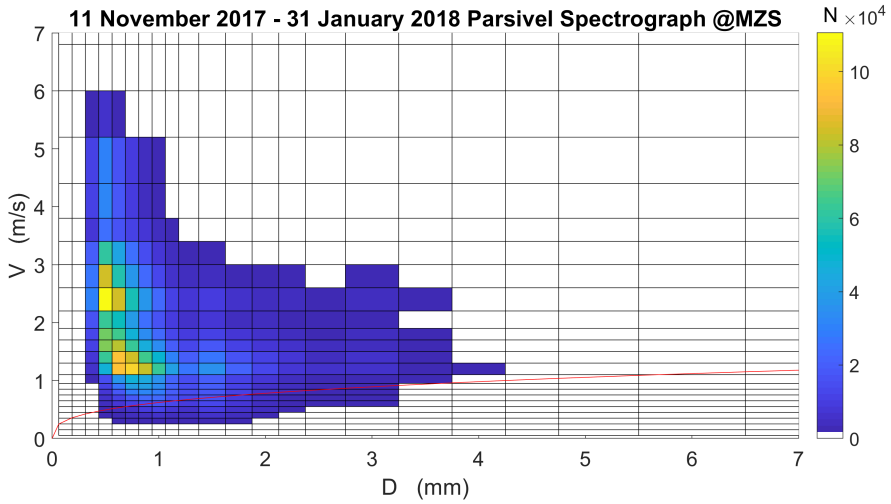

Fig. 4.16: Parsivel spectrograph data of 33nd Italian Antarctic expedition at MZS. Red line represents velocity-speed relation for dendrites (Locatelli and Hobbs, 1974), and it is reported as reference.

4.5 Hydrometeor characterization

The Parsivel disdrometer data and the results of the four backscattering cross section calculations were joined together to compute the simulated equivalent radar reflectivity factor Z_e. The latter was compared with the simultaneous reflectivity measured by the MRR at the first exploitable range gate (i.e. 300 meters above ground level), with the purpose of inferring falling particle features.

In Figure 4.17 the first approach in the evaluation of comparisons is provided. For each precipitation day, the mean value of the observed MRR reflectivity was subtracted from the mean value of each simulated reflectivity, in order to estimate the deviations. The results are plotted versus the mean value of Z_e of the day taken into account. The blue dots represent the errors referred to simulations where the DDA aggregate (hereinafter DDA-agg) database was used, as well as red dots stand for the DDA pristine (here-

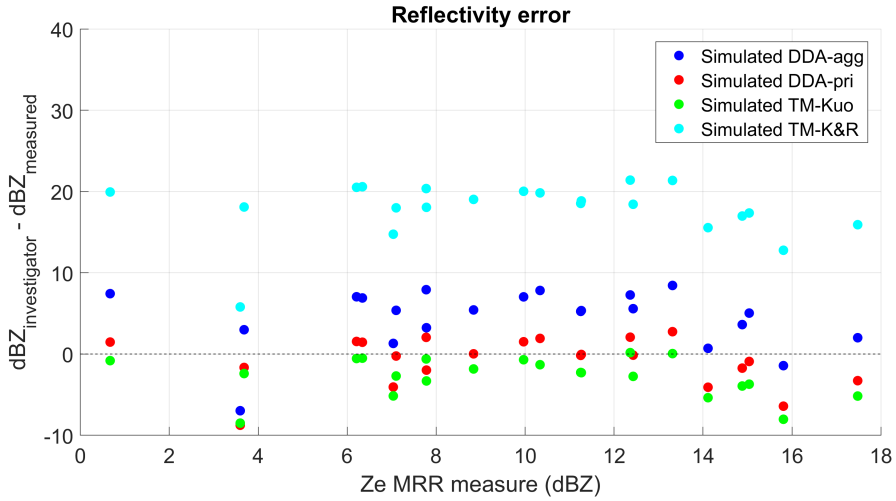

Fig. 4.17: Errors in modeled and actual radar equivalent reflectivity for the 22 precipitation events considered at MZS.

inafter DDA-pri) database. The T-Matrix simulation errors are depicted by green and cyan markers. The former indicates that the CANTMAT code was initialized with the results of DDA-T-Matrix harmonization procedure, while K&R stands for the T-Matrix simulations where the size relations and the canting angle standard deviation by Kennedy and Rutledge (2011) have been used, that in order to try out a literature result in this context. It should be noted that the errors seem to be placed in three different levels. The simulations computed through the DDA-pri and the TM-Kuo are in very good agreement each other and show small errors, especially in the days in which the Z_e mean value is between 6 and 13 dBz. The DDA-agg simulations exhibit higher errors, up to 10 dBz, almost always overestimating the observations, but resulting in a good agreement when large radar reflectivities were measured. Lastly, simulations with the literature T-Matrix inputs for the CANTMAT code, result in an overestimation of the actual Z_e values, proving to be inadequate in all the precipitation days.

This raw analysis was followed by an investigation where proper statistical tools were used, in view of linking each precipitation day to the simulation that estimates the true reflectivity as best. As described in section 3.2.3, the correlation coefficient and the root mean square error were computed for the four simulations each day. A threshold of 0.6 for the correlation coefficient was established for removing simulations with a low degree of correlation with the observations. Then, the computation with the lower value of RMSE, among the simulations belonging to the same day, has been considered as the best estimate. This procedure allowed to classify the precipitation events at MZS into three main groups: days that exhibit an aggregate-like precipitation behavior, a pristine-like behavior or unclassified events. The first contains days in which the DDA-aggregate simulation displays the small RMSE value.

Observation period	Aggregate	Pristine	Unclassified
22/11/2016 - 09/02/2017	6	2	3
11/11/2017 - 31/01/2018	0	8	3
Total	6	10	6

Table 4.1: Precipitation events at MZS during the 32nd and 33rd Antarctic expeditions, classified by the best simulation estimate.

The second consists of days where the DDA-pristine and the T-Matrix (Kuo) simulations are the best estimates. These two simulations, showing a very similar behavior (as already depicted in Figure 4.17) and resulting in comparable statistical values, were placed in the same grouping. As unclassified event was considered a day with poor correlation degrees (cc<0.6), often a day with short-living of precipitation or with prolonged weak precipitation.

Classifying the snowfall days at the Mario Zucchelli station using the three described groups allowed us to categorize the 22 precipitation events, that are summarized in Table 4.1. The aggregate-like events were concentrated in the season 2016/2017, while no entry was found in the following observation period. A high occurrence of the pristine-like feature was found during the 33rd Antarctic expedition. In 6 snowfall days none of the simulations has given reliable statistical index values, resulting in 6 unclassified events. Some case studies are presented as examples for each grouping, in order to point out the peculiar features of the precipitation events.

Aggregate-like event

A snowfall amount of 37.8 mm was recorded at MZS on 17 December 2017, due to a well organized low pressure system approaching the research area

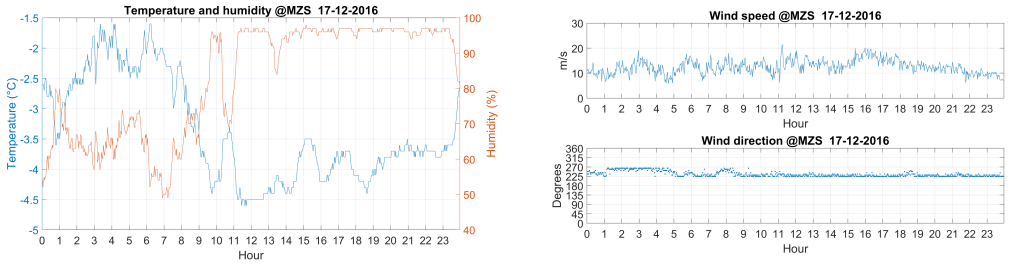

(a) Temperature and humidity

(b) Wind speed and direction

Fig. 4.18: Meteorological conditions at MZS on 17 December 2016.

from the Ross Sea. High-speed wind (up to 20 m/s) affected the station from a direction almost parallel to the coastline (Figure 4.18(b)), suggesting the presence of the so-called barrier wind (see section 1.2). Temperature and humidity show an opposite behavior: the former decreased whereas the latter increased (Figure 4.18(a)). This is likely due to the occurrence of continuous precipitation, especially during the second half of the day. The MRR equivalent reflectivity measurements are shown in Figure 4.19, where the time is reported along the x-axis, whereas the y-axis represents the height above the instrument. The graph shows a well organized precipitation pattern that reaches the first exploitable range gate of MRR (300 meters) with high dBz values. These have been compared with the four Z_e simulations and the results are reported in Figure 4.20. It should be noted the good agreement between the simulation in which the DDA aggregate database was used and the reflectivity observed. The pristine and the T-Matrix (with Kuo relations) simulations underestimate the actual values, while the CANTMAT outputs, initialized with the literature relations, substantially overestimates. The good agreement is also confirmed by statistical indexes. The correlation coefficient is 0.76 for the DDA-agg simulation, coupled with a RMSE value of 3.9 dBz. The other simulations show similar correlation coefficients, but

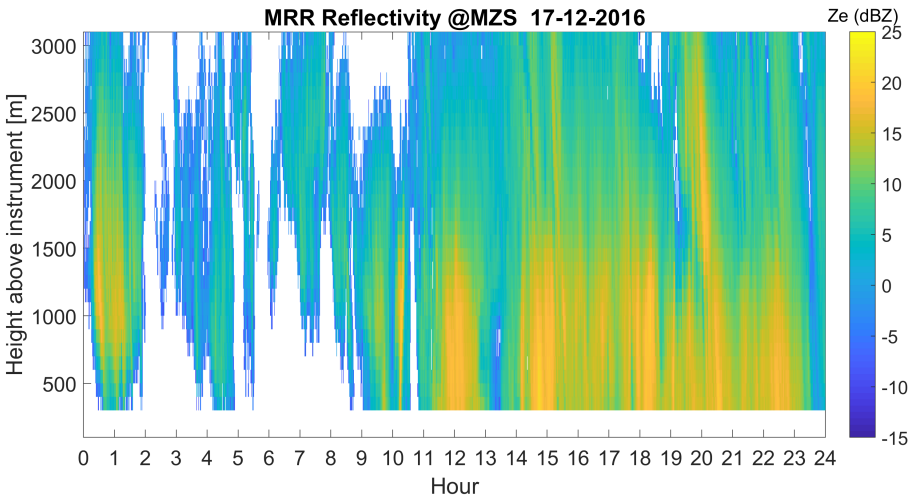

Fig. 4.19: Equivalent reflectivity measured by Micro Rain Radar at the Mario Zucchelli research station on 17 December 2016.

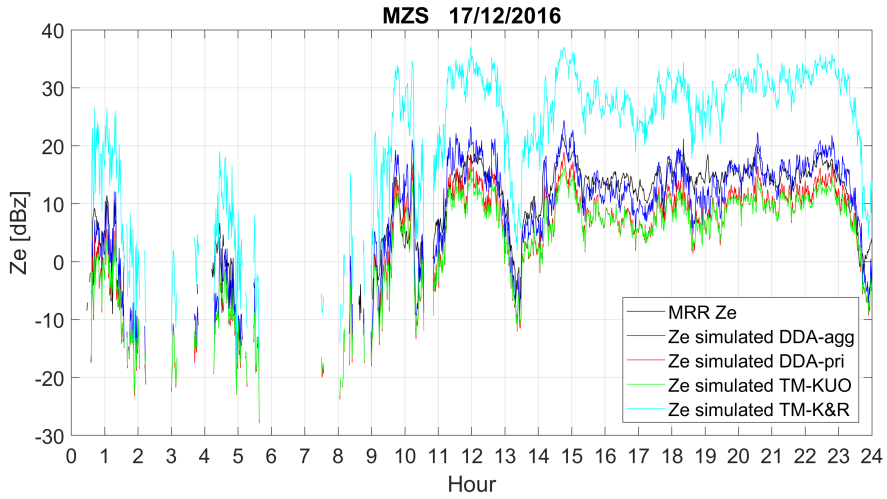

Fig. 4.20: Equivalent reflectivity measured by Micro Rain Radar (black line) on 17 December 2016 is reported together with the four Z_e simulations.

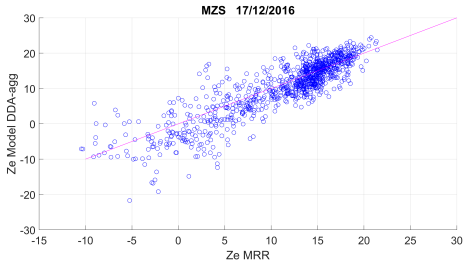

(a) Z_e observed versus Z_e simulated using DDA aggregate database.

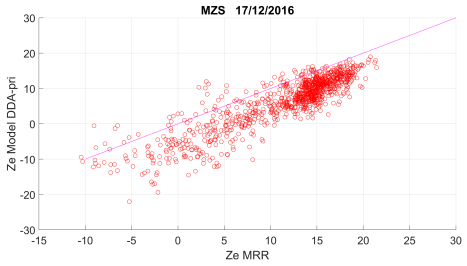

(b) Z_e observed versus Z_e simulated using DDA pristine database.

Fig. 4.21: Scatter plots: measured versus simulated Z_e values at MZS on 17 December 2016.

the RMSE values are much higher. Scatter plots are provided in Figure 4.21, note the concordance between the DDA-agg simulation and the observations, and the underestimation in the case of the DDA-pristine database. Finally, the spectrograph and the PSD gathered by the Parsivel are also provided (Figure 4.22). Both seem to trace well the seasonal observations (Figures 4.13 and 4.11). Especially, the Parsivel retrieved small dimension of particles together with a high speed, quite unrealistic, likely due to the windy conditions. Moreover, a large variability of hydrometeor velocity is reported together with a small dimensional spread. Both features reflect on the peaked particle size distribution. This spectrograph behavior seems to be peculiar

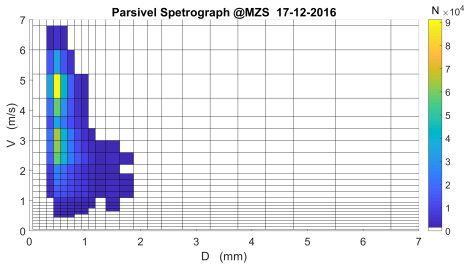

(a) Spectrograph.

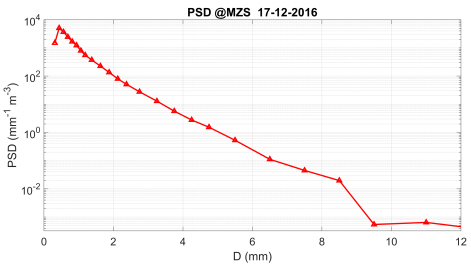

(b) Particle size distribution.

Fig. 4.22: Parsivel observations at MZS on 17 December 2016.

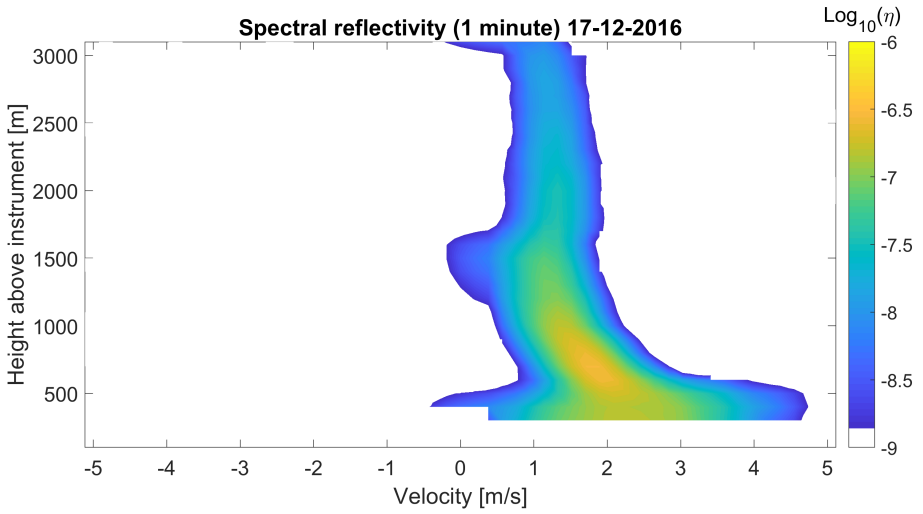

Fig. 4.23: Spectral reflectivity (1 minute) measured by Micro Rain Radar on 17 December 2016.

of aggregate-like precipitation events, that have a strong presence during the 32nd Antarctic expedition. The high hydrometeor speed variability is also confirmed by the spectral reflectivity measured by the Micro Rain Radar. Here, an example of one minute (that with the highest reflectivity value was chosen) of the MRR spectra is shown (Figure 4.23). At the lower levels the velocities are larger than those at the upper ones, and span up to 5 m/s. Hence, it is clear that windy conditions result in a higher impact close to the ground than in the upper atmospheric levels, increasing the turbulence and, consequently, impacting on the particle velocities.

Pristine-like event

In this section, two case studies are presented in order to point out the different behaviors in the Parsivel observations when a pristine-like event occurs.

A temperature slightly below 0°C and a wind speed between 5 and 10 m/s

were observed at MZS on 25 January 2018 (not shown). In Figure 4.24 the Micro Rain Radar measurements were reported, and shows a well structured precipitation event and some ice virga, namely streaks of ice particles falling out of a cloud but evaporating or sublimating before reaching the ground. A total amount of 39 mm of snowfall was recorded in that day. Comparing simulated and actual Z_e values, the DDA pristine database and the T-Matrix with Kuo size relations seem to be the best estimates. The statistical indexes show correlation coefficients well above 0.7 for both simulations, and a RMSE around 4 dBz. Whereas, the DDA-agg and the other T-Matrix simulation result in a strong overestimation. The latter is evident analyzing the two scatter plots of the DDA driven simulations versus the actual MRR observations (Figure 4.26). Lastly, the Parsivel measurements were also analyzed (Figure 4.27) for the purpose of inferring microphysical features of precipitation. A well-defined speed-size zone in which particles concentration is rather high is presented in the spectrograph. The same pattern can be found

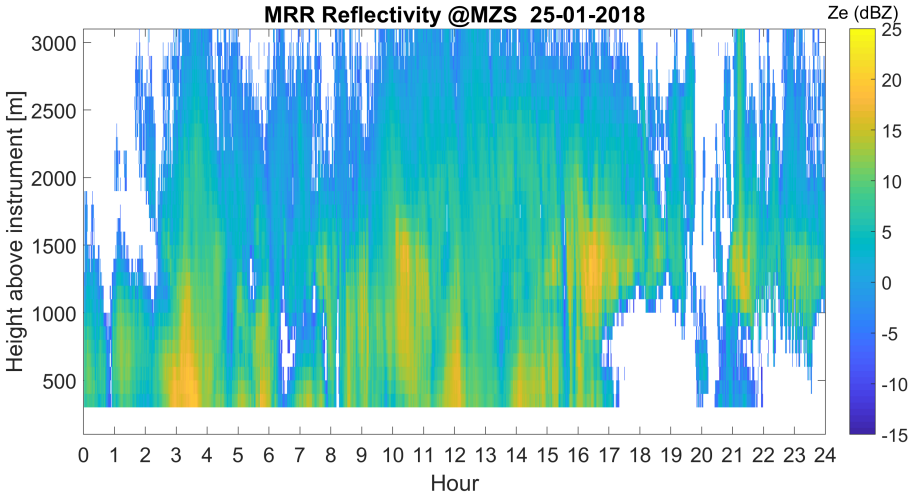

Fig. 4.24: Equivalent reflectivity measured by Micro Rain Radar at the Mario Zucchelli research station on 25 January 2018.

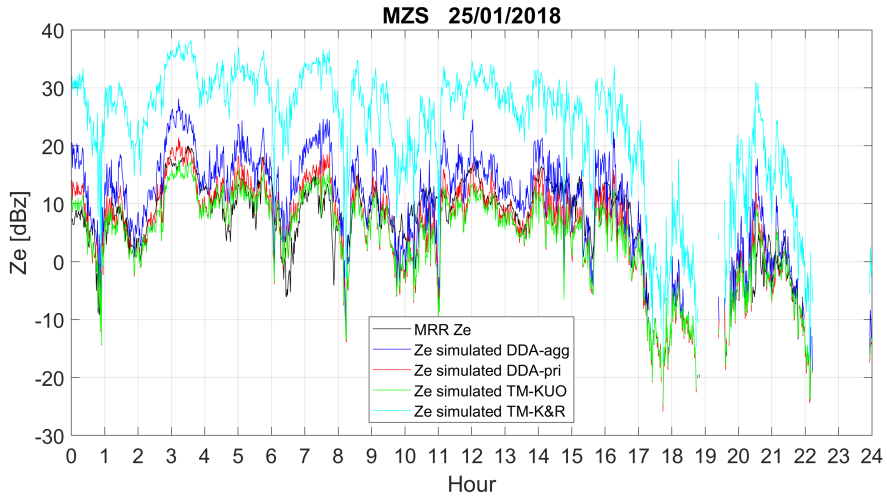

Fig. 4.25: Equivalent reflectivity measured by Micro Rain Radar (black line) on 25 January 2018 is reported together with the four Z_e simulations.

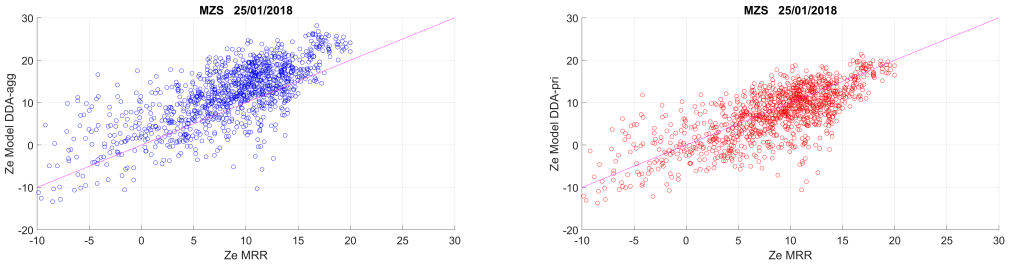

(a) Z_e observed versus Z_e simulated using DDA aggregate database.

(b) Z_e observed versus Z_e simulated using DDA pristine database.

Fig. 4.26: Scatter plots: measured versus simulated Z_e values at MZS on 25 January 2018.

in the seasonal diagram (Figure 4.16), coupled by another maximum of larger particles. The PSD on 25 January highlights hydrometeors slightly bigger than those on 17 December. Moreover, the PDF distribution is more spread out for larger diameters, probably hinting to the presence of different types of falling particles that reached the ground.

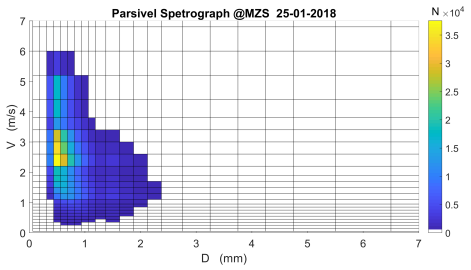

(a) Spectrograph.

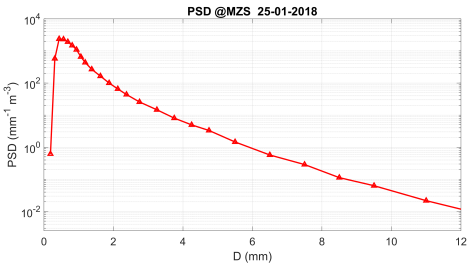

(b) Particle size distribution.

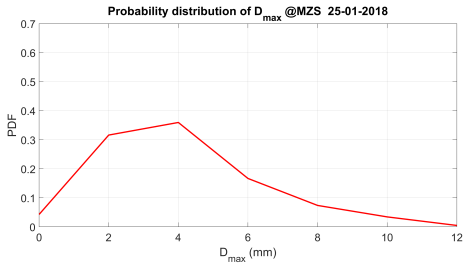

(c) PDF of D_{max}

Fig. 4.27: Parsivel observations at MZS on 25 January 2018.

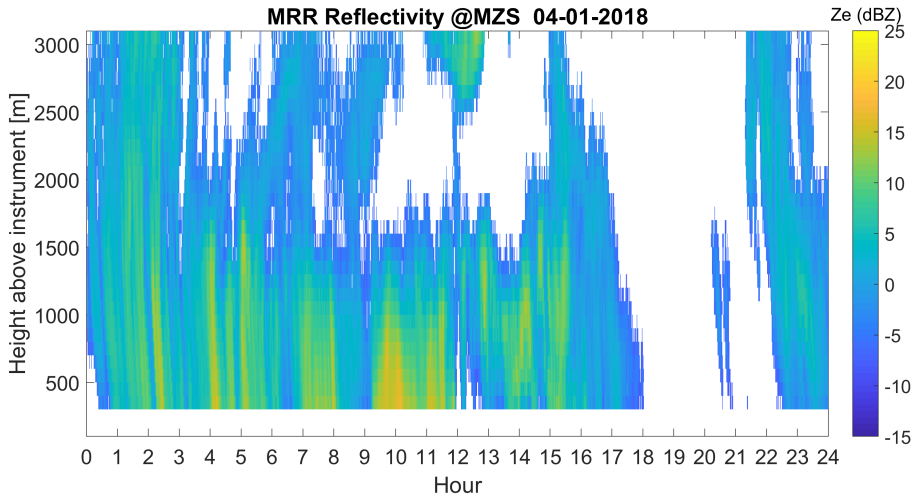

Fig. 4.28: Equivalent reflectivity measured by Micro Rain Radar at the Mario Zucchelli research station on 4 January 2018.

Low-speed wind conditions and temperature around -10°C were reported on 4 January 2018 in the first half of the day, when weak precipitation (Figure 4.28) affected the research station, accumulating a snowfall of 23.8 mm. The equivalent reflectivity simulations are drawn in Figure 4.29 and compared with the values observed by the MRR. Again, the actual MRR Z_e measures are correctly simulated by the DDA-pristine and the T-Matrix (Kuo based) computations. The correlation coefficients are 0.79 and 0.81 respectively, with the RMSE values around 4 dBz. The DDA-agg simulation shows a higher value for RMSE and a lower coefficient of correlation. Moreover, it must be reported that the deviation between the daily average of the true measurements and the daily mean value of simulations is only 0.022, thus resulting in a nearly complete agreement. In Figure 4.30 the two DDA scatter plots are provided. Note the pretty good agreement of the pristine simulation, especially for higher dBz values, and the overestimation of the aggregate computation, together with a larger spread of the data. The Parsivel obser-

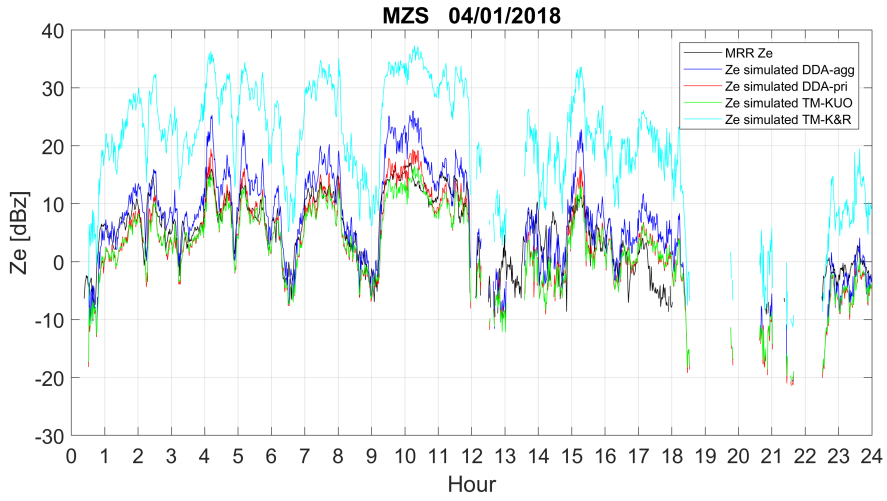

Fig. 4.29: Equivalent reflectivity measured by Micro Rain Radar (black line) on 04 January 2018 is reported together with the four Z_e simulations.

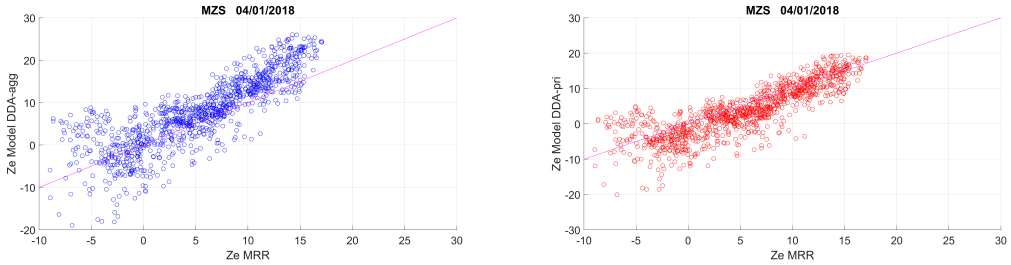

(a) Z_e observed versus Z_e simulated using DDA aggregate database.

(b) Z_e observed versus Z_e simulated using DDA pristine database.

Fig. 4.30: Scatter plots: measured versus simulated Z_e values at MZS on 04 January 2018.

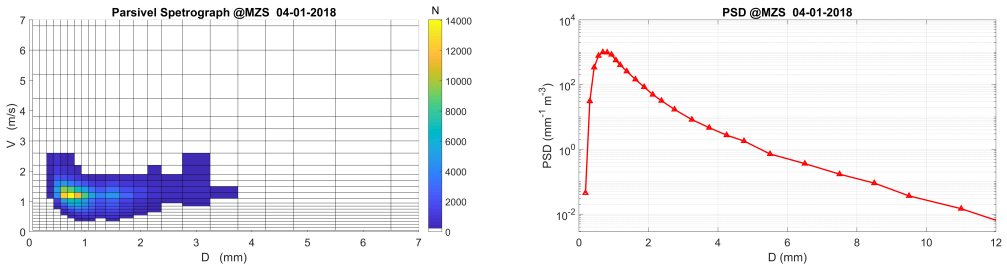

(a) Spectrograph. (b) Particle size distribution.

Fig. 4.31: Parsivel observations at MZS on 4 January 2018.

vations provided the size-velocity plot and the particle size distribution that are depicted in Figure 4.31. The spectrograph exhibits a peculiar behavior because of the large particles with a low falling speed reported in this event. The concentration peak is in accordance with the maximum present in the Parsivel graph of the 33rd Antarctic expedition. Also a high dimensional variability is evident, the opposite of that gathered by the disdrometer in the aggregate-like event presented above (Figure 4.22(a)). The low speed

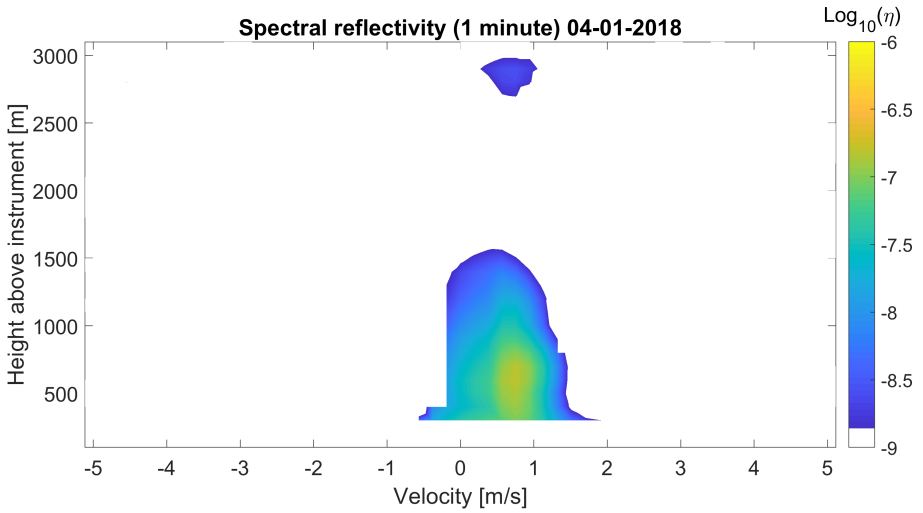

Fig. 4.32: Spectral reflectivity (1 minute) measured by Micro Rain Radar on 04 January 2018.

variability and the low turbulence conditions are also confirmed by the spectral reflectivity computed by the MRR (Figure 4.32). In the precipitation column, the velocities of the hydrometeors span between 0 and 1 m/s, in according with the typical snowflake fall speed. The observed PSD is slightly shifted towards larger diameters, and the peak appears wider in comparison with the particle size distributions of the other case studies.

Unclassified event

In 6 precipitation events of the observation periods, the methodology followed in this thesis fails, because the comparison between the measurements and the simulations show poor or even negative correlation values. One of these events is presented.

Heavy snowfall was recorded at MZS on 13 January 2018, coupling with a high-speed wind conditions (up to 20 m/s). The MRR radar observations captured the beginning of precipitation just before 19:00 UTC (Figure 4.33). A decrease in snowfall, indicated by low dBz values, is evident from 21:00 UTC to 23:00 UTC, then heavy precipitation started over again. In Figure 4.34 the comparison measurements-simulations is illustrated. Analyzing the plot, it is clear that the drop of the MRR reflectivity (black line) is not followed by a reduction of the simulation values, that instead show some peaks. Hence, the Parsivel at the ground continuously observed many particles, while co-located and simultaneous radar measurements gathered pretty low dBz values 300 meters above the ground. This could be due to a well-known peculiar feature of cold and windy regions. In fact, the fresh snow accumulated at the ground can be lifted in case of strong wind, giving rise to the so-called blowing snow. This phenomenon makes the precipitation measurement really hard, and the Parsivel disdrometer observations prove

to be inaccurate in these situations. Due to the marked difference between simulation and MRR true values, the correlation coefficient turn out to be negative (Figure 4.35), and the methodology applied is not able to classify

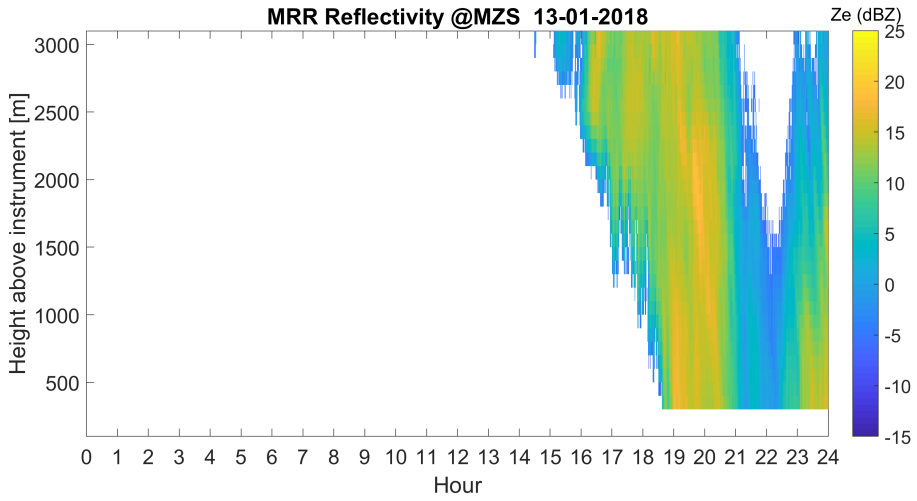

Fig. 4.33: Equivalent reflectivity measured by Micro Rain Radar at the Mario Zucchelli research station on 13 January 2018.

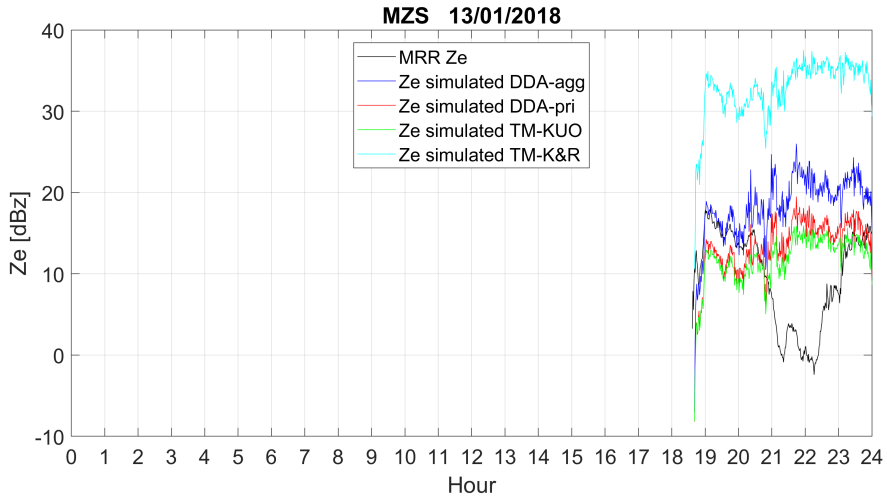

Fig. 4.34: Equivalent reflectivity measured by Micro Rain Radar (black line) on 13 January 2018 is reported together with the four Z_e simulations.

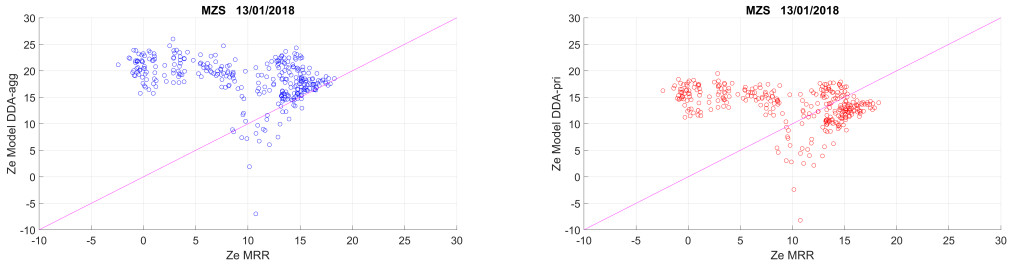

(a) Z_e observed versus Z_e simulated using DDA aggregate database.

(b) Z_e observed versus Z_e simulated using DDA pristine database.

Fig. 4.35: Scatter plots: measured versus simulated Z_e values at MZS on 13 January 2018.

this event.

Chapter 5

Discussion and conclusion

5.1 Discussion

5.1.1 DDA - T-Matrix comparison

Once the harmonization procedure was applied, the comparison between the T-Matrix and the DDA methods was executed and evaluated. The results, presented in the previous section, confirm the conclusions of several studies (e.g. Ori *et al.* 2014; Kuo *et al.* 2016; Falconi *et al.* 2018), in which the scattering problems and the two scattering methods were deeply investigated, although no one dealt with the electromagnetic responses of ice particles at 24 GHz (K-band), as carried out in this work. In fact, the graph of the comparison (Figure 4.8) shows that the T-Matrix cross section values are higher than the DDA ones for small particles, but lower for larger particles, as reported in Falconi *et al.* (2018). Actually, the difference is rather small at small diameters, thus the two methods seem to achieve the same results, whereas the gap increases with increasing diameters, resulting in a difference of several orders of magnitude.

The difference in the response at the larger sizes can be interpreted as the consequence of the spheroidal approximation made by the T-Matrix. Indeed, as long as ice particles are quite small, the approximation of the crystal shape with a spheroid seems to work properly. On the other hand, such approximation fails to model the complex shapes of lager particles, as snow aggregates, that deviate significantly from the spheroidal form.

Moreover, analyzing the results of the simulations (Figure 4.9 and 4.10) it is clear that they are strongly influenced by the size relations used, that act as tuning parameters. Indeed, the backscattering cross sections can vary considerably due to the density and axis ratio values used as input in the CANTMAT code. This means that, in the T-Matrix simulations, the choice of the right size relations, or of the right density and axis ratio values, is a fundamental issue to deal with. As already considered in section 4, the canting angle values used into the CANTMAT code, seem to influence less the outcomes of the simulations. Despite of this secondary role, also the selection of the proper value of the canting angle is a challenging question. It should be underlined that, in this thesis, the NASA database pre-compiled by the DDA method, was considered as reference. Hence, the tuning parameters for the T-Matrix simulations were derived from the DDA database in order to make an appropriate comparison between the two methods. It is nonetheless true that also to compute the DDA database proper size relations must be used, thus running into the same T-Matrix issues.

These considerations imply that the backscattering cross section values, or more generally the scattering properties of hydrometeors, depend deeply on the relations that linked the microphysical quantities of ice particles, as density, dimensions and axis ratio. Hence, compared to this, the decision of the method to be used in the scattering problems seems to be a secondary

issue. Furthermore, the retrieval of microphysical parameters of solid hydrometeors is not trivial. A great experimental effort is required in order to provide an adequate characterization of ice and snow particles. This is the reason why size relations derived from the literature are often used.

5.1.2 Microphysical observations

Obtaining and evaluating the particle size distributions of hydrometeors at the Mario Zucchelli research station is one on the aims of this thesis. To reach this goal the Parsivel disdrometer data, collected during the austral summers 2016-2017 and 2017-2018, were processed and evaluated. This represent the first analysis in which microphysical data of two seasons from MZS have been used.

Both PSD (Figures 4.11 and 4.14) highlight the presence of very small ice particles during the summer periods. This feature is consistent with the dimensions measured at other Antarctic locations (Lachlan-Cope *et al.* 2001; Gay *et al.* 2002; Walden *et al.* 2003), reporting values between 0.03 and 0.6 mm. It must be underlined that most of these observations are referred to research stations very far from the sea. On the Antarctic coast, due to the influence of the ocean on the atmospheric moisture amount, the particle dimensions are expected to be slightly larger, and this proved to be in reasonable agreement with the microphysical results found at MZS. Moreover, Gorodetskaya *et al.* (2015) reported that photographic observations of the fallen snow crystals at the Princess Elisabeth research station captured a maximum size of 0.5-0.8 mm, whereas Souverijns *et al.* (2017) indicated that the snow particles over the PE station have a median diameter around 0.7 mm. Considering the position of the PE station, a few hundred kilometers away from the coastline, both the maximum dimension and the median

diameter of the hydrometeors found at MZS are consistent with the PE observations.

Analyzing the spectrographs (Figures 4.13 and 4.16), the influence of high-speed wind in the Parsivel retrieval cannot be neglected. As stressed in section 3.1.2, the disdrometer betrays a lack of accuracy during windy days. The spectrograph of the first observation period (2016-2017) exhibits a very high number of small particles, coupled with an unrealistic fall speed. This can be considered a peculiar signature of recurring high-speed wind conditions at MZS. This well-known drawback of the instrument was deeply investigated by Friedrich *et al.* (2013a,b). They found an artifact in the Parsivel observations represented by an unusual large number concentration of hydrometeors with large diameters and low fall speed in windy conditions. This characteristic feature was not found in the Parsivel measurements at MZS, where small particles with unrealistic high speed were clearly detected when strong winds blew. This disdrometer limitation should be born in mind when interpreting the Parsivel data, and further mitigation measures must be devised and applied in order to improve the retrieval of the disdrometer.

However, the high number of small hydrometeors captured by the instrument in windy conditions could also be caused by other factors, as well as due to the intrinsic limitation in small particles detection of the Parsivel (Battaglia *et al.*, 2010). Blowing snow contributes to the near ground snow flux, and is particularly effective in recirculating small and light particles (e.g. Mann *et al.* 2000; Gordon and Taylor 2009). Gorodetskaya *et al.* (2015) report a threshold of 8 m/s, as wind speed needed for lifting snow from the ground, a value often exceeded at MZS. Moreover, as evaluated by Vardiman (1978) and supposed by Grazioli *et al.* (2017b), a contribution to small particles may be the fragmentation of aggregates, in particular at the

lower levels of the atmosphere, due to the mechanical breakup caused by strong wind and turbulence. Both these effects can be key contributions to the high concentrations and to the unrealistic velocities of the small particles observed.

Finally, the accumulated snowfall amount was calculated for each Antarctic expedition using the Parsivel data in spite of its limitations. The formula presented by Huang *et al.* (2010) was used, even though it was derived for 2DVD disdrometer that measures two sizes of each ice particle. The snowfall rate, calculated through such formula, proves to be very sensitive to the density-size relation used. Moreover, the observation periods are limited to just a few months. For these reasons, it is therefore difficult to compare the results obtained in this analysis with the other annual estimates of accumulated snowfall at MZS reported in the literature, although, at first glance, they seem to be substantially higher, confirming that the quantification of precipitation in the coastal regions of Antarctica remains a difficult task.

5.1.3 Hydrometeor characterization

The simulated equivalent radar reflectivity factor was calculated through the formula 3.27, using the outcomes of the four backscattering cross section computations and the particle size distributions. Comparing the simulated Z_e values with the simultaneous actual reflectivity measured by the Micro Rain Radar, the features of the precipitation at MZS can be deduced. Despite of the uncertainties of the Parsivel measurements, considering the various approximations made in the DDA database processing and in the T-Matrix computations, as well as the distance between the lowest measuring range of MRR (300 m) and the Parsivel instrument at the ground, the comparisons result in an unexpected agreement, albeit in 6 precipitation events the

methodology failed. For the aggregate-like events the mean value of the correlation coefficient is 0.68, well over the fixed threshold, whereas the RMSE mean is slightly more than 5 dBz. The precipitation days classified as having pristine-like features exhibit a mean Pearson index of 0.69 together with 4.9 dBz as RMSE average. These indexes show that the methodology works generally well.

Moreover, two comments on the scattering methods can be derived from these comparisons. First, the DDA aggregate and pristine databases reproduce satisfactorily the scattering properties of ice particles at MZS, second, the T-Matrix simulations again appear to be very sensitive to the size relations. In fact, a good correspondence between the T-Matrix method and the DDA-pristine was found when the CANTMAT code was initialized with the relationships obtained from the NASA database, even though such relationships have been derived only from the aggregate database. This confirms that the T-Matrix seems to be having trouble in dealing with aggregate particles. Instead, when the literature relations were used in the CANTMAT code, the simulations result in a systematic overestimation of the actual reflectivity values.

The classification of the events reveals that ice particles frequently exhibit an aggregate- or pristine-like form at MZS. The only other categorization, in the coastal regions of Antarctica, was carried out by Grazioli *et al.* (2017b) that classified the hydrometeors exploiting the polarimetric data of the MX-Pol radar at the DDU research station. They observed, at 400 m above the ground, a proportion of three particle types with about 10% of rimed snowflakes, 40% of aggregates and 50% of crystals, albeit at the ground the majority of the hydrometeors (54%) was identified as small particles, and 20% was by aggregates. This research can in part confirm the results found

in this thesis inasmuch the presence of tiny solid hydrometeors and a substantial number of aggregates have been recognized. However, as opposed to Grazioli *et al.* (2017b), the methodology applied in this dissertation does not allow to discriminate multiple types of hydrometeors in the same event, thus loosing the fine variability in the habits of particles during precipitation.

Analyzing the meteorological observations at the research station, a high correlation was found between the occurrences of aggregate-like precipitation and high-speed wind conditions. Going in depth, we found that aggregate events always take place together with barrier wind, namely when southwesterly flow, almost parallel to the coast-line, blows at ground level. Thus, we can speculate that the aggregate events are intrinsically related to the presence of a large low pressure system offshore over the Ross Sea, that pushes air masses from the ocean towards the steep coast, increasing the moisture and promoting aggregates formation. Furthermore, the turbulence and the high-speed wind could broke the aggregates at lower levels, as mentioned before, explaining the high concentration of small particles captured by the disdrometer. The pristine-like episodes are found to occur mainly in conjunction with a low-speed wind with variable direction. Moreover, they seem to be related to a meteorological pattern in which the air masses originating from the inner part of Antarctica (where single crystal precipitation have repeatedly been observed (e.g. Lachlan-Cope *et al.* 2001; Walden *et al.* 2003) likely due to the extremely low humidity level) to reach the Mario Zucchelli station.

On the other hand, the last two points can also be interpreted as due to the difficulty of the Parsivel in ice particles detection, giving rise to observations biased because of the wind. This is the reason why another type of ground instrument (e.g. 2DVD, MASC) or photographs of the falling parti-

cles could be helpful to completely demonstrate the validity of the methodology presented in this work. Actually, a photograph of the hydrometeors at

Fig. 5.1: Picture of the fallen hydrometeors at the Mario Zucchelli research station on 2 December 2016.

MZS was taken on 2 December 2016. That day was classified as an aggregate-like episode (correlation coefficient=0.65, RMSE=5.5 dBz) by the method presented in this thesis. The hydrometeors depicted in the picture seem to be snowflakes aggregates having dimension around 1 mm (Roberto *et al.*, 2018), confirming the validity of the methodology.

It should also be stressed that the importance of a correct classification of the hydrometeors lies in the possibility of using the appropriate density-size relation in each precipitation episode. This relationship represents a key term in the snowfall rate formula, and therefore in the calculation of the total snowfall accumulation at the ground, that is the fundamental input for establishing the hydrologic cycle of Antarctica.

Finally, as well demonstrated by the unclassified event presented in section 4, comparing simulated Z_e values from Parsivel observations with the reflectivity measured by the Micro Rain Radar, the blowing snow episodes can be detected. In fact, the height above the ground of the lowest MRR gate (300 m) can be considered not affected by this phenomenon (e.g. Gordon and Taylor 2009; Scarchilli *et al.* 2010), which rarely exceeds 200 meters of vertical development (Grazioli *et al.*, 2017b). Hence, according to Grazioli *et al.* (2017b), the synergetic use of remote sensing and in-situ measurements can overcome in part the problem of the phantom precipitation, detecting, and therefore removing, the contribution of the blowing snow to the total accumulation. The main limit of this treatment seems to be that it can be applied only to pure blowing snow episodes, hence not when precipitation and blowing snow occur together. Actually, considering the difference between simulated and true reflectivity values an estimate of the contribution of blowing snow could be derived if an appropriate Z_e-S relationship is used. In the same way also the low-level sublimation episodes, due to the dry katabatic winds, can be detected when the reflectivity at 300 meters exceeds considerably the simulated reflectivity at the ground. According to Grazioli *et al.* (2017a), the sublimation of precipitation accounts up to 35% reduction of total snowfall on the margins of East Antarctica, thus posing a serious problem to the measurements of snowfall accumulations as well as to the satellite-based estimations of precipitation.

5.2 Outlook

Several approaches are conceivable to improve the analysis of precipitation from ground observations at the Mario Zucchelli station. The data-set eval-

uated in this thesis covers only two summer periods, namely a few months of observations. Using the new data, including, for the first time, a whole Antarctic year, can allow a more extensive discussion of the results presented in this dissertation, being based on a more appropriate set of data.

Moreover, exploiting these new observations can permit to parameterize the particle size distribution of hydrometeors, thus increasing the knowledge of precipitation structure at Terra Nova Bay. In addition, such parameters can be used as input into a recent development of the NASA-DDA website that allows to generate several DDA-databases varying the mass-dimension relation and the size distribution constants. Hence, DDA-databases suited for Antarctic precipitation can be produced and then utilized to simulate the reflectivity factor using the method discussed in this thesis. Then, minimizing the gap between actual and simulated Z_e, a proper mass-size relation for the Antarctic precipitation can be attained. This would be a key point in the snowfall estimation at MZS. In fact, a suitable mass-size relation is essential for the snowfall rate calculation, as previously discussed and, for this purpose, the formula and the method presented in Souverijns *et al.* (2017) can be followed and utilized.

Furthermore, thanks to the discrimination of precipitation episodes investigated in this thesis, an appropriate mass-size relation can be obtained for pristine/aggregate-like precipitation events, improving the qualitative measurement of snowfall accumulation significantly. This is needed to better assess the surface mass balance in the Antarctic region.

The precipitation events can be investigated in detail by the use of the repaired Micro Rain Radar, that will be installed during the next Antarctic expedition at MZS. Using a vertical resolution of 25 meters, the atmospheric layers closer to the ground can be explored in more detail.

Moreover, the classification of precipitation events deserves to be looked at more closely. Using the new Parsivel observation as well as the new MRR measurements, the method can be improved, contributing to refine the detection criteria. Adding the European Center for Medium-Range Weather Forecasts Interim re-analysis data, each pristine/aggregate event can be analyzed in relationship to the synoptic weather systems.

Furthermore, from simultaneous measurements of MRR reflectivity factor and snowfall rate, the Ze-SR power law relationship can be derived. This would allow to estimate unambiguously the snowfall accumulation in case of strong wind as well as the low-level sublimation of snowfall.

According to Grazioli *et al.* (2017a), also a sublimation ratio (SBR) can be obtained through equation 5.1,

$$SBR = \frac{S_{max} - S_{ground}}{S_{max}} \tag{5.1}$$

where S_{max} represents the maximum of snowfall accumulation calculated by the Ze-SR relationship and S_{ground} is the accumulated precipitation at ground, thus comparing the computed values to those of the other Antarctic research stations (e.g. Dumont D'Urville). Other comparisons can be carried out between satellite-based snowfall accumulations and ground based observations at MZS, detecting the effects of the sublimation. The sublimation analysis can also be studied with the aid of radiosonde measurements that are conducted twice a day at MZS.

Finally, the data collected can be organized into a valuable database. This would allow not only the opportunity to investigate in detail the snowfall events, their spatial and temporal occurrence and frequency at MZS, but also it would support the validation and calibration of satellite-based measurements. The database would be also helpful to the next satellite mission EarthCARE, offering a precious validation site over the Antarctic region.

5.3 Conclusion

Despite their fundamental contribution in the assessment of the Antarctic hydrologic cycle, the measurements of precipitation at the ground over the southern polar region are scarce and not adequate to detail precipitation properties. In order to fill this gap, some research programs in Antarctica have been funded over recent years. One of them is the Italian APP-PNRA project ("Antarctic precipitation properties from ground-based instruments") that aims to set up an observatory for investigating the precipitation at the Mario Zucchelli research station (MZS).

As part of the APP project, the main goals of this thesis are the evaluation of the response of solid hydrometeors to the electromagnetic radiation at 24 GHz and the microphysical characterization of precipitation at MZS.

The electromagnetic response was explored by two scattering methods, the DDA (Discrete Dipole Approximation) and the T-Matrix. Complex shaped hydrometeors are taken into account by the DDA, while the T-Matrix approximates ice particles as spheroids. The outcomes of the T-Matrix scattering simulations and the backscattering cross sections of a very recent pre-computed DDA database have been compared. The results show that T-Matrix exhibits cross section values higher than DDA for small ice aggregates, whereas lower for larger particles. On the other hand, the methods seem to be in good agreement when the T-Matrix is compared with the DDA database for pristine crystals. These results suggest that the T-Matrix method, computed by the CANTMAT code, has problems in dealing with complex shape hydrometeors as aggregates. In addition, the T-Matrix proves to be very sensitive to the density-diameter and the axis ratio-diameter relations used in the simulations.

The microphysical characterization of precipitation was derived evaluat-

ing the Parsivel disdrometer and Micro Rain Radar observations at MZS during the austral summer seasons 2016-2017 and 2017-2018. The particle size distribution of each season has been computed and the results, in both observation periods, display an evident maximum around 1 mm diameter. Similar sizes were observed in other research stations along the Antarctic coast. Although the PSDs of the two summer seasons show only a slight difference, the Parsivel spectrographs exhibit two well separate patterns. Especially, during the 2016-2017, a peculiar behavior of disdrometer measurements was observed, showing very small particles coupled with unrealistic fall speed. Such signature seems to be due both to the high-speed wind conditions, that can influence the Parsivel retrieval, and to the mechanical break of aggregate hydrometeors caused by wind and turbulence at lower atmospheric levels.

The synergetic use of remote sensing and in-situ measurements as well as of the DDA and T-Matrix scattering methods allowed to discriminate the precipitation days at MZS. The MRR equivalent reflectivity factor at 300 meters above the ground was compared with the simultaneous reflectivity computed with the Parsivel observation and the scattering data. Using the Pearson correlation coefficient and the root mean square error, each precipitation event has been classified as having pristine-/aggregate-like hydrometeor features. Applying this methodology, 6 out of 22 precipitation episodes were identified as aggregate-like, 10 as pristine-like and in 6 days the method turned out to be unsuitable. The relevance of the hydrometeors classification lies in the possibility to compute the snowfall rate using proper mass-density relationships.

The results of this thesis will contribute to providing a more accurate quantification of solid precipitation in the Antarctic continent.

Part of this work was presented as poster contribution at the 10th Eu-

ropean Conference on Radar in Meteorology and Hydrology, July 2018 (P 1.36).

References

Adirosi, E., Baldini, L., Roberto, N., Gatlin, P., and Tokay, A. (2016). Improvement of vertical profiles of raindrop size distribution from micro rain radar using 2d video disdrometer measurements. *Atmospheric Research*, **169**, 404 – 415.

Agosta, C., Fettweis, X., and Datta, R. (2015). Evaluation of the cmip5 models in the aim of regional modelling of the antarctic surface mass balance. *The Cryosphere*, **9**(6), 2311–2321.

Andronache, C. (2018). *Remote Sensing of Clouds and Precipitation*. Springer.

Ardon-Dryer, K., Levin, Z., and Lawson, R. P. (2011). Characteristics of immersion freezing nuclei at the south pole station in antarctica. *Atmospheric Chemistry and Physics*, **11**(8), 4015–4024.

Argentini, S. and Mastrantonio, G. (1994). Barrier winds recorded during two summer antarctic campaigns and their interaction with the katabatic flows as observed by a tri-axial doppler sodar. *REMOTE SENSING*, **15**(2), 455–466.

Argentini, S., Del Buono, P., Della Vedova, A., and Mastrantonio, G. (1995).

A statistical analysis of wind in terra nova bay, antarctica, for the austral summers 1988 and 1989. *Atmospheric research*, **39**(1-3), 145–156.

Atlas, D., Srivastava, R., and Sekhon, R. S. (1973). Doppler radar characteristics of precipitation at vertical incidence. *Reviews of Geophysics*, **11**(1), 1–35.

Bailey, M. and Hallett, J. (2004). Growth rates and habits of ice crystals between -20 and -70 celsius degrees. *Journal of the Atmospheric Sciences*, **61**(5), 514–544.

Bailey, M. P. and Hallett, J. (2009). A comprehensive habit diagram for atmospheric ice crystals: Confirmation form laboratory, airs ii, and other field studies. *Journal of the Atmospheric Sciences*, **66**(9), 2888–2899.

Battaglia, A., Rustemeier, E., Tokay, A., Blahak, U., and Simmer, C. (2010). Parsivel snow observations: A critical assessment. *Journal of Atmospheric and Oceanic Technology*, **27**(2), 333–344.

Belosi, F., Contini, D., Donateo, A., Santachiara, G., and Prodi, F. (2012). Aerosol size distribution at nansen ice sheet antarctica. *Atmospheric Research*, **107**, 42 – 50.

Belosi, F., Santachiara, G., and Prodi, F. (2014). Ice-forming nuclei in antarctica: New and past measurements. *Atmospheric Research*, **145-146**, 105 – 111.

Bohren, C. F. and Huffman, D. R. (2008). *Absorption and scattering of light by small particles*. John Wiley.

Botta, G., Aydin, K., Verlinde, J., Avramov, A. E., Ackerman, A. S., Fridlind, A. M., McFarquhar, G. M., and Wolde, M. (2011). Millimeter wave scat-

tering from ice crystals and their aggregates: Comparing cloud model simulations with x-and ka-band radar measurements. *Journal of Geophysical Research: Atmospheres*, **116**(D1).

Botta, G., Aydin, K., and Verlinde, J. (2013). Variability in millimeter wave scattering properties of dendritic ice crystals. *Journal of Quantitative Spectroscopy and Radiative Transfer*, **131**, 105–114.

Bradley, S. and Stow, C. (1975). Reply. *Journal of Applied Meteorology*, **14**(3), 426–428.

Brandes, E. A., Ikeda, K., Zhang, G., Schönhuber, M., and Rasmussen, R. M. (2007). A statistical and physical description of hydrometeor distributions in colorado snowstorms using a video disdrometer. *Journal of applied meteorology and climatology*, **46**(5), 634–650.

Bringi, V. and Chandrasekar, V. (2001). *Polarimetric Doppler weather radar:principles and applications*. Cambridge university press.

Broadley, S. L., Murray, B. J., Herbert, R. J., Atkinson, J. D., Dobbie, S., Malkin, T. L., Condliffe, E., and Neve, L. (2012). Immersion mode heterogeneous ice nucleation by an illite rich powder representative of atmospheric mineral dust. *Atmospheric Chemistry and Physics*, **12**(1), 287–307.

Bromwich, D. H., Nicolas, J. P., Hines, K. M., Kay, J. E., Key, E. L., Lazzara, M. A., Lubin, D., McFarquhar, G. M., Gorodetskaya, I. V., Grosvenor, D. P., Lachlan, T., and van Lipzig, N. P. M. (2012). Tropospheric clouds in antarctica. *Reviews of Geophysics*, **50**(1).

Chadwick, R., Moran, K., Strauch, R., Morrison, G., and Campbell, W. (1976). Microwave radar wind measurements in the clear air. *Radio Science*, **11**(10), 795–802.

Chen, B., Hu, W., and Pu, J. (2011). Characteristics of the raindrop size distribution for freezing precipitation observed in southern china. *Journal of Geophysical Research: Atmospheres*, **116**(D6).

Cochet, N. and Widehem, P. (2000). Ice crystallization by pseudomonas syringae. *Applied Microbiology and Biotechnology*, **54**, 153 – 161.

Contini, D., Donateo, A., Belosi, F., Grasso, F. M., Santachiara, G., and Prodi, F. (2010). Deposition velocity of ultrafine particles measured with the eddy-correlation method over the nansen ice sheet (antarctica). *Journal of Geophysical Research: Atmospheres*, **115**(D16).

Cristofanelli, P., Calzolari, F., Bonafè, U., Lanconelli, C., Lupi, A., Busetto, M., Vitale, V., Colombo, T., and Bonasoni, P. (2011). Five-year analysis of background carbon dioxide and ozone variations during summer seasons at the mario zucchelli station (antarctica). *Tellus B: Chemical and Physical Meteorology*, **63**(5), 831–842.

Dalgleish, D. I. (1989). *An introduction to satellite communications*. Number 20. IET.

Davolio, S. and Buzzi, A. (2002). Mechanisms of antarctic katabatic currents near terra nova bay. *Tellus A: Dynamic Meteorology and Oceanography*, **54**(2), 187–204.

DeConto, R. and Pollard, D. (2016). Contribution of antarctica to past and future sea-level rise. *Nature*, **531**, 591–597.

Del Guasta, M., Morandi, M., Stefanutti, L., Brechet, J., and Piquard, J. (1993). One year of cloud lidar data from Dumont d'Urville (Antarctica): 1. General overview of geometrical and optical properties. *Journal of Geophysical Research: Atmospheres*, **98**, 18.

DeVoe, H. (1964). Optical properties of molecular aggregates. i. classical model of electronic absorption and refraction. *The Journal of chemical physics*, **41**(2), 393–400.

Diederich, M., Crewell, S., Simmer, C., and Uijlenhoet, R. (2004). Investigation of rainfall microstructure and variability using vertically pointing radar and disdrometer. In *Proceedings of ERAD*, volume 80.

Draine, B. T. (1988). The discrete-dipole approximation and its application to interstellar graphite grains. *The Astrophysical Journal*, **333**, 848–872.

Draine, B. T. and Flatau, P. J. (1994). Discrete-dipole approximation for scattering calculations. *JOSA A*, **11**(4), 1491–1499.

Draine, B. T. and Flatau, P. J. (2008). Discrete-dipole approximation for periodic targets: theory and tests. *JOSA A*, **25**(11), 2693–2703.

Falconi, M. T., Lerber, A. v., Ori, D., Marzano, F. S., and Moisseev, D. (2018). Snowfall retrieval at x, ka and w bands: consistency of backscattering and microphysical properties using baecc ground-based measurements. *Atmospheric Measurement Techniques*, **11**(5), 3059–3079.

Fenni, I., Haddad, Z. S., Roussel, H., Kuo, K.-S., and Mittra, R. (2018). A computationally efficient 3-d full-wave model for coherent em scattering from complex-geometry hydrometeors based on mom/cbfm-enhanced algorithm. *IEEE Transactions on Geoscience and Remote Sensing*, **56**(5), 2674–2688.

Fletcher, N., Squires, P., and Bowen, E. (1962). *The Physics of Rainclouds*. Cambridge University Press.

French, H. and Guglielmin, M. (2000). Frozen ground phenomena in the vicinity of terra nova bay, northern victoria land, antarctica: a preliminary report. *Geografiska Annaler: Series A, Physical Geography*, **82**(4), 513–526.

Friedrich, K., Higgins, S., Masters, F. J., and Lopez, C. R. (2013a). Articulating and stationary parsivel disdrometer measurements in conditions with strong winds and heavy rainfall. *Journal of Atmospheric and Oceanic Technology*, **30**(9), 2063–2080.

Friedrich, K., Kalina, E. A., Masters, F. J., and Lopez, C. R. (2013b). Drop-size distributions in thunderstorms measured by optical disdrometers during vortex2. *Monthly Weather Review*, **141**(4), 1182–1203.

Gay, M., Fily, M., Genthon, C., Frezzotti, M., Oerter, H., and Winther, J.-G. (2002). Snow grain-size measurements in antarctica. *Journal of Glaciology*, **48**(163), 527–535.

Glickman, T. (2000). *Glossary of Meteorology*. American Meteorological Society.

Gordon, M. and Taylor, P. A. (2009). Measurements of blowing snow, part i: Particle shape, size distribution, velocity, and number flux at churchill, manitoba, canada. *Cold Regions Science and Technology*, **55**(1), 63–74.

Gorodetskaya, I. V., Kneifel, S., Maahn, M., Van Tricht, K., Thiery, W., Schween, J. H., Mangold, A., Crewell, S., and Van Lipzig, N. P. M. (2015). Cloud and precipitation properties from ground-based remote-sensing instruments in east antarctica. *The Cryosphere*, **9**(1), 285–304.

Gravner, J. and Griffeath, D. (2009). Modeling snow-crystal growth: A three-dimensional mesoscopic approach. *Physical Review E*, **79**(1), 011601.

Grazioli, J., Lloyd, G., Panziera, L., Hoyle, C. R., Connolly, P. J., Henneberger, J., and Berne, A. (2015). Polarimetric radar and in situ observations of riming and snowfall microphysics during clace 2014. *Atmospheric Chemistry and Physics*, **15**(23), 13787–13802.

Grazioli, J., Madeleine, J.-B., Gallée, H., Forbes, R. M., Genthon, C., Krinner, G., and Berne, A. (2017a). Katabatic winds diminish precipitation contribution to the antarctic ice mass balance. *Proceedings of the National Academy of Sciences*, **114**(41), 10858–10863.

Grazioli, J., Genthon, C., Boudevillain, B., Duran-Alarcon, C., Del Guasta, M., Madeleine, J.-B., and Berne, A. (2017b). Measurements of precipitation in dumont d'urville, adélie land, east antarctica. *The Cryosphere*, **11**(4), 1797–1811.

Griffiths, R. (1975). Comments on "the measurement of charge and size of raindrops: Parts i and ii". *Journal of Applied Meteorology*, **14**(3), 422–425.

Grigioni, P., Ciardini, V., De Silvestri, L., Iaccarino, A., Scarchilli, C., Camporeale, G., Dolci, S., Pellegrini, A., Proposito, M., and Schioppo, R. (2016). La rete di stazioni meteorologiche dell'osservatorio meteoclimatologico in antartide.

Gunn, K. L. S. and Marshall, J. S. (1958). The distribution with size of aggregate snowflakes. *Journal of Meteorology*, **15**(5), 452–461.

Gunn, R. and Kinzer, G. D. (1949). The terminal velocity of fall for water droplets in stagnant air. *Journal of Meteorology*, **6**(4), 243–248.

Heymsfield, A. (1975). Cirrus uncinus generating cells and the evolution of cirriform clouds. part iii: Numerical computations of the growth of the ice phase. *Journal of the Atmospheric Sciences*, **32**(4), 820–830.

Heymsfield, A., DeMott, P., Field, P., Rogers, D., Wang, Z., and Lasher-Trapp, S. (2010). The ice in clouds experiment-tropical field campaign-(ice-t). *Research Plan. Scientific Overview Doc.*

Heymsfield, A. J., Lewis, S., Bansemer, A., Iaquinta, J., Miloshevich, L. M., Kajikawa, M., Twohy, C., and Poellot, M. R. (2002). A general approach for deriving the properties of cirrus and stratiform ice cloud particles. *Journal of the atmospheric sciences*, **59**(1), 3–29.

Heymsfield, A. J., Bansemer, A., Schmitt, C., Twohy, C., and Poellot, M. R. (2004). Effective ice particle densities derived from aircraft data. *Journal of the atmospheric sciences*, **61**(9), 982–1003.

Hobbs, P. V. and Rangno, A. L. (1990). Rapid development of high ice particle concentrations in small polar maritime cumuliform clouds. *Journal of the Atmospheric Sciences*, **47**(22), 2710–2722.

Honeyager, R., Liu, G., and Nowell, H. (2016). Voronoi diagram-based spheroid model for microwave scattering of complex snow aggregates. *Journal of Quantitative Spectroscopy and Radiative Transfer*, **170**, 28–44.

Hong, G., Yang, P., Baum, B. A., Heymsfield, A. J., Weng, F., Liu, Q., Heygster, G., and Buehler, S. A. (2009). Scattering database in the millimeter and submillimeter wave range of 100–1000 ghz for nonspherical ice particles. *Journal of Geophysical Research: Atmospheres*, **114**(D6).

Huang, G.-J., Bringi, V., Cifelli, R., Hudak, D., and Petersen, W. (2010). A methodology to derive radar reflectivity–liquid equivalent snow rate relations using c-band radar and a 2d video disdrometer. *Journal of Atmospheric and Oceanic Technology*, **27**(4), 637–651.

IPCC (2014). *Observations:Cryosphere*. Cambridge University Press.

Jiang, H., Yin, Y., Su, H., Shan, Y., and Gao, R. (2015). The characteristics of atmospheric ice nuclei measured at the top of huangshan (the yellow mountains) in southeast china using a newly built static vacuum water vapor diffusion chamber. *Atmospheric Research*, **153**, 200 – 208.

Johnston, S. (2009). Climate change policies in the polar regions: Trade offs from an international policy laboratory. *IOP Conference Series: Earth and Environmental Science*, **6**(43), 432013.

Joly, M., Attard, E., Sancelme, M., Deguillaume, L., Guilbaud, C., Morris, C. E., Amato, P., and Delort, A.-M. (2013). Ice nucleation activity of bacteria isolated from cloud water. *Atmospheric Environment*, **70**, 392 – 400.

Keat, W. J. and Westbrook, C. D. (2017). Revealing layers of pristine oriented crystals embedded within deep ice clouds using differential reflectivity and the copolar correlation coefficient. *Journal of Geophysical Research: Atmospheres*, **122**(21).

Kennedy, P. C. and Rutledge, S. A. (2011). S-band dual-polarization radar observations of winter storms. *Journal of Applied Meteorology and Climatology*, **50**(4), 844–858.

Kneifel, S., Maahn, M., Peters, G., and Simmer, C. (2011). Observation of snowfall with a low-power fm-cw k-band radar (micro rain radar). *Meteorology and Atmospheric Physics*, **113**(1-2), 75–87.

Kobayashi, T. (1961). The growth of snow crystals at low supersaturations. *The Philosophical Magazine: A Journal of Theoretical and Applied Physics*, **6**(71), 1363–1370.

Kulie, M. S., Bennartz, R., Greenwald, T. J., Chen, Y., and Weng, F. (2010). Uncertainties in microwave properties of frozen precipitation: Implications for remote sensing and data assimilation. *Journal of the Atmospheric Sciences*, **67**(11), 3471–3487.

Kuo, K.-S., Olson, W. S., Johnson, B. T., Grecu, M., Tian, L., Clune, T. L., van Aartsen, B. H., Heymsfield, A. J., Liao, L., and Meneghini, R. (2016). The microwave radiative properties of falling snow derived from nonspherical ice particle models. part i: An extensive database of simulated pristine crystals and aggregate particles, and their scattering properties. *Journal of Applied Meteorology and Climatology*, **55**(3), 691–708.

Lachlan-Cope, T., Ladkin, R., Turner, J., and Davison, P. (2001). Observations of cloud and precipitation particles on the avery plateau, antarctic peninsula. *Antarctic Science*, **13**(3), 339–348.

Lau, K. M. and Wu, H. T. (2003). Warm rain processes over tropical oceans and climate implications. *Geophysical Research Letters*, **30**(24).

Leinonen, J. and Szyrmer, W. (2015). Radar signatures of snowflake riming: A modeling study. *Earth and Space Science*, **2**(8), 346–358.

Leinonen, J., Lebsock, M. D., Tanelli, S., Sy, O. O., Dolan, B., Chase, R. J., Finlon, J. A., von Lerber, A., and Moisseev, D. (2018). Retrieval of snowflake microphysical properties from multi-frequency radar observations. *Atmospheric Measurement Techniques*.

Libbrecht, K. G. (2005). The physics of snow crystals. *Reports on progress in physics*, **68**(4), 855.

Liou, K. and Yang, P. (2016). *Light Scattering by Ice Crystals: Fundamentals and Applications*. Cambridge University Press.

Liu, G. (2008). A database of microwave single-scattering properties for nonspherical ice particles. *Bulletin of the American Meteorological Society*, **89**(10), 1563–1570.

Locatelli, J. and Hobbs, P. (1974). Fall speeds and masses of solid precipitation particles. *Journal of Geophysical Research*, **79**(15), 2185–2197.

Löffler-Mang, M. and Blahak, U. (2001). Estimation of the equivalent radar reflectivity factor from measured snow size spectra. *Journal of Applied Meteorology*, **40**(4), 843–849.

Löffler-Mang, M. and Joss, J. (2000). An optical disdrometer for measuring size and velocity of hydrometeors. *Journal of Atmospheric and Oceanic Technology*, **17**(2), 130–139.

Löffler-Mang, M., Kunz, M., and Schmid, W. (1999). On the performance of a low-cost k-band doppler radar for quantitative rain measurements. *Journal of Atmospheric and Oceanic Technology*, **16**(3), 379–387.

Lu, Y., Jiang, Z., Aydin, K., Verlinde, J., Clothiaux, E. E., and Botta, G. (2016). A polarimetric scattering database for non-spherical ice particles at microwave wavelengths. *Atmospheric Measurement Techniques*, **9**(10), 5119–5134.

Maahn, M. and Kollias, P. (2012). Improved micro rain radar snow measurements using doppler spectra post-processing. *Atmospheric Measurement Techniques*, **5**(11), 2661–2673.

Magono, C. (1960). Structure of snowfall revealed by geographic distribution of snow crystals. In *Physics of Precipitation*, volume 60, page 142. Geophys. Monogr.

Magono, C. and Lee, C. W. (1966). Meteorological classification of natural snow crystals. *Journal of the Faculty of Science, Hokkaido University*, (2), 321–335.

Mann, G., Anderson, P., and Mobbs, S. (2000). Profile measurements of blowing snow at halley, antarctica. *Journal of Geophysical Research: Atmospheres*, **105**(D19), 24491–24508.

Marshall, J. S. and Palmer, W. M. K. (1948). The distribution of raindrops with size. *Journal of meteorology*, **5**(4), 165–166.

Metek (2010). *MRR Physical Basics*.

Milani, L., Kulie, M. S., Casella, D., D'Adderio, L. P., Dietrich, S., L'Ecuyer, T. S., Panegrossi, G., Porcù, F., Sanò, P., and Wood, N. B. (2016). On the use of Cloud Profiling Radar to detect solid precipitation over Antarctica at different scales. In *EGU General Assembly Conference Abstracts*, volume 18 of *EGU General Assembly Conference Abstracts*, pages EPSC2016–12167.

Mishchenko, M. (1990). Extinction of light by randomly-oriented nonspherical grains. *Astrophysics and space science*, **164**(1), 1–13.

Mishchenko, M. I. and Travis, L. D. (1998). Capabilities and limitations of a current fortran implementation of the t-matrix method for randomly oriented, rotationally symmetric scatterers. *Journal of Quantitative Spectroscopy and Radiative Transfer*, **60**(3), 309 – 324.

Mishchenko, M. I., Travis, L. D., and Mackowski, D. W. (1996). T-matrix computations of light scattering by nonspherical particles: A review. *Journal of Quantitative Spectroscopy and Radiative Transfer*, **55**(5), 535 – 575. Light Scattering by Non-Spherical Particles.

Mishchenko, M. I., Travis, L. D., and Lacis, A. A. (2002). *Scattering, absorption, and emission of light by small particles*. Cambridge university press.

Mitchell, D., Huggins, A., and Grubisic, V. (2006). A new snow growth model with application to radar precipitation estimates. *Atmospheric Research*, **82**(1-2), 2–18.

Molthan, A. L., Colle, B. A., Yuter, S. E., and Stark, D. (2016). Comparisons of modeled and observed reflectivities and fall speeds for snowfall of varied riming degrees during winter storms on long island, new york. *Monthly Weather Review*, **144**(11), 4327–4347.

Muramoto, K.-I., Matsuura, K., and Shiina, T. (1995). Measuring the density of snow particles and snowfall rate. *Electronics and Communications in Japan (Part III: Fundamental Electronic Science)*, **78**(11), 71–79.

Murray, B. J., Broadley, S. L., Wilson, T. W., Atkinson, J. D., and Wills, R. H. (2011). Heterogeneous freezing of water droplets containing kaolinite particles. *Atmospheric Chemistry and Physics*, **11**(9), 4191–4207.

Nowell, H., Liu, G., and Honeyager, R. (2013). Modeling the microwave single-scattering properties of aggregate snowflakes. *Journal of Geophysical Research: Atmospheres*, **118**(14), 7873–7885.

Oluwadare, E. J., Tomiwa, A., and Ajewole, M. (2010). Investigation of radiowave propagation impairment at super high frequency due to rain in akure. *Am. Int. J. Contemporary Res*, **2**(10), 122–137.

Ori, D. (2016). *Study of the optical properties of complex ice crystal aggregates*. Ph.D. thesis, Alma Mater Studiorum - University of Bologna.

Ori, D., Maestri, T., Rizzi, R., Cimini, D., Montopoli, M., and Marzano, F. (2014). Scattering properties of modeled complex snowflakes and mixed-phase particles at microwave and millimeter frequencies. *Journal of Geophysical Research: Atmospheres*, **119**(16), 9931–9947.

OTT (2017a). *Operating instructions: Parsivel Application Software ASDO*.

OTT (2017b). *Operating instructions: Present Weather Sensor OTT Parsivel*.

Palerme, C., Kay, J., Genthon, C., L'Ecuyer, T., Wood, N., and Claud, C. (2014). How much snow falls on the antarctic ice sheet? *The Cryosphere*, **8**(4), 1577–1587.

Patade, S., Nagare, B., Wagh, S., Maheskumar, R., Prabha, T. V., and Kumar, P. P. (2014). Deposition ice nuclei observations over the indian region during caipeex. *Atmospheric Research*, **149**, 300 – 314.

Peters, G., Fischer, B., and Clemens, M. (2010). Rain attenuation of radar echoes considering finite-range resolution and using drop size distributions. *Journal of atmospheric and Oceanic Technology*, **27**(5), 829–842.

Petty, G. W. and Huang, W. (2010). Microwave backscatter and extinction by soft ice spheres and complex snow aggregates. *Journal of the Atmospheric Sciences*, **67**(3), 769–787.

Piccardi, G., Udisti, R., and Casella, F. (1994). Seasonal trends and chemical composition of snow at terra nova bay (antarctica). *International journal of environmental analytical chemistry*, **55**(1-4), 219–234.

Ponzo, U. and Lori, A. (2007). *Descrizione della Stazione Mario Zucchelli*. Enea-PNRA.

Praz, C., Roulet, Y.-A., and Berne, A. (2017). Solid hydrometeor classification and riming degree estimation from pictures collected with a multi-angle snowflake camera. *Atmospheric Measurement Techniques*, **10**(4), 1335–1357.

Pruppacher, H. and Klett, J. (1997). *Microphysics of Clouds and Precipitation*. Kluwer Academic Publishers.

Purcell, E. M. and Pennypacker, C. R. (1973). Scattering and absorption of light by nonspherical dielectric grains. *The Astrophysical Journal*, **186**, 705–714.

Richter, J. H. (1969). High resolution tropospheric radar sounding. *Radio Science*, **4**(12), 1261–1268.

Roberto, N., Adirosi, E., Montopoli, M., Baldini, L., Dietrich, S., and Porcù, F. (2017). Preliminary microphysical characterization of precipitation at ground over Antarctica coast. *EGU General Assembly Conference Abstracts*, **19**, 15965.

Roberto, N., Baldini, L., Bracci, A., Montopoli, M., Adirosi, E., Gorgucci, E., Scarchilli, C., Grigioni, P., Ciardini, V., and Porcù, F. (2018). Preliminary results on microphysical characterization of precipitation over antarctica coast.

Rogers, D. C. (1974). The aggregation of natural ice crystals. *Rep. No. AR 110*, **35**.

Santachiara, G., Belosi, F., and Prodi, F. (2014). The mystery of ice crystal multiplication in a laboratory experiment. *Journal of the Atmospheric Sciences*, **71**(1), 89–97.

Saxena, V. K. and Weintraub, D. C. (1988). Ice forming nuclei concentrations at palmer station, antarctica. pages 679–682.

Scarchilli, C., Frezzotti, M., Grigioni, P., De Silvestri, L., Agnoletto, L., and Dolci, S. (2010). Extraordinary blowing snow transport events in east antarctica. *Climate Dynamics*, **34**(7-8), 1195–1206.

Scarchilli, C., Frezzotti, M., and Ruti, P. (2011). Snow precipitation at four ice core sites in east antarctica: Provenance, seasonality and blocking factors. *Climate Dynamics*, **37**, 2107–2125.

Scarchilli, C., Grigioni, P., Maahn, M., Negusini, M., Argentini, S., Pace, G., Frezzotti, M., De Silvestri, L., Ciardini, V., Galeandro, A., Iaccarino, A., Dolci, S., Proposito, M., and Camporeale, G. (2017). Solid precipitation estimation during summer snowfall events at a coastal site of the Terra Nova bay area, Antarctica. In *EGU General Assembly Conference Abstracts*, volume 19 of *EGU General Assembly Conference Abstracts*, page 10463.

Schlenczek, O., Fugal, J. P., Lloyd, G., Bower, K. N., Choularton, T. W., Flynn, M., Crosier, J., and Borrmann, S. (2017). Microphysical properties of ice crystal precipitation and surface-generated ice crystals in a high alpine environment in switzerland. *Journal of Applied Meteorology and Climatology*, **56**(2), 433–453.

Sekhon, R. and Srivastava, R. (1970). Snow size spectra and radar reflectivity. *Journal of the Atmospheric Sciences*, **27**(2), 299–307.

Sheperd, A., Ivins, E., Rignot, E., Smith, B., van de Broeke, M., Velicogna, I., Whitehouse, P., Briggs, K., Joughin, I., Krinner, G., *et al.* (2018). Mass balance of the antarctic ice sheet from 1992 to 2017. *Nature*, **556**, 219–222.

Shum, C., yen Kuo, C., and yi Guo, J. (2008). Role of antarctic ice mass balance in present-day sea-level change. *Polar Science*, **2**(2), 149 – 161.

Skofronick-Jackson, G., Hudak, D., Petersen, W., Nesbitt, S. W., Chandrasekar, V., Durden, S., Gleicher, K. J., Huang, G.-J., Joe, P., Kollias, P., *et al.* (2015). Global precipitation measurement cold season precipitation experiment (gcpex): for measurement's sake, let it snow. *Bulletin of the American Meteorological Society*, **96**(10), 1719–1741.

Souverijns, N., Gossart, A., Lhermitte, S., Gorodetskaya, I., Kneifel, S., Maahn, M., Bliven, F., and van Lipzig, N. (2017). Estimating radar reflectivity - snowfall rate relationships and their uncertainties over antarctica by combining disdrometer and radar observations. *Atmospheric Research*, **196**, 211 – 223.

Souverijns, N., Gossart, A., Lhermitte, S., Gorodetskaya, I. V., Grazioli, J., Berne, A., Duran-Alarcon, C., Boudevillain, B., Genthon, C., Scarchilli, C., *et al.* (2018). Evaluation of the cloudsat surface snowfall product over antarctica using ground-based precipitation radars. Manuscript under review for journal The Cryosphere.

Tokay, A., Wolff, D. B., and Petersen, W. A. (2014). Evaluation of the new version of the laser-optical disdrometer, ott parsivel2. *Journal of Atmospheric and Oceanic Technology*, **31**(6), 1276–1288.

Turner, J., Bindschadler, R., Convey, P., Di Prisco, G., Fahrbach, E., Gutt, J., Hodgson, D., Mayewski, P., and Summerhayes, C. (2009). *Antarctic climate change and the environment*. Scientific Committee on Antarctic Research.

Tyynelä, J. and Chandrasekar, V. (2014). Characterizing falling snow using multifrequency dual-polarization measurements. *Journal of Geophysical Research: Atmospheres*, **119**(13), 8268–8283.

Tyynelä, J., Leinonen, J., Moisseev, D., and Nousiainen, T. (2011). Radar backscattering from snowflakes: Comparison of fractal, aggregate, and soft spheroid models. *Journal of Atmospheric and Oceanic Technology*, **28**(11), 1365–1372.

Ulbrich, C. W. (1983). Natural variations in the analytical form of the raindrop size distribution. *Journal of Climate and Applied Meteorology*, **22**(10), 1764–1775.

Vali, G. (1985). Nucleation terminology. *Bulletin of the American Meteorological Society*, (66), 1426–1427.

Van Tricht, K., Gorodetskaya, I. V., Lhermitte, S., Turner, D. D., Schween, J. H., and Van Lipzig, N. P. M. (2014). An improved algorithm for polar cloud-base detection by ceilometer over the ice sheets. *Atmospheric Measurement Techniques*, **7**(5), 1153–1167.

Vardiman, L. (1978). The generation of secondary ice particles in clouds by crystal–crystal collision. *Journal of the Atmospheric Sciences*, **35**(11), 2168–2180.

Walden, V. P., Warren, S. G., and Tuttle, E. (2003). Atmospheric ice crystals over the antarctic plateau in winter. *Journal of Applied Meteorology*, **42**(10), 1391–1405.

Wang, J. and Georgakakos, K. P. (2005). Effects of cold microphysical processes on the surface precipitation variability of nonsquall tropical oceanic convection. *Journal of Geophysical Research: Atmospheres*, **110**(D22).

Wang, P. K. (2013). *Physics and Dynamics of Clouds and Precipitation*. Cambridge University Press.

Waterman, P. C. (1971). Symmetry, unitarity, and geometry in electromagnetic scattering. *Physical review D*, **3**(4), 825.

Woods, C. P., Stoelinga, M. T., and Locatelli, J. D. (2008). Size spectra of snow particles measured in wintertime precipitation in the pacific northwest. *Journal of the Atmospheric Sciences*, **65**(1), 189–205.

Yuter, S. E., Kingsmill, D. E., Nance, L. B., and Löffler-Mang, M. (2006). Observations of precipitation size and fall speed characteristics within coexisting rain and wet snow. *Journal of Applied Meteorology and Climatology*, **45**(10), 1450–1464.